Molecular beam epitaxy of the half-Heusler antiferromagnet CuMnSb

Dissertation zur Erlangung des naturwissenschaftlichen Doktorgrades
der Julius-Maximilians-Universität Würzburg

vorgelegt von

Lukas Scheffler

aus Schweinfurt

Würzburg, 2022

Imagination is more important than knowledge. For knowledge is limited, whereas imagination embraces the entire world, stimulating progress, giving birth to evolution.

Albert Einstein

CONTENTS

List of Figures

List of Tables

Acronyms

AFM atomic force microscopy

BEP beam equivalent pressure

CCD charge-coupled device

CSH compensating sample holder

DC direct current

FC field cooling

fcc face-centered cubic

FCW field cooled warming

FIB focused ion beam

FWHM full width at half maximum

GMR giant magnetoresistance

HAADF high-angle annular dark-field

HRXRD high resolution X-ray diffraction

MBE molecular beam epitaxy

ML monolayer

NMVF non-magnetic volume fraction

PIXE particle-induced X-ray emission

PMMA poly(methyl methacrylate)

RBS Rutherford backscattering spectrometry

RHEED reflection high-energy electron diffraction

RMS root mean square

RRR residual resistivity ratio

RSM reciprocal space map

SEM scanning electron microscope

SIMS secondary-ion mass spectrometry

SOT spin orbit torque

SQUID superconducting quantum interference device

STEM scanning transmission electron microscopy

$T_{\mathbf{N}}$ Néel temperature

TRM thermoremanent magnetization

UHV ultrahigh vacuum

ZFCW zero field cooled warming

$\Theta_{\mathbf{CW}}$ Curie-Weiss temperature

$\mu_{\mathbf{eff}}$ effective moment

μ**SR** muon spin rotation

Summary

This work presents a newly developed method for the epitaxial growth of the half-Heusler antiferromagnet CuMnSb. All necessary process steps, from buffer growth to the deposition of a protective layer, are presented in detail. Using structural, electrical, and magnetic characterization, the material parameters of the epitaxial CuMnSb layers are investigated.

The successful growth of CuMnSb by molecular beam epitaxy is demonstrated on InAs (001), GaSb (001), and InP (001) substrates. While CuMnSb can be grown pseudomorphically on InAs and GaSb, the significant lattice mismatch for growth on InP leads to relaxation already at low film thicknesses. Due to the lower conductivity of GaSb compared to InAs, GaSb substrates are particularly suitable for the fabrication of CuMnSb layers for lateral electrical transport experiments. However, by growing a high-resistive ZnTe interlayer below the CuMnSb layer, lateral transport experiments on CuMnSb layers grown on InAs can also be realized. Protective layers of Ru and Al_2O_3 have proven to be suitable for protecting the CuMnSb layers from the environment.

Structural characterization by high resolution X-ray diffraction (full width at half maximum of 7.7 ″ of the rocking curve) and atomic force microscopy (root mean square surface roughness of 0.14 nm) reveals an outstanding crystal quality of the epitaxial CuMnSb layers. The half-Heusler crystal structure is confirmed by scanning transmission electron microscopy and the stoichiometric material composition by Rutherford backscattering spectrometry. In line with the high crystal quality, a new minimum value of the residual resistance of CuMnSb ($\rho_0 = 35\,\mu\Omega \cdot cm$) could be measured utilizing basic electrical transport experiments.

An elaborate study of epitaxial CuMnSb grown on GaSb reveals a dependence of the vertical lattice parameter on the Mn/Sb flux ratio. This characteristic enables the growth of tensile, unstrained, and compressive strained CuMnSb layers on a single substrate material. Additionally, it is shown that the Néel temperature has a maximum of 62 K at stoichiometric material composition and thus can be utilized as a selection tool for stoichiometric CuMnSb samples. Mn-related defects are believed to be the driving force for these observations.

The magnetic characterization of the epitaxial CuMnSb films is performed by superconducting quantum interference device magnetometry. Magnetic behavior comparable to the bulk material is found, however, an additional complex magnetic phase appears in thin CuMnSb films and/or at low magnetic fields, which has not

been previously reported for CuMnSb. This magnetic phase is believed to be local-ized at the CuMnSb surface and exhibits both superparamagnetic and spin-glass-like behavior. The exchange bias effect of CuMnSb is investigated in combination with different in- and out-of-plane ferromagnets. It is shown that the exchange bias effect can only be observed in combination with in-plane ferromagnets.

Finally, the first attempts at the growth of fully epitaxial CuMnSb/NiMnSb heterostructures are presented. Both magnetic and structural studies by secondary-ion mass spectrometry indicate the interdiffusion of Cu and Ni atoms between the two half-Heusler layers, however, an exchange bias effect can be observed for the CuMnSb/NiMnSb heterostructures. Whether this exchange bias effect originates from exchange interaction between the CuMnSb and NiMnSb layers, or from ferromagnetic inclusions in the antiferromagnetic layer can not be conclusively identified.

ZUSAMMENFASSUNG

In dieser Arbeit wird eine neu entwickelte Methode für das epitaktische Wachstum des antiferromagnetischen halb-Heuslers CuMnSb vorgestellt. Alle notwendigen Prozessschritte, vom Pufferschichtwachstum bis hin zum Aufbringen einer Schutzschicht, werden detailliert dargestellt. Mittels struktureller, elektrischer und magnetischer Charakterisierung werden die Materialparameter der epitaktischen CuMnSb-Schichten untersucht.

Das erfolgreiche Wachstum von CuMnSb durch Molekularstrahlepitaxie wird auf InAs (001), GaSb (001) und InP (001) Substraten demonstriert. Während CuMnSb auf InAs und GaSb pseudomorph gewachsen werden kann, führt die signifikante Gitterfehlanpassung beim Wachstum auf InP bereits bei geringen Schichtdicken zur Relaxation. Aufgrund der geringeren Leitfähigkeit von GaSb im Vergleich zu InAs sind GaSb-Substrate besonders geeignet für die Herstellung von CuMnSb-Schichten für laterale elektrische Transportexperimente. Durch Einbringen einer hochohmigen ZnTe-Zwischenschicht unterhalb der CuMnSb-Schicht können jedoch auch laterale Transportexperimente an CuMnSb-Schichten, die auf InAs gewachsen werden, durchgeführt werden. Schutzschichten aus Ru und Al_2O_3 haben sich als geeignet erwiesen, die CuMnSb-Schichten vor der Umgebung zu schützen.

Die strukturelle Charakterisierung mittels hochauflösender Röntgendiffraktometrie (Halbwertsbreite der Rocking-Kurve von 7.7″) und Rasterkraftmikroskopie (quadratisches Mittel der Oberflächenrauhigkeit von 0.14 nm) zeigt eine hervorragende Kristallqualität der epitaktischen CuMnSb-Schichten. Die halb-Heusler Kristallstruktur wird durch Rastertransmissionselektronenmikroskopie und die stöchiometrische Materialzusammensetzung durch Rutherford-Rückstreuspektrometrie bestätigt. In Übereinstimmung mit der hohen Kristallqualität konnte ein neuer Minimalwert des Restwiderstands von CuMnSb ($\rho_0 = 35\,\mu\Omega \cdot cm$) mit Hilfe von einfachen elektrischen Transportexperimenten gemessen werden.

Eine ausführliche Untersuchung von epitaktischem CuMnSb, das auf GaSb gewachsen wurde, zeigt eine Abhängigkeit der vertikalen Gitterkonstante vom Mn/Sb-Flussverhältnis. Diese Eigenschaft ermöglicht das Wachstum von zugverspannten, unverspannten und druckverspannten CuMnSb Schichten auf einem einzigen Substratmaterial. Darüber hinaus wird gezeigt, dass die Néel-Temperatur bei stöchiometrischer Materialzusammensetzung ein Maximum von 62 K aufweist und somit als Auswahlinstrument für stöchiometrische CuMnSb Proben dienen

kann. Es wird angenommen, dass Mn-bezogene Defekte ursächlich für diese Beobachtungen sind.

Die magnetische Charakterisierung der epitaktischen CuMnSb-Filme erfolgt mittels Magnetometrie. Das magnetische Verhalten ist mit dem des Volumenmaterials vergleichbar. Allerdings tritt in dünnen CuMnSb Filmen und/oder bei niedrigen Magnetfeldern eine zusätzliche komplexe magnetische Phase auf, die bisher noch nicht für CuMnSb beobachtet wurde. Es wird angenommen, dass diese magnetische Phase an der CuMnSb-Oberfläche lokalisiert ist und sowohl superparamagnetisches als auch Spin-Glas-artiges Verhalten zeigt. Der Exchange Bias Effekt von CuMnSb wird in Kombination mit verschiedenen Ferromagneten mit vertikaler und horizontaler remanenter Magnetisierung untersucht. Es wird gezeigt, dass der Exchange Bias Effekt nur in Kombination mit Ferromagneten mit horizontaler remanenter Magnetisierung beobachtet werden kann.

Schließlich werden die ersten Versuche zum Wachstum von vollständig epitaktischen CuMnSb/NiMnSb-Heterostrukturen vorgestellt. Sowohl magnetische als auch strukturelle Untersuchungen mittels Sekundärionen-Massenspektrometrie weisen auf die Interdiffusion von Cu- und Ni-Atomen zwischen den beiden halb-Heusler Schichten hin. Der Exchange Bias Effekt kann an den CuMnSb/NiMnSb Heterostrukturen beobachtet werden. Ob dieser Exchange Bias Effekt auf Austauschwechselwirkungen zwischen den CuMnSb- und NiMnSb-Schichten oder auf ferromagnetische Einschlüsse in der antiferromagnetischen Schicht zurückzuführen ist, lässt sich nicht eindeutig feststellen.

1

Introduction

Around 1930, Louis Eugène Félix Néel gathered evidence that, besides the already known ferromagnetism, there is another ordered magnetic state known today as antiferromagnetism. At that time, he probably had no idea of the impact this magnetic state would have on science today, specifically in the field of spintronics. While antiferromagnetism was considered interesting but of no use in technology, ferromagnetism became a secret star of the digital age with the discovery of the giant magnetoresistance (GMR) effect by Albert Fert and Peter Grünberg in 1988 [1, 2]. The ability to read and manipulate the orientation of ferromagnets (which can represent the digital states 0 and 1) using spin-polarized currents spurred the research field of spintronics in the following years.

For antiferromagnetism, it was to take almost another 30 years before it could finally take spintronics to new heights by eliminating some of the main drawbacks of using ferromagnetic materials for data storage [3]. Two major advantages over ferromagnetic materials are the order of magnitude increase in intrinsic dynamic frequencies, which shortens switching times, and the absence of external stray fields, which increases the possible storage density. The possibility to manipulate an antiferromagnetic state by spin orbit torque (SOT) which is induced by electrical pulses and to read out the state via resistance measurements in planar Hall geometry was first demonstrated experimentally on CuMnAs by Wadley *et al.* in 2016 [4].

After a wave of euphoria when electrical switching was also demonstrated on other antiferromagnetic materials [5–8], the first doubts arose as to whether the measured signals were purely antiferromagnetic in nature. Thus, Chiang *et al.* showed that similar signals could also be generated without an antiferromagnetic layer when using the same device geometry and measurement procedure [9]. They attributed this to anisotropic thermal gradients and voltages due to the large current densities of the current pulses needed for switching. Furthermore, they consider

1

an unequivocal detection of the Néel vector before and after switching as essential for clear evidence of SOT switching of antiferromagnets.

That electrical switching observed in antiferromagnets can also be caused by effects other than SOT was demonstrated by recent studies on CuMnAs. It was possible to achieve an increase in resistance of several tens of percent by applying strong electrical pulses, which is comparable to the values achieved by the GMR effect [10, 11]. The so-called quench-switching was explained by the fragmentation of the antiferromagnetic state into many small domains, which in turn is probably due to growth defects [12]. However, an important difference to SOT switching is that the generated high-resistive state is not stable over time, but relaxes back to the initial state more or less quickly depending on the temperature. Quench-switching is therefore less suitable for data storage than for applications relating to neuronal computation.

Independently of the actual effect, switching experiments above and below the Néel temperature can be performed to check whether the switching is antiferromagnetic in nature. If the switching is observed only in the antiferromagnetic state and not in the paramagnetic state, it would be a strong indication of the switching of the antiferromagnet. The Néel temperatures of the materials previously used for switching experiments are so high (500 K, 525 K, and >1000 K for CuMnAs [13], NiO [14], and Mn_2Au [15], respectively) that they cannot be reached without destroying the material. Therefore, other antiferromagnetic materials with an accessible Néel temperature that meet the requirements for switching of the antiferromagnetic state are of particular interest.

The antiferromagnetic half-Heusler CuMnSb undergoes the magnetic transition at a temperature of about 60 K, which is accessible by standard laboratory equipment. In the antiferromagnetic state, its magnetic sites have the symmetry group $\bar{4}2m$, theoretically allowing Néel vector switching by antidamping SOT [16]. In addition, it has been predicted that a substantial nonlinear anomalous Hall effect could allow Néel vector detection by Hall measurements in CuMnSb [17]. These properties make CuMnSb a particularly suitable model platform for studying effects below and above the Néel temperature. Furthermore, CuMnSb is structurally very similar to the ferromagnetic half-Heusler NiMnSb. Therefore, the long-term experience with the epitaxial growth of NiMnSb [18–20] is helpful for the development of CuMnSb epitaxy, since the replacement of Ni by Cu is not expected to cause too much variation in the growth process.

To date, CuMnSb has only been investigated as a bulk material, fabricated by various melting techniques [21–27]. However, especially for electrical transport experiments like Néel vector switching, high-quality thin films with well-defined interfaces to other materials are needed. For such requirements, material growth by means of molecular beam epitaxy (MBE) is ideally suited. It enables the growth

1

of high-quality crystals and brings certain flexibility due to modifiable material composition. Additionally, it offers the possibility to grow heterostructures of CuMnSb and its ferromagnetic counterpart NiMnSb.

This work presents a newly developed growth process of CuMnSb layers by MBE including all the required process steps. Since a comprehensive understanding of the material is essential for the realization of functional transport devices, the basic material properties are presented through a detailed characterization of the grown layers, with a separate chapter elaborating more profoundly on the magnetism of epitaxial CuMnSb. In addition, the first attempts at the growth of CuMnSb/NiMnSb heterostructures are presented. As a basis, the half-Heusler CuMnSb and the methods used in this work are introduced at the beginning.

2

The half-Heusler CuMnSb

CuMnSb belongs to the remarkable material class of Heusler compounds. The naming of these alloys, which according to today's definition, mainly share the crystal structure and the composition of two transition metals (X and Y) and one *p*-electron element of the main group (Z), traces back to the German mining engineer and chemist Friedrich Heusler. During his studies in 1903, he discovered that the alloy Cu_2MnAl is ferromagnetic, although none of the alloying elements is ferromagnetic itself [28, 29]. Cu_2MnAl crystallizes in an $L2_1$ crystal structure which is formed by four face-centered cubic (*fcc*) sublattices translated by 1/4 along the long diagonal of the unit cell, which is explained in more detail below by means of the corresponding Wyckoff positions. In the case of the full-Heusler Cu_2MnAl, the two Cu atoms occupy Wyckoff positions 4c and 4d. This is in contrast to a half-Heusler, where the 4d position is unoccupied. It turned out that there exist many other alloys with the chemical formula X_2YZ that form an $L2_1$ crystal structure in the crystalline state and have different properties than would be expected from the combination of alloy constituents. This group of alloys was henceforth referred to as Heusler alloys. A distinction is made between full-Heusler alloys with the chemical formula X_2YZ and half-Heusler alloys with the chemical formula XYZ. The latter differ from the full-Heuslers in that one of the four *fcc* sublattices is unoccupied, resulting in a $C1_b$ crystal structure. Today, the group of known Heusler alloys has more than 1500 members that exhibit a broad spectrum of properties, which are of interest not only for scientific research but also for future spintronic device applications [30].

One of the members of the half-Heusler family is CuMnSb. It was first synthesized by Castelliz in 1952 while experimenting with CuMnSb-NiMnSb mixed crystals [31]. A demonstration of the $C1_b$ half-Heusler crystal structure followed in the same year by Nowotny and Glatzl [32]. Figure 2.1 **a** shows the resulting unit

2
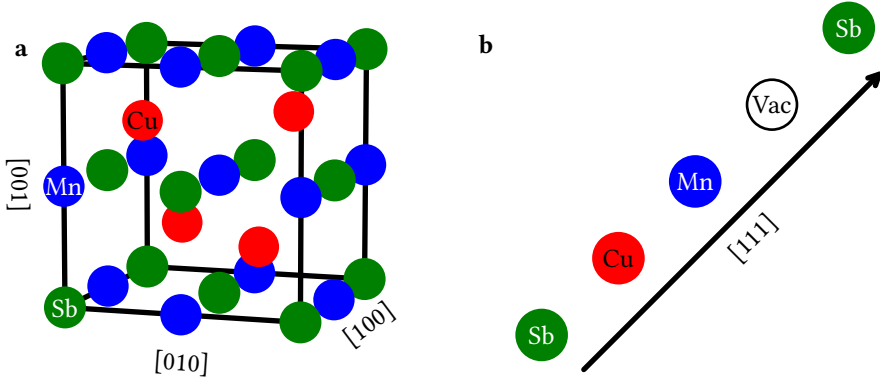
Figure 2.1: **C1$_b$ half-Heusler crystal structure of CuMnSb. a** Crystal structure of CuMnSb. The Wyckoff positions 4a (0, 0, 0), 4b (1/2, 1/2, 1/2), and 4c (1/4, 1/4, 1/4) are occupied by the atomic species Sb, Mn, and Cu, respectively, 4d (3/4, 3/4, 3/4) is vacant. **b** Long diagonal of the CuMnSb crystal along the [111] direction showing the lack of inversion symmetry.

cell of CuMnSb. The Wyckoff positions 4a (0, 0, 0), 4b (1/2, 1/2, 1/2), and 4c (1/4, 1/4, 1/4) are occupied by the atomic species Sb, Mn, and Cu, respectively. Sb and Cu form a zincblende sublattice in which Sb occupies the octahedral sites. The Wyckoff position 4d (3/4, 3/4, 3/4) is vacant, leading to a non-centrosymmetric lattice with space group $F\bar{4}3m$ (no. 216). This breaking of inversion symmetry is best seen by looking at the atoms located on the long diagonal of the crystal along the [111] direction, as shown in Figure 2.1 **b**. While the Mn atom would be surrounded by two Cu atoms in the corresponding full-Heusler, in the half-Heusler, it has a Cu atom on one side and a vacancy as a neighbor on the other side. It is this lack of inversion symmetry that might lead to spin-orbit interactions [26] and thus to the ability to realize SOT switching of CuMnSb [16].

Endo *et al.* reported on the first magnetic properties of CuMnSb. Using temperature dependent susceptibility measurements, they found CuMnSb to be antiferromagnetic and determined the Néel temperature (T_N) to be 55 K, the Curie-Weiss temperature (Θ_{CW}) to be −180 K and the the effective moment (μ_{eff}) to be 5.6 μ_B/f.u. [21]. Both the rather low T_N, and the ratio of $-\Theta_{CW}/T_N \approx 3$, are considered indicative of strong geometric frustration of the moments in the CuMnSb crystal [33, 34]. Using neutron experiments, Forster *et al.* were able to demonstrate that the antiferromagnetism of CuMnSb is of type-II and that the magnetic moments are localized at the Mn atoms [22]. In type-II antiferromagnets such as the transition
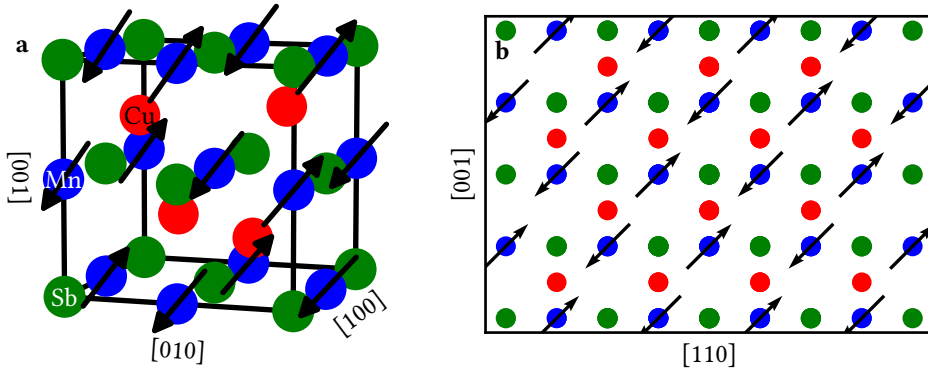
Figure 2.2: **Magnetic structure of CuMnSb. a** Crystal structure of CuMnSb with magnetic moments located at the Mn atoms. The magnetic moments are aligned ferromagnetically within the {111} planes and antiferromagnetically between the {111} planes. **b** CuMnSb crystal with line of sight in the [1$\bar{1}$0]. In this representation, the overlaying Mn moments share the same orientation.

metal oxides [35], the moments are aligned ferromagnetically within {111} planes and antiferromagnetically between {111} planes. Thereby, the magnetic moments are pointing in ⟨111⟩ directions. This magnetic structure, henceforth referred to as the AFM111 structure, is shown for the CuMnSb crystal in Figure 2.2 **a**. To illustrate the type-II antiferromagnetism more clearly, a two-dimensional representation of the CuMnSb crystal with magnetic moments is shown in Figure 2.2 **b**. With the line of sight in the [1$\bar{1}$0] direction, the magnetic moments located at the Mn sites in series have the same orientation. In the AFM111 state, there are four energetically identical magnetic domains with different orientations of the moments. The four possible orientations of the magnetic moments are:

- moments oriented along the [111] and [$\bar{1}\bar{1}\bar{1}$] directions

- moments oriented along the [$\bar{1}$11] and [1$\bar{1}\bar{1}$] directions

- moments oriented along the [11$\bar{1}$] and [$\bar{1}\bar{1}$1] directions

- moments oriented along the [1$\bar{1}$1] and [$\bar{1}$1$\bar{1}$] directions

Up to date, no studies have been published on the size of the magnetic domains and thus on the magnetic domain structure of CuMnSb in general.

Recent *ab initio* calculations by Máca *et al.* suggest, however, that the AFM111 state is not the ideal ground state of CuMnSb [36]. In fact, the AFM111 state is

stabilized by point defects like Mn_{Cu} (Mn antisites on the Cu lattice) and Mn_{vac} with concentrations of only a few percent. For an ideal CuMnSb crystal, they expect an antiferromagnetic state with moments aligned ferromagnetically within the {001} planes and antiferromagnetically in between the {001} planes. In this state, the moments are pointing in ⟨100⟩ directions. Other types of point defects may lead to even more complex ground states. It may be precisely this sensitivity to small changes in composition and to crystal defects that is responsible for the wide range of magnetic material parameters reported for bulk CuMnSb crystals. Various research groups have reported values ranging between 50 and 62 K, −250 and −120 K, and 3.9 and 6.3 μ_B/f.u. for T_N, Θ_{CW} and μ_{eff}, respectively [21–27]. In addition, a canted antiferromagnetic phase at low temperatures was recently discovered by Regnat *et al.* in CuMnSb grown by optical float zoning [26].

While the basic properties of CuMnSb are already intensively studied, the many aspects of this feature-rich material are still far from being fully understood. For instance, the antiferromagnetism of CuMnSb is described as unconventional as it shows signs of both local-moment and itinerant magnetism [37]. Furthermore, it is still debated whether CuMnSb is an antiferromagnetic half-metal [38]. More recent calculations by Shao *et al.* even suggest that multiple Weyl points may be present in the CuMnSb band structure, leading to a significant nonlinear anomalous Hall effect [17]. The resulting large Berry curvature is expected to depend strongly on the antiferromagnetic order, allowing Néel vector detection by Hall measurements. Experimental proof of these theories has not yet been provided.

3

Experimental methods

This chapter elaborates on the experimental methods used extensively throughout this work, especially when they are applied in a form that deviates from the standard described in the literature. Other methods utilized will be discussed at the appropriate place, if necessary. Explicitly, no introduction to the methods is given, but details of the methods specific to this work are explained. Furthermore, the equipment used is specified to increase the reproducibility of the results presented in this thesis. For a general introduction to the methods used, reference is made to standard literature at appropriate points.

3.1 Reflection High-energy Electron Diffraction

Reflection high-energy electron diffraction (RHEED) is used for *in-situ* observation of the layer surface during MBE growth. Comprehensive descriptions of RHEED can be found in [39, 40].

During the epitaxial growth of half-Heusler layers, the development of the RHEED reconstructions contains essential information about material composition and correctness of the growth parameters [20]. Therefore, for all samples dedicated to growth development, images of the RHEED reconstructions are taken during CuMnSb and NiMnSb growth at a defined interval (2 to 10 min, depending on the growth time) along the high symmetry crystal directions [100], [010], [110] and [1$\bar{1}$0] using a grayscale charge-coupled device (CCD) camera. The camera used is a DMK 23U274 from The Imaging Source with a Sony ICX274AL sensor. This sensor has a dynamic range of 12 bit. A stepper motor ensures the precise positioning of the wafer for the image acquisition along a specific crystal direction. To increase the lateral homogeneity of the material composition of the epitaxial layer during growth, the stepper motor continuously rotates the wafer at nine revolutions per minute between the acquisition of each RHEED image series. Both the stepper

motor and the CCD camera are controlled by the MBE control software MBEpy, which was developed during this work. An introduction to MBEpy can be found in Appendix A.

For the evaluation of the surface reconstructions observed by RHEED, the gray values recorded by the CCD camera are interpreted as intensities. In this work, these intensities are presented in a perceptually uniform sequential color map[1] for better visibility.

3.2 Atomic Force Microscopy

Surface imaging of the fabricated samples is performed by atomic force microscopy (AFM), using a DME DS-95 Igloo in AC-mode. More details on the used technique in this work can be found in [41], and more general introductions in [42, 43].

3.3 High Resolution X-ray Diffraction

High resolution X-ray diffraction (HRXRD) measurements are used for structural characterization of the fabricated layer stacks. They are carried out using a Pana-lytical X'Pert[3] MRD machine with a triple-axis detector operated with Cu $K_{\alpha 1}$ radiation and a symmetric Ge(220) monochromator. For a basic introduction to HRXRD, the reader is referred to the standard literature [44–47].

The mosaicity of a layer - a measure of the crystal quality of the layer - is determined by rocking curves (ω-scans) around the layer peak. In this work, the full width at half maximum (FWHM) of the rocking curve is used as the measure for the mosaicity and thus the crystal quality of a layer. The FWHM is obtained by fitting the measured rocking curve by a Voigt profile. Reciprocal space maps (RSMs) are used to analyze the pseudomorphic character of the grown layers. For the RSM studies in this work, the asymmetric (224) diffraction peak is used, as the intensity is sufficiently large for the CuMnSb layers as well as for the used III-V materials. Details of the technique used to measure RSMs can be found in [41]. $\omega - 2\theta$-diffractograms are used to determine the vertical lattice parameter and the crystalline layer thickness of the individual layers. Together with the known lattice parameter of the substrate, the strain of the epitaxial layers can be calculated.

The aforementioned parameters are obtained from the $\omega - 2\theta$-diffractograms by full dynamical simulations and fits based on the layer stack using the software xrayutilities [53]. The source code of all simulations and fits shown in this thesis can be found as described in section 3.7. The materials to be simulated are defined by their crystal structure and by the atomic species they consist of. In addition, the materials' elastic constants C_{ijkl} are required to calculate the change in the

---

[1]The perceived contrast of a perceptually uniform sequential color map is chosen to reflect the actual value change

Material	C_{11} (GPa)	C_{12} (GPa)	C_{44} (GPa)	reference
InAs	83.4	45.4	39.5	[48]
InP	101.1	56.1	45.6	[49]
GaSb	88.3	40.2	43.2	[50]
GaAs	119.0	53.4	59.6	[49]
ZnTe	82.0	42.0	55.0	[51]
NiMnSb	170.9	82.7	54.7	[52]
CuMnSb	105.6	63.9	39.2	[52]

Table 3.1: **Elastic constants of the materials used for HRXRD simulations with XRAYUTILITIES.** The elastic constants of GaAs are needed for the simulation of (In,Ga)As. All given values represent the elastic constants of the bulk material.

vertical lattice parameter for materials grown pseudomorphically on the substrate. For materials with cubic symmetry, which is valid for all materials used in this work, C_{ijkl} can be simplified to:

$$
C_{ijkl} = \begin{bmatrix}
C_{11} & C_{12} & C_{12} & 0 & 0 & 0 \\
C_{12} & C_{11} & C_{12} & 0 & 0 & 0 \\
C_{12} & C_{12} & C_{11} & 0 & 0 & 0 \\
0 & 0 & 0 & C_{44} & 0 & 0 \\
0 & 0 & 0 & 0 & C_{44} & 0 \\
0 & 0 & 0 & 0 & 0 & C_{44}
\end{bmatrix}.
\tag{3.1}
$$

Table 3.1 lists the elastic constants used for the HRXRD simulations in this work. The strain of a layer resulting from pseudomorphic growth on a non lattice-matched substrate is expressed by the strain tensor ε. Following [54], ε is:

$$
\varepsilon = \begin{pmatrix}
\varepsilon_\| & 0 & 0 \\
0 & \varepsilon_\| & 0 \\
0 & 0 & -\varepsilon_\|/\sigma^{(001)}
\end{pmatrix}
\tag{3.2}
$$

for (001)-oriented pseudomorphic layer stacks, which applies to all layer stacks fabricated in this work. Here, $\varepsilon_\|$ is the in-plane strain and $\sigma^{(001)}$ is the Poisson's ratio for the epitaxial film on a (001) substrate. $\varepsilon_\|$ is calculated by:

$$
\varepsilon_\| = \frac{a_{\text{substrate}} - a_{\text{layer}}}{a_{\text{layer}}},
\tag{3.3}
$$

with $a_{\text{substrate(layer)}}$ being the intrinsic lattice parameter of the substrate (layer). $\sigma^{(001)}$ is defined by:

$$
\sigma^{(001)} = \frac{C_{11}}{2C_{12}}.
\tag{3.4}
$$

The strained horizontal lattice parameter $a_{\text{layer}}^{\text{strained}}$ and vertical lattice parameter $c_{\text{layer}}^{\text{strained}}$ can then be calculated by:

$$a_{\text{layer}}^{\text{strained}} = a_{\text{layer}}(1 + \varepsilon_\parallel) \tag{3.5}$$

and

$$c_{\text{layer}}^{\text{strained}} = a_{\text{layer}}(1 - \frac{\varepsilon_\parallel}{\sigma^{(001)}}) = a_{\text{layer}}(1 - \frac{2C_{12}\varepsilon_\parallel}{C_{11}}). \tag{3.6}$$

3.4 SQUID Magnetometry

Magnetic characterization of the fabricated samples is realized by superconducting quantum interference device (SQUID) magnetometry using a Quantum Design MPMS-XL machine. Time, temperature, and magnetic field dependent measurements of the magnetization of the sample can be performed with this system. Basic information on this technique can be found in [55, 56]. Due to the low external magnetic moment of a few nanometer thin antiferromagnetic layers, some precautions and adjustments have to be made for the magnetic characterization of epitaxial CuMnSb grown on 500 μm thick diamagnetic substrates, as the diamagnetic signal can easily dominate the measured signal. The optimized procedure presented below is the result of an extensive collaboration with Prof. Dr. hab. Maciej Sawicki and Dr. Katarzyna Gas from the Institute of Physics of the Polish Academy of Sciences.

The samples must be prepared for the SQUID magnetometry measurements. Therefore, the indium glue used to attach the substrate during MBE growth is removed from the backside, as its magnetic response matches well the range of the signals expected from thin antiferromagnetic layers [57]. About 200 μm are removed from the back of the sample by mechanical polishing on Al_2O_3 powder. The top surface of the sample is thereby glued to a stamp made of brass. To protect the surface of the sample, it is covered with a poly(methyl methacrylate) (PMMA) film before being glued on. After polishing, all residues are removed in a bath of acetone at 50 °C, followed by rinsing with isopropanol. This cleaning process ensures that no contaminants remain on the sample, which could create an additional magnetic moment. The samples are then glued to the sample holders using GE Low Temperature Varnish.

After sample preparation, the magnetic measurements are performed following the protocol for measuring minute signals [58]. Compared to the diamagnetic signal of the substrates, the antiferromagnetic signal of CuMnSb is tiny. The signals of buffer and cap are of a comparable order of magnitude. To be able to make quantitative statements about the magnetism of the CuMnSb layer, the magnetic measurements must therefore be compensated for the signals from substrate, buffer,
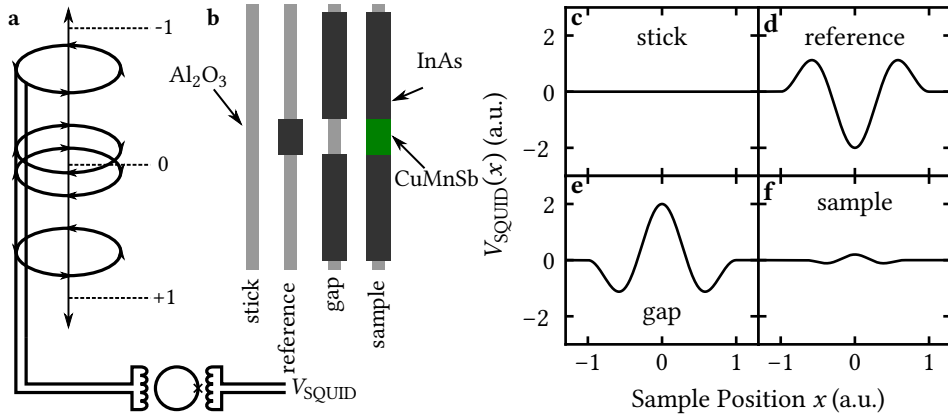
Figure 3.1: **Simplified principle of the *in-situ* compensation. a** Schematic of the second derivative axial gradiometer coupled inductively to the SQUID. **b** Possible configurations of stick, reference material and sample. **c-f** Resulting SQUID voltages for the configurations shown in **b**.

and cap. For this, a recently developed method for *in-situ* compensation [59], as well as a slightly modified method, are used. Both methods are described in more detail below, starting with the original approach.

A second derivative axial gradiometer is used in the SQUID magnetometer. It consists of four pickup coils, the middle two of which are wound in opposite directions to the outer ones. Moving a sample through the gradiometer, changes in magnetic flux induce a current in the coils. By an inductive coupling to the DC-SQUID, this current is transformed into a voltage V_{SQUID} which is proportional to the change in magnetic flux within the coils. This setup is depicted schematically in Figure 3.1 **a**.

From the development of V_{SQUID}, in turn, the magnetic moment of the sample can be inferred. In simplified terms, it can be assumed that the magnetic moment of the sample is proportional to the enclosed area of the function $V_{SQUID}(x)$, where x is the position of the sample with respect to the center of the gradiometer. Samples are typically mounted on sticks for measurements, as shown in Figure 3.1 **b**. Compared to the dimensions of the gradiometer, such a stick is infinitely long. If the stick is uniform and moved through the gradiometer without a sample, there is no change in the magnetic flux in the pickup coils and thus $V_{SQUID}(x) = 0$, as shown in Figure 3.1 **c**. Mounting an additional diamagnetic sample ("reference" in Figure 3.1) on the stick results in the curve shown in Figure 3.1 **d** for $V_{SQUID}(x)$ in a positive magnetic field. The signal shown is generated by the special arrangement of the four pickup coils. The negative moment of the diamagnetic sample induces a positive current in the two outer individual pickup coils, which leads to the two maxima

at the beginning and at the end of the measurement of $V_{\text{SQUID}}(x)$. The opposite winding direction of the two inner pickup coils, however, leads to a minimum in the middle of the measurement of $V_{\text{SQUID}}(x)$ as the induced current is of opposite sign. By using two coils at the same location, the amplitude of this minimum is doubled compared to the two maxima produced by the outer pickup coils.

Since $V_{\text{SQUID}}(x)$ maps the change in magnetic flux, a signal of $V_{\text{SQUID}}(x)$ which is inverse to that shown in Figure 3.1 **d** can be created by attaching long strips of the same material to the stick and leaving a gap with the exact dimensions of the sample as depicted in Figure 3.1 **b**. This signal is shown in Figure 3.1 **e**. Placing a sample consisting of the previously discussed diamagnetic material and an additional layer of CuMnSb in this gap, the diamagnetic material again forms an infinitely long strip with respect to the dimensions of the gradiometer. Hence, the diamagnetic material does not generate a signal, and $V_{\text{SQUID}}(x)$ contains only the change in magnetic flux generated by the CuMnSb layer. In this simplified case, the diamagnetic material is fully compensated.

Based on this principle, a so-called compensating sample holder (CSH) was manufactured using a sapphire stick and InAs strips for compensation of samples grown on InAs substrates. It is shown together with a mounted sample in Figure 3.2 **a**. The sample does not fill the entire gap of the CSH, since it is not practical to fit each sample precisely to it. To achieve full compensation, a total of three different measurements are required, specifically the gap alone, the gap together with a reference sample (R), and the gap together with the actual sample (S) have to be measured as depicted in Figure 3.2 **b**. Here, the reference sample consists of the same layers as the actual sample, without the CuMnSb layer. The resulting $V_{\text{SQUID}}(x)$, which are the sums of the individual components, are shown in Figure 3.2 **c-e** for these cases. Figure 3.2 **c** shows the signal generated only by the gap (G). This signal is also shown as a light blue line in Figure 3.2 **d** and **e**. The signals of the reference sample (R) and the actual sample (S) are shown as light red lines in Figure 3.2 **d** and **e**. As can be seen, the sums of the individual components (G+R and G+S) shown as black lines in Figure 3.2 **d** and **e** differ from the simplified representation in Figure 3.1, where the reference and the sample completely fill the gap. Therefore, in order to perform a compensation, the geometries of the gap, the reference, and the sample must be considered.

Taking geometrical factors γ, which scale the magnetometer output of physical bodies to their point object equivalent [58] and masses μ of the samples into account, $V_{\text{SQUID}}(x)$ and thus the magnetic moment of the CuMnSb layer m_{CuMnSb} can be calculated by:

$$m_{\text{CuMnSb}} = \frac{m_{\text{S}} - m_{\text{R}} + \beta m_{\text{G}}}{\gamma_{\text{CuMnSb}}} \tag{3.7}$$
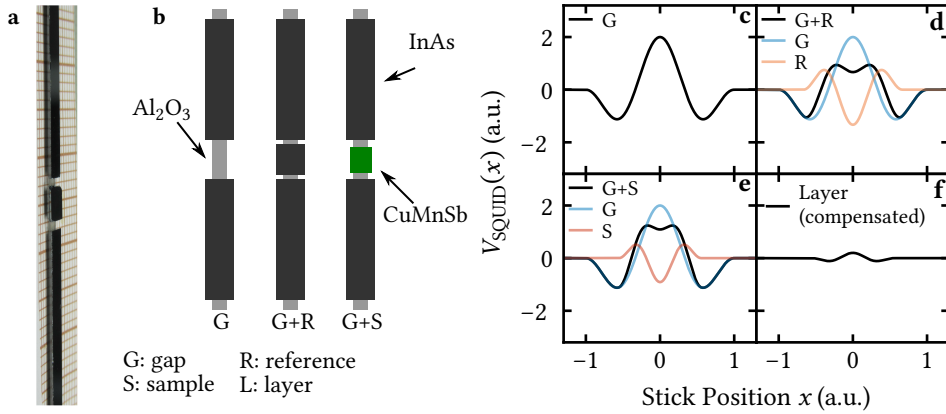
Figure 3.2: ***In-situ* compensation of magnetic measurements using the CSH. a** Image of the CSH made of an Al_2O_3 stick and InAs compensation strips. A sample is glued in the gap of the CSH. **b** Possible configurations of CSH, reference material and sample. The gap of the CSH is usually not completely filled. **c-f** Resulting SQUID voltages for the configurations shown in **b** and for the compensated signal of the layer.

with:

$$\beta = \frac{\mu_R \gamma_R - \mu_S \gamma_S}{\mu_G \gamma_G}. \tag{3.8}$$

The resulting compensated $V_{SQUID}(x)$ of the CuMnSb layer is shown in Figure 3.2 **f**. Compensation can be performed this way for all field, time, and temperature dependent measurements. Measurements presented in this thesis that were obtained using this compensation method are marked with the label CSH in the figure caption.

For samples grown on GaSb substrates and for some samples grown on InAs, a slightly modified and simplified process is used for compensation. Thereby, the samples are mounted on a plain Si stick without compensation strips. The desired measurement is performed for the actual sample (S) and a reference sample (R) without the CuMnSb layer. Considering γ and μ, the compensated magnetic moment of the CuMnSb layer m_{CuMnSb} can then be derived from:

$$m_{CuMnSb} = \frac{m_S}{\gamma_S} - \frac{m_R}{\gamma_R} \cdot \frac{\mu_S}{\mu_R}. \tag{3.9}$$

The measurements compensated with this method are marked with the label COMP in the figure caption. The COMP method has a slightly higher inaccuracy compared to the CSH method, since the higher absolute signals during the measurements require a higher measuring range, which in turn leads to higher noise.

Unless otherwise stated, all unlabeled magnetic measurements shown in this work are measured uncompensated on simple Si sticks, which is sufficient for qualitative evaluations.

3.5 Particle-induced X-ray Emission & Rutherford backscattering spectroscopy

Particle-induced X-ray emission (PIXE) is used for the analysis of the material composition of the manufactured samples. The experiments are performed on the 2 MV Van de Graaff generator at the Ion Beam Center of Helmholtz-Zentrum Dresden-Rossendorf by Dr. Shengqiang Zhou. Three types of spectra can be acquired with this instrument, which are the Rutherford backscattering spectrum, X-ray emission spectrum, and channeling spectrum. A collimated 1.7 MeV He+ beam is used to acquire the spectra at a backscattering angle of 170°. Simulation of Rutherford backscattering spectrometry (RBS) measurements is performed using the SIMNRA software [60]. More introductory information about this technique can be found in [61].

3.6 Open Source Software

This thesis was set in LuaLATEX using the Libertinus and Inconsolata fonts. The following open source software packages are used in this work for calculations, data analysis, and figure generation:

- Python 3 [62]

- NumPy [63]

- SciPy [64]

- Matplotlib [65]

- Inkscape [66]

- scikit-image [67]

3.7 Reproducibility of this work

To increase the reproducibility of the results presented in this work, all figures that are based on measurement data are generated by Python scripts. Thereby always the raw data of the measurements is used. This way, the Python code can be used to track exactly how the figures are generated from the raw data.

The source code of this work is available on the EP3-GitLab server at `https://gitlabep3.physik.uni-wuerzburg.de/lus66ad/dissertation`. The used measurement data can be found in the `src/data` folder. The `src/python` folder contains all Python scripts used to generate the figures. For compiling the figures and the work itself, a LuaLaTeX installation, as well as installations of Python, pip and Inkscape are necessary. If these dependencies are fulfilled, the working environment can be created on Unix-based operating systems with the command `make prepare`. Afterwards the figures and the work can be compiled with the commands `make figures` and `make compile`. If one wants to edit single figures, an interactive view of a figure can be created by executing the corresponding Python file. The virtual Python environment created by `make prepare` must therefore be activated using `source .venv/bin/activate`. The execution of the Python file must be carried out inside the `src/python` folder.

The measurement data files all have the corresponding sample name in their file name. This allows both the measurement data and the figures to be traced back to the associated sample. A list of all samples from which measurement data is shown in this work is therefore given in Appendix B. In addition, all data shown in this paper are tagged with the sample name in the form of such badges: Sample Name. This allows an unambiguous assignment of the data to the respective layer stack.

4

Sample fabrication and layer growth by MBE

In this chapter, all essential steps of sample preparation are explained, including substrate selection and preparation, buffer growth, layer growth, and cap layer deposition. The latter three are performed in an ultrahigh vacuum (UHV) cluster system that combines several specialized MBE chambers, characterization instruments, and material deposition chambers. All MBE chambers used are operated by the MBEPY software, which was developed during this work. An introduction to this software is given in Appendix A. Details about the machines used are provided at the appropriate places. For a general introduction to MBE, the reader is referred to the literature [44].

4.1 Substrate selection and preparation

All samples are grown on epi-ready (001) substrates with a maximum miscut of 0.1° according to the specifications of the wafer manufacturer. Depending on the application, the 2 inch wafers are cleaved into smaller pieces before growth. The substrate materials used are InAs, InP and GaSb, all III-V compound semiconductors. Members of this family of materials are particularly suitable for the use as substrates for the epitaxial growth of half-Heuslers, as they share the space group $F\bar{4}3m$ (no. 216).

In the context of CuMnSb and NiMnSb growth, the most relevant differences within the substrates are their lattice parameters and conductivities. Figure 4.1 shows the lattice parameters of both the substrates and the materials CuMnSb, NiMnSb, and ZnTe that are epitaxially grown on these substrates. While GaSb allows the growth of nearly unstrained CuMnSb, growth on InAs and InP always leads to epitaxially strained layers.
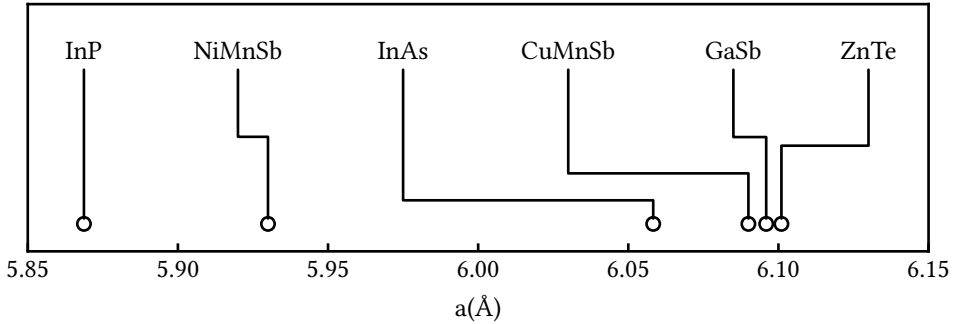
Figure 4.1: **Intrinsic lattice parameters of the materials used as substrates and/or as epitaxial layers.**

Especially for lateral transport measurements, the conductivity of the substrate is crucial. Therefore, different dopants for InAs, GaSb, and InP were investigated. We found that low Te doping for GaSb and Fe doping for InP resulted in the lowest parallel conductance values for transport measurements. For InAs, all available doping variants showed conductance values too high for lateral transport experiments. Further details, especially on the conductivity of doped GaSb substrates, can be found in [68]. All results in this thesis stem from samples grown on InAs:undoped, GaSb:lowTe, or InP:Fe substrates, unless otherwise stated.

Before the substrates are loaded into the UHV cluster, they are mounted with indium glue on Mo blocks used for the transport system. To prevent contamination of the UHV system by water residues, the loaded samples are degassed before entering the inner vacuum sector of the cluster. GaSb substrates are degassed at 100 °C for 30 min, InAs and InP at 250 °C for 10 min.

4.2 Buffer layer growth

Epi-ready substrates are covered with a thin oxide layer. To accomplish epitaxial growth on the surface, this layer must be removed. In this work, the oxide layer is removed by desorption as it is common for III-V substrates. This process can leave a rough surface morphology. By growing a 100 to 200 nm thick buffer layer, the surface can be smoothed to ensure perfect conditions for the growth start of the half-Heusler thin films. The buffer layer materials used are InAs for InAs substrates, GaSb for GaSb substrates, and lattice-matched (In,Ga)As for InP substrates. A buffer layer of ZnTe can be used to create a high-resistance barrier to prevent parallel conductivity in lateral transport experiments.

The Growth of InAs, GaSb and (In,Ga)As is performed in the III-V-MBE chamber (RIBER Compact 21) of the UHV cluster. In and Ga are evaporated by dual filament

Figure 4.2: **Temperature development of the substrate during InAs buffer growth with critical process milestones together with the surface reconstruction observed after growth. a** After oxide desorption, indicated by 3D dots in the RHEED pattern, the substrate is heated up until a 4 × 2 surface reconstruction appears and no more signs of 3D dots are observed. During cooldown to the growth temperature, the RHEED pattern exhibits a transition from 4 × 2 to 2 × 4. 10 °C below this transition temperature the InAs growth takes place. **b** d/2 reconstruction in [110] crystal direction. **c** d/4 reconstruction in [1$\bar{1}$0] crystal direction. For both crystal directions Kikuchi lines and Laue spots are visible.

effusion cells, and Sb by a single filament effusion cell. As flux is supplied by a valved cracker cell that is operated below the cracking temperature. ZnTe is grown in the II-VI-MBE chamber (RIBER Compact 21), where Zn and Te are evaporated by single filament effusion cells. The main shutters of the chambers used for buffer growth are open during the entire process to avoid contamination of the sample surface by the movement of the shutter.

4.2.1 InAs on InAs

The growth of the InAs buffer layers is largely adopted from the well-established process of InAs (001) homoepitaxy reported in [69]. Growth in the As-rich regime with an As:In beam equivalent pressure (BEP) ratio of 15:1 resulted in the best layer quality. The BEPs used are 6.7×10^{-6} mbar for As and 4.4×10^{-7} mbar for In. All critical steps of the growth process are depicted in Figure 4.2 **a**. For oxide desorption, the substrate is heated at a temperature rate of 30 °C min^{-1}. An As flux is provided above 300 °C to prevent As atoms of the substrate from desorbing, as explained in [69]. The beginning of the desorption process of the oxide layer at about 500 °C is represented by 3D dots in the RHEED pattern. When the oxide is fully removed (usually at temperatures around 570 °C), as indicated by a clear and

Figure 4.3: **Structural characterization of InAs buffer layers. a** AFM measurement of the InAs buffer surface ▣C21.1-1906 . Steps with the height of half an InAs unit cell are present. **b** Line profile extracted from the highlighted area in **a**. **c** Rocking curve of the (004) diffraction peak (dots) of an InAs buffer on an InAs substrate ▣C21.1-1751 with fitted Voigt profile (line). The fit yields a FWHM of 8.7 ″.

sharp 4 × 2 reconstruction, the substrate is cooled to growth temperature. During cooldown, the RHEED reconstruction transforms from 4 × 2 to 2 × 4 at about 510 °C. This transition plays an essential role in determining the ideal growth temperature for As-rich growth. It has been found that the ideal growth temperature is 10 °C below the temperature at which this transition is observed.

The growth of InAs is initiated by opening the In cell shutter after the substrate has been stabilized to growth temperature. Typical growth rates of $10\,\text{nm}\,\text{min}^{-1}$ lead to growth times of 15 min. Throughout growth a sharp and distinct 2 × 4 RHEED reconstruction (Figure 4.2 **b** and **c**) is observed. Growth is terminated by closing the In cell shutter. During the cooldown, the RHEED reconstruction remains unchanged. As flux is applied until the intensity of the RHEED pattern starts to decrease. This usually occurs at about 430 °C.

The high crystal quality of the InAs buffers is confirmed by AFM and HRXRD measurements (Figure 4.3). Figure 4.3 **a** shows the surface of an InAs buffer measured by AFM. The surface has a low root mean square (RMS) roughness of 0.15 nm. According to the line profile shown in Figure 4.3 **b**, the visible steps are of the height of half an InAs unit cell. A rocking curve of the (004) diffraction peak of InAs is shown in Figure 4.3 **c**. The Voigt profile fit yields a FWHM of 8.7 ″, which is no degradation compared to bare substrates.

4.2.2 GaSb on GaSb

Following the optimized growth process developed in [41], the GaSb buffer layers are grown with an Sb:Ga BEP ratio of 7.5:1. This is achieved by applying BEPs of 4.0×10^{-6} mbar and 5.3×10^{-7} mbar for Sb and Ga, respectively. Figure 4.4 **a** shows all important process milestones of the GaSb buffer growth. For oxide desorption,
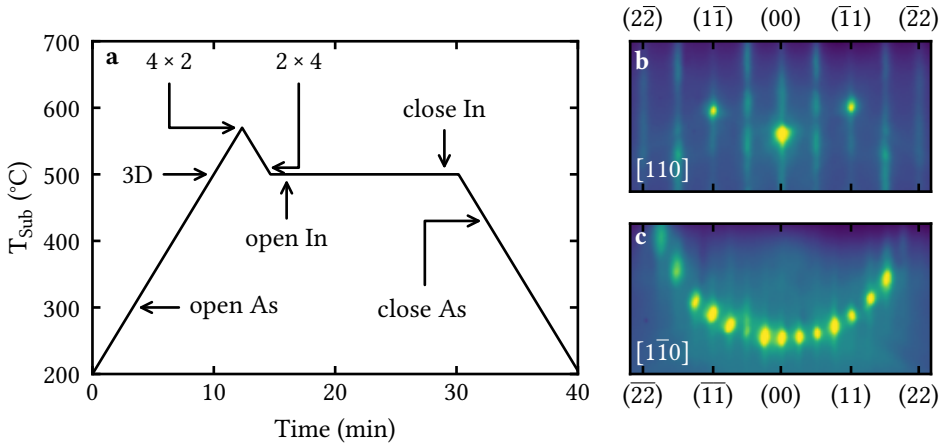
Figure 4.4: **Temperature development of the substrate during GaSb buffer growth with critical process milestones together with the surface reconstruction observed after growth. a** The desorption of the oxide is indicated by 3D dots in the RHEED pattern. When the substrate is stabilized at the growth temperature, growth is initiated by opening the shutter of the Ga cell. Within the first minute of growth a 1 × 3 reconstruction is observed by RHEED, which remains unchanged during growth. After terminating the growth by closing the shutter of the Ga cell, the substrate is cooled down. Between 400 and 350 °C the 1 × 3 reconstruction transforms to 2 × 5. **b** d/2 reconstruction in [110] crystal direction. **c** d/5 reconstruction in [1$\bar{1}$0] crystal direction.

the substrate is first heated up to 600 °C at a rate of 30 °C min^{-1} with Sb flux applied above 250 °C. After the substrate is held at 600 °C until dots in the RHEED pattern indicate a 3D surface, it is cooled to the growth temperature of 530 °C.

Once the substrate temperature has stabilized, buffer growth is initiated by opening the Ga shutter. Within the first minute of growth, the 3D surface transforms into a 2D surface, indicated by a 1 × 3 reconstruction. This reconstruction remains unchanged during growth. The used BEPs lead to a growth rate of 10 nm min^{-1}. For typical GaSb buffer thicknesses of 150 to 200 nm, the growth time is therefore 15 to 20 min. Upon reaching the desired layer thickness, the growth is terminated by closing the Ga shutter. During cooldown, the surface reconstruction transforms from 1 × 3 to 2 × 5 between 400 and 350 °C. The 2 × 5 reconstruction is shown in Figure 4.4 **b** and **c**. As soon as the substrate temperature is below 250 °C, the application of Sb flux is halted.

Figure 4.5 **a** shows an AFM image of the surface of a GaSb buffer layer. A low RMS roughness of 0.08 nm confirms a high surface quality of the grown GaSb. Again, atomic steps with the height of half a unit cell are visible on the surface, as revealed by the line profile in Figure 4.5 **b**.
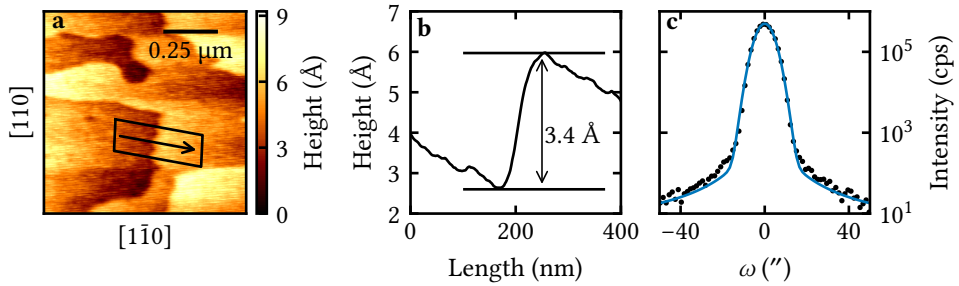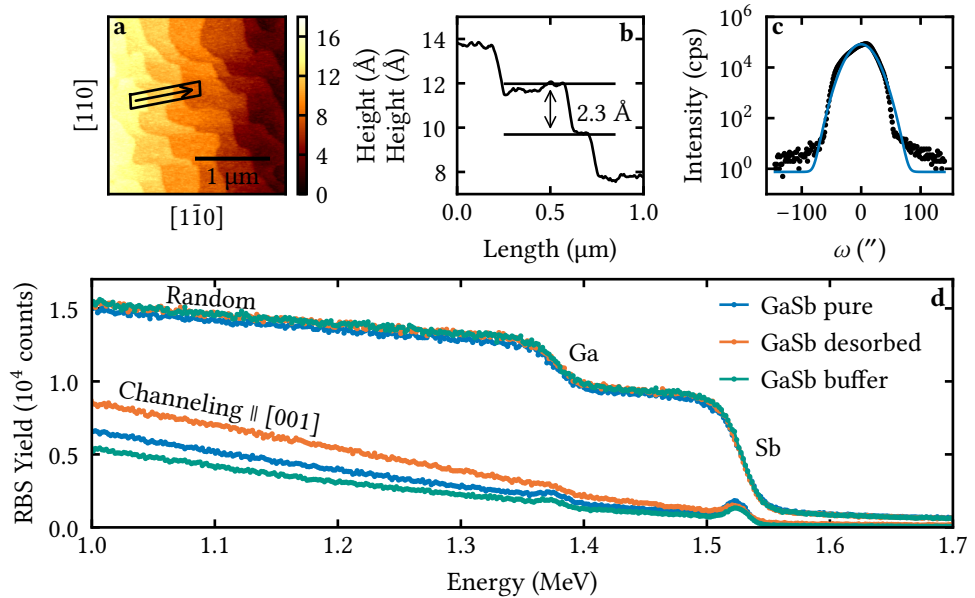
Figure 4.5: **Structural characterization of GaSb buffer layers. a** AFM measurement of the GaSb buffer surface C21.1-2045 . Steps with the height of half a GaSb unit cell are present. **b** Line profile extracted from the highlighted area in **a**. **c** Rocking curve of the (004) diffraction peak (dots) of a GaSb buffer on a GaSb substrate C21.1-1990 with fitted Voigt profile (line). The fit yields a FWHM of 38.7 ″. **d** RBS spectra in random and channeling configuration of a pure GaSb wafer, a GaSb wafer after oxide desorption C21.1-2249 , and a GaSb wafer with GaSb buffer layer C21.1-2244 .

Judging from the 2D surface reconstruction observed by RHEED and the atomically smooth surface imaged by AFM, the GaSb buffers have comparable quality to the InAs buffers. However, considering the rocking curve in Figure 4.5 **c** of a sample after buffer growth, the wide FWHM of 38.7 ″ indicates increased mosaicity. In comparison, the FWHM of an unprocessed low Te doped GaSb wafer is 9.9 ″. Thus, the deterioration in crystal quality must be caused by a process during sample preparation or buffer growth. Detailed investigations in [41] conclude that the degradation of the GaSb crystal results from the high substrate temperatures during oxide desorption. Furthermore, it was shown that lowering the maximum substrate temperature during the desorption process is not a suitable solution. Although lowering the substrate temperature during the desorption process prevented degradation of the substrate, complete desorption of the oxide layer was prevented. The degradation of the substrate is probably due to stresses in the GaSb crystal caused by temperature gradients due to non-uniform heat distribution in the substrate. Clamping the substrates to the Mo blocks instead of gluing them with In glue could

prevent this in the future since with clamped substrates the heat radiation from the substrate heater hits the substrate directly. However, this would require major modifications to the MBE chamber used for Heusler growth, as in this chamber the measurement and thus control of the substrate temperature can only be performed indirectly via the temperature of the Mo block at the back. Whether such a change of the desorption process is necessary with respect to the CuMnSb growth is highly questionable, since, as shown in the next paragraph, the quality of the GaSb buffer and thus the starting conditions for the CuMnSb growth are not affected by the degradation of the GaSb substrate.

To further investigate the influence of the substrate degradation on the starting conditions for the growth of CuMnSb, RBS spectra in random and channeling configuration are recorded for each of an unprocessed GaSb sample, a GaSb sample after oxide desorption, and a GaSb sample after buffer growth. The recorded spectra are plotted in Figure 4.5 **d**. As expected, in the random configuration all three samples show comparable RBS spectra consisting of the signals of the elements Ga and Sb. In the channeling configuration, however, the sample with desorbed oxide shows a steeper increase in the dechanneling yield towards lower energies than the pure GaSb sample, just below the surface peak of Sb. This behavior indicates that the crystal is weakly damaged after oxide desorption [61]. Typical defects that cause such dechanneling behavior are point defects, dislocations, and stacking faults [61]. In order to make a statement about the exact type of defect, scanning transmission electron microscopy (STEM) measurements would be necessary. Interestingly, the increase in the dechanneling rate of the sample with the GaSb buffer layer is the lowest. This result shows that the damage to the crystal by the oxide desorption only affects the substrate. The subsequent growth of the GaSb buffer is not affected, which is consistent with the results of the AFM and RHEED measurements. Moreover, the crystal quality of the GaSb buffer even exceeds the quality of the original GaSb wafer. The GaSb buffer layer thus provides perfect starting conditions for CuMnSb growth.

4.2.3 (IN,GA)AS ON INP

The growth of lattice-matched (In,Ga)As buffer layers on InP substrates is carried out according to the method described in [18–20], which is illustrated schematically in Figure 4.6 **a**. To prevent P atoms from desorbing at high substrate temperatures, an As flux with a BEP of 1×10^{-5} mbar is applied for temperatures exceeding 330 °C. The same As flux is also applied during (In,Ga)As growth. For oxide desorption, the substrate is heated at a rate of 50 °C min^{-1}. From 400 °C the heating rate is reduced to 20 °C min^{-1}. Between 500 and 550 °C a 4 × 2 reconstruction can be observed by RHEED. The start of the oxide desorption is indicated by a transformation of this 4 × 2 reconstruction to a 2 × 4 reconstruction. To ensure complete removal of the
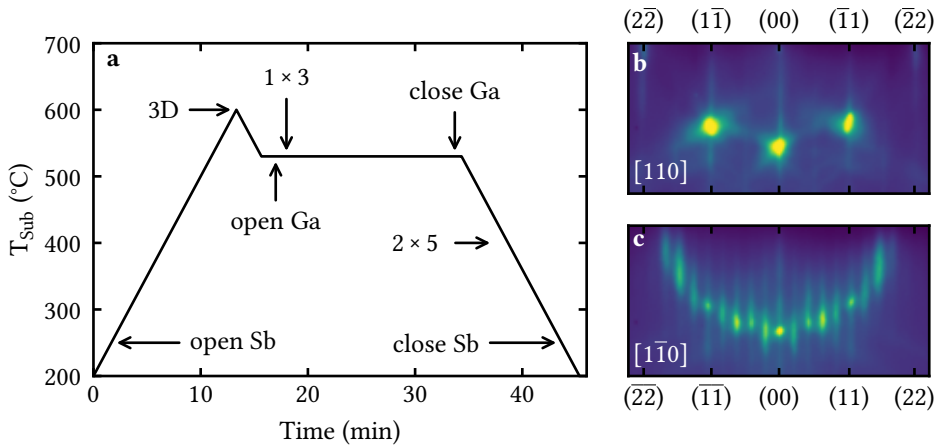
Figure 4.6: **Temperature development of the substrate during (In,Ga)As buffer growth with critical process milestones together with the surface reconstruction observed after growth. a** The transformation from 4 × 2 to 2 × 4 of the surface reconstruction indicates the start of the oxide desorption. When the growth of (In,Ga)As is initiated by opening the In and Ga cell shutters, the surface reconstruction changes back to 4 × 2 under the appearance of 3D dots. During cooldown after growth, the reconstruction changes to 4 × 3 as it is shown in **b** and **c**. **b** d/4 reconstruction in [110] crystal direction. **c** d/3 reconstruction in [1$\bar{1}$0] crystal direction.

oxide, the substrate is heated by an additional 10 °C.

The substrate is then cooled to the growth temperature, which is equivalent to the temperature at which the conversion of the reconstruction from 4 × 2 to 2 × 4 occurs. Simultaneous opening of the In and Ga cell shutters initiates (In,Ga)As growth. Material fluxes with BEPs of approximately 2.5 × 10^{-7} mbar and 1 × 10^{-7} mbar are used for In and Ga, respectively, leading to a growth rate of 10 nm min^{-1}. The exact fluxes must be continuously adjusted for lattice-matched growth over time using measurements of the vertical lattice parameter of the grown (In,Ga)As buffers. At the beginning of the growth, the 2 × 4 reconstruction transforms back to a 4 × 2 reconstruction under the occurrence of 3D dots. After about one minute of growth, the 3D dots disappear, and the 2D 4 × 2 reconstruction is present until the end of the growth. The growth is terminated by closing the In and Ga cell shutters. During cooldown the 4 × 2 reconstruction transforms to a 4 × 3 reconstruction (Figure 4.6 **b** and **c**) at around 450 °C.

The crystal quality of the (In,Ga)As buffer layer is determined by HRXRD measurements. For this purpose, a buffer layer containing 5 % more Ga compared to the composition (In$_{0.53}$,Ga$_{0.48}$)As which is used for lattice-matched growth on InP is considered. The $\omega - 2\theta$-diffractogram in Figure 4.7 **a** shows the separated (004)

Figure 4.7: **Structural characterization of (In,Ga)As buffer layers.** **a** $\omega - 2\theta$-diffractogram of the (004) diffraction peak together with a full dynamical simulation of an $(In_{0.48},Ga_{0.52})$As buffer layer grown on InP ⬚C21.1-1625. The peak separation is realized by slightly increasing the Ga content. The diffractogram of an $(In_{0.53},Ga_{0.48})$As buffer layer ⬚C21.1-815, which is lattice-matched to the InP substrate is shown for comparison. **b** Rocking curve of the (004) diffraction peak of the $(In_{0.48},Ga_{0.52})$As buffer layer. The Voigt profile fit yields a FWHM of 8.4″.

diffraction peaks of the InP substrate and the (In,Ga)As layer together with a full dynamical simulation, which yields a composition of $(In_{0.48},Ga_{0.52})$As and a buffer height of 92 nm. For comparison, a diffractogram of a sample with lattice-matched $(In_{0.53},Ga_{0.48})$As buffer is also shown in Figure 4.7 **a**. In this sample, the diffraction peaks of the buffer and the substrate are superimposed and do not allow separate analysis of the (In,Ga)As diffraction peak. Figure 4.7 **b** shows the rocking curve of the (In,Ga)As (004) diffraction peak. The FWHM of 8.4″, which results from the Voigt profile fit, confirms the high crystal quality of the (In,Ga)As buffer layers.

4.2.4 ZnTe

ZnTe can be grown on both InAs and GaSb buffer layers using the process described below. The main reason for an additional buffer layer of ZnTe is to introduce a highly resistive barrier that mitigates parasitic effects through substrate and buffer layers in lateral transport experiments. Since the low Te doped GaSb substrates already have a conductivity low enough for lateral transport experiments (see [68] for detailed information), an additional ZnTe layer was omitted for transport studies of GaSb-based samples. The surface reconstructions are therefore described in the example of growth on InAs substrates.

For the growth of the ZnTe buffer layer, the sample is transferred to the II-VI-MBE chamber after the III-V-buffer growth without leaving the UHV environment. Fluxes with BEPs of 7×10^{-7} mbar for Zn and 1.3×10^{-6} mbar for Te
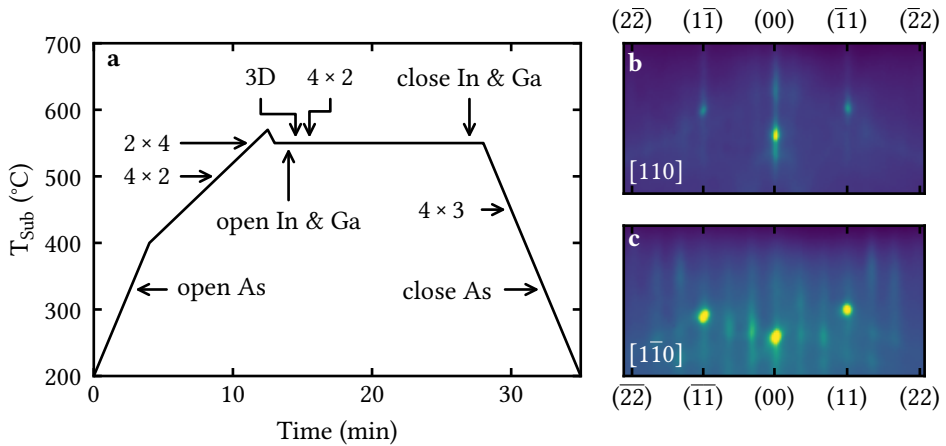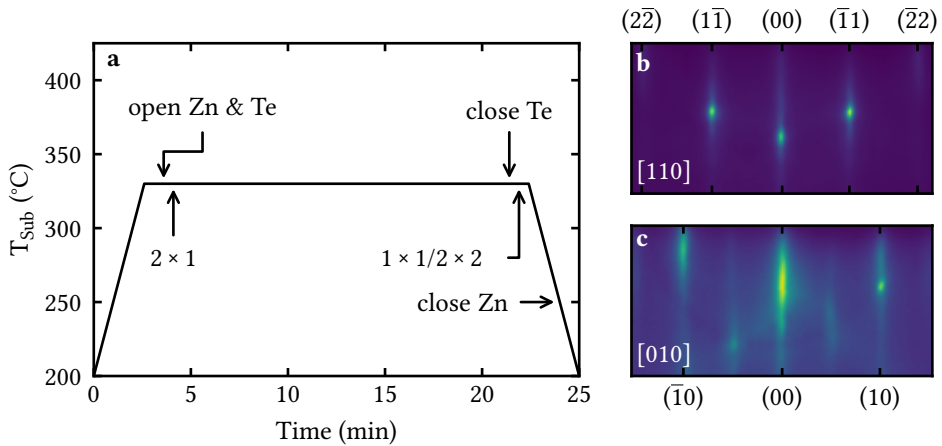
Figure 4.8: **Temperature development of the substrate during ZnTe buffer growth with critical process milestones together with the surface reconstruction observed during and after growth. a** After the substrate is heated to growth temperature, growth is initiated by opening the Zn and Te cell shutters. Within the first minute of growth the surface reconstruction transforms from 2 × 4 to 2 × 1. Closing the Te cell shutter terminates the ZnTe growth. To ensure a Zn-rich surface, Zn flux is applied during cooling. For the Zn-rich surface a 1 × 1 reconstruction in [110] and [1$\bar{1}$0] direction and a 2 × 2 reconstruction in [100] and [010] direction is observed. **b** d/1 surface reconstruction of the Zn-rich surface in [110] crystal direction. **c** d/2 surface reconstruction of the Zn-rich surface in [010] crystal direction.

are used to achieve Te-rich growth at a rate of 6 nm min^{-1}. The sample is heated at a rate of 50 °C min^{-1} to the growth temperature of 330 °C. This and all subsequent steps are shown in the overview of process steps in Figure 4.8 **a**.

Once the sample is stabilized at the growth temperature, the shutters of the Zn and Te cells are opened simultaneously to start growth. Immediately after opening the cell shutters, the 2 × 4 reconstruction of the InAs surface disappears. After approximately 30 s, a 2 × 1 reconstruction develops, which is typical of Te-rich growth. This reconstruction remains unchanged during growth. Growth is terminated by closing the shutter of the Te cell. The resulting Zn-rich surface causes the 2 × 1 reconstruction to transform into a 1 × 1 reconstruction in [110] and [1$\bar{1}$0] directions and a 2 × 2 reconstruction in [100] and [010] directions. Figure 4.8 **a** and **b** show these reconstructions exemplarily for the [110] and [010] directions. During cooling, Zn flux is applied down to a substrate temperature of 250 °C to ensure a Zn-rich surface.

Figure 4.9 **a** shows the $\omega - 2\theta$-diffractogram of the (002) diffraction peak of a ZnTe buffer layer grown on InAs. Well-defined thickness fringes indicate a uniform
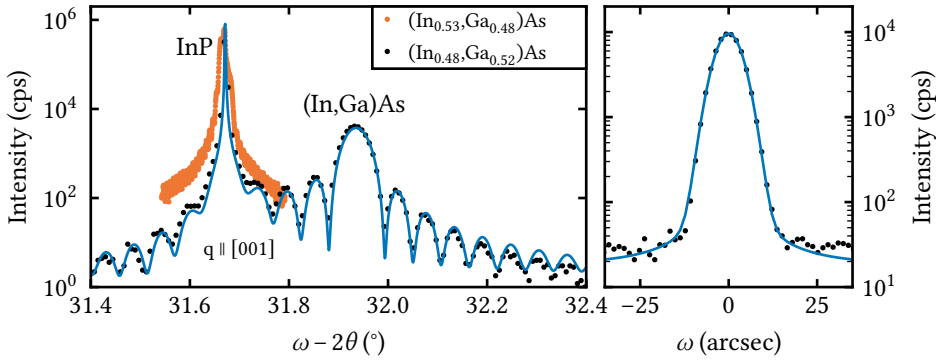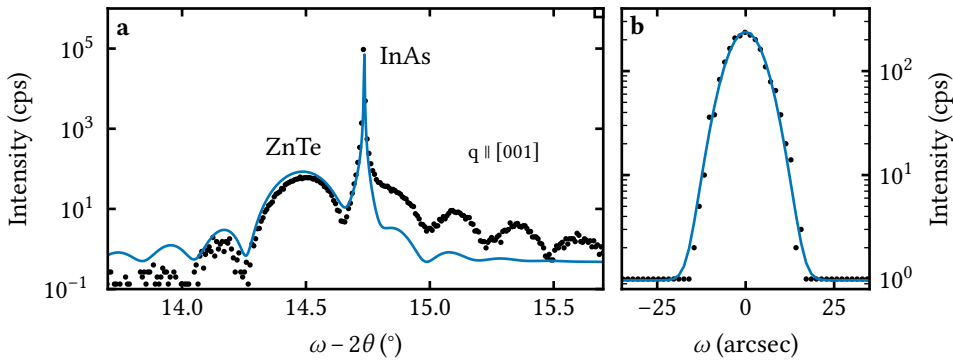
Figure 4.9: **Structural characterization of ZnTe buffer layers.** 📚 Y421   **a** $\omega - 2\theta$-diffractogram of the (002) diffraction peak together with a full dynamical simulation. The poor agreement of the fit away from the layer diffraction peaks can be explained by the low intensity of the thickness fringes at small angles. The low intensity at small angles is probably due to a slight misalignment of the sample, which cannot be taken into account by the simulation. However, this is not a problem for the parameters to be extracted. **b** Rocking curve of the (002) ZnTe diffraction peak. The Voigt profile fit yields a FWHM of 11.4″.

layer thickness. The full dynamical simulation yields a thickness of 21.7 nm and a vertical lattice parameter of 6.168 Å for the ZnTe layer. Excellent crystal quality is demonstrated by the FWHM of the rocking curve of the (002) diffraction peak in Figure 4.9 **b**. The Voigt profile fit yields a FWHM of 11.4″, indicating a low mosaicity. More extensive structural characterization of the ZnTe buffer layers can be found in subsection 5.1.1 (Figure 5.4).

4.3 Layer growth by MBE

Layer growth of NiMnSb and CuMnSb is performed in a MBE-chamber dedicated to Heusler growth. It is equipped with single filament effusion cells for Ni, Mn, and Sb and a dual filament effusion cell for Cu. The cells are first heated to the required temperatures in preparation for growth. Then, the cell shutters are cleaned from deposits that can accumulate on the shutters when they are cool by opening and closing them sequentially five times, maintaining each state for 5 min. Once the chamber is prepared for growth, the sample is transferred into the chamber after buffer growth without leaving the UHV.

4.3.1 NiMnSb

The epitaxy of NiMnSb is a well-established process that is applied without modification in this work [18–20]. Therefore, only a brief description of the basic process

is given here.

Before growth, the sample is heated to the growth temperature of 250 °C. Since the growth of NiMnSb does not occur in a self-stabilized regime, such as the growth of the III-V-buffers, even minor fluctuations in material flux have a significant impact on the material composition. Opening a cell shutter can introduce a thermal perturbation into the cell/material system large enough to alter the material flux of the cell concerned. This is circumvented by opening the cell shutters 5 min in advance of growth of NiMnSb is initiated by opening the main shutter.

Within the first minutes of growth, the 4 × 3 surface reconstruction of (In,Ga)As slowly transforms into a 2 × 1 reconstruction. In the case of stoichiometric growth conditions, this surface reconstruction remains unchanged until growth is terminated by closing the main shutter. The sample is then cooled and transferred out of the chamber for further processing.

4.3.2 CuMnSb

The growth of CuMnSb is carried out, like the growth of NiMnSb, at a substrate temperature of 250 °C, although no significant differences in growth were observed for substrate temperatures up to 300 °C. Due to the similarity of the growth process to that of NiMnSb, it is obvious that for the growth of CuMnSb too, the smallest fluctuations in the material fluxes can have a significant effect on the material composition. For this reason, the cell shutters are also opened 5 minutes before growth starts to stabilize the material fluxes.

The necessity of this procedure becomes clear when looking at the flux measurements of Cu (Figure 4.10 **a**), Mn (Figure 4.10 **b**) and Sb (Figure 4.10 **c**), which were carried out at the sample position using a Bayard-Alpert-type ionization gauge. In the beginning, the measurements show the pressure with the cell shutter closed. After about 5 min, the cell shutter is opened for 10 min, which can be seen from the sharp increase in pressure. Immediately after opening the cell shutter, the flux reaches its maximum, whereupon it slowly decreases until it finally stabilizes after about 5 min. BEPs given in this thesis for the growth of CuMnSb are always calculated by the difference between this pressure reached after stabilization and the pressure just before the opening of the cell shutter from such flux measurements. Once the cell shutter is closed again, the pressure briefly drops below that which was present prior to opening, due to the gettering behavior of the evaporated materials.

After stabilizing the material fluxes, CuMnSb growth is initiated by opening the main shutter. The growth is monitored by RHEED as explained in section 3.1 for all samples dedicated to growth development. Figure 4.11 summarizes the development of the RHEED reconstructions in [110] and [1$\bar{1}$0] crystal directions during growth using the example of a stoichiometric CuMnSb layer grown on InAs.
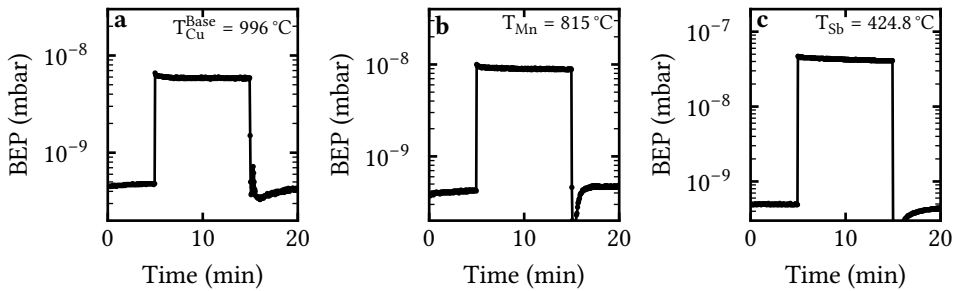
Figure 4.10: **Flux measurements of the materials used for CuMnSb growth.** The beginning and end of the measurements each show a 5 min time frame with the cell shutter closed. In the center, a period of 10 min is measured with the cell shutter open, which can be recognized by the significantly increased pressure. The measurements for Cu (**a**), Mn (**b**) and Sb (**c**) show a maximum pressure just after opening the cell shutter. Subsequently, the pressure decreases slightly and finally stabilizes.

Before growth starts, the InAs buffer surface shows a typical 2 × 4 reconstruction, with clearly visible Kikuchi lines (Figure 4.11 **a** and **b**) indicating a high degree of both bulk and surface order. The waterfall plots in Figure 4.11 **c** and **d** show the time evolution of the RHEED intensities extracted from the individual images taken from the RHEED reconstructions, starting 5 min before growth was initiated with the InAs 2 × 4 reconstruction. As soon as the main shutter is opened, the RHEED intensity decreases, which is attributed to the formation process of the InAs/CuMnSb interface. Within the first 2 min of CuMnSb growth (approx. 1 unit cell), the 2 × 4 reconstruction transforms to a blurry 2 × 2 pattern and the intensity increases. With increasing CuMnSb thickness, the 2 × 2 intensifies and remains unchanged until the growth is terminated by closing the main shutter. The 2 × 2 surface reconstruction at the end of growth is depicted in Figure 4.11 **e** and **f**, where the points of enhanced intensity originate from a crossing of the Kikuchi lines with the elastic diffraction streaks of the CuMnSb surface [40].

During CuMnSb growth, specular spot oscillations can be observed as highlighted by the magnified section of the (00) streak in Figure 4.11 **d**, indicating layer-by-layer growth. Intensity oscillations are also observed for streaks of higher order as indicated by the magnified section of the $(1\bar{1})$ streak in Figure 4.11 **c**. For further investigation of these oscillations, the intensities of the main streak and of the first-order streaks are plotted in Figure 4.11 **g** for the [110] direction and in Figure 4.11 **h** for the $[1\bar{1}0]$ direction as a function of growth time. As can be seen, the oscillations of the first order streaks $[(1\bar{1})$ and $(\bar{1}1)]$ in [110] direction show a larger amplitude than the (00) main streak, while in $[1\bar{1}0]$ direction the exact opposite behavior can be observed. A complete interpretation for this phenomenon
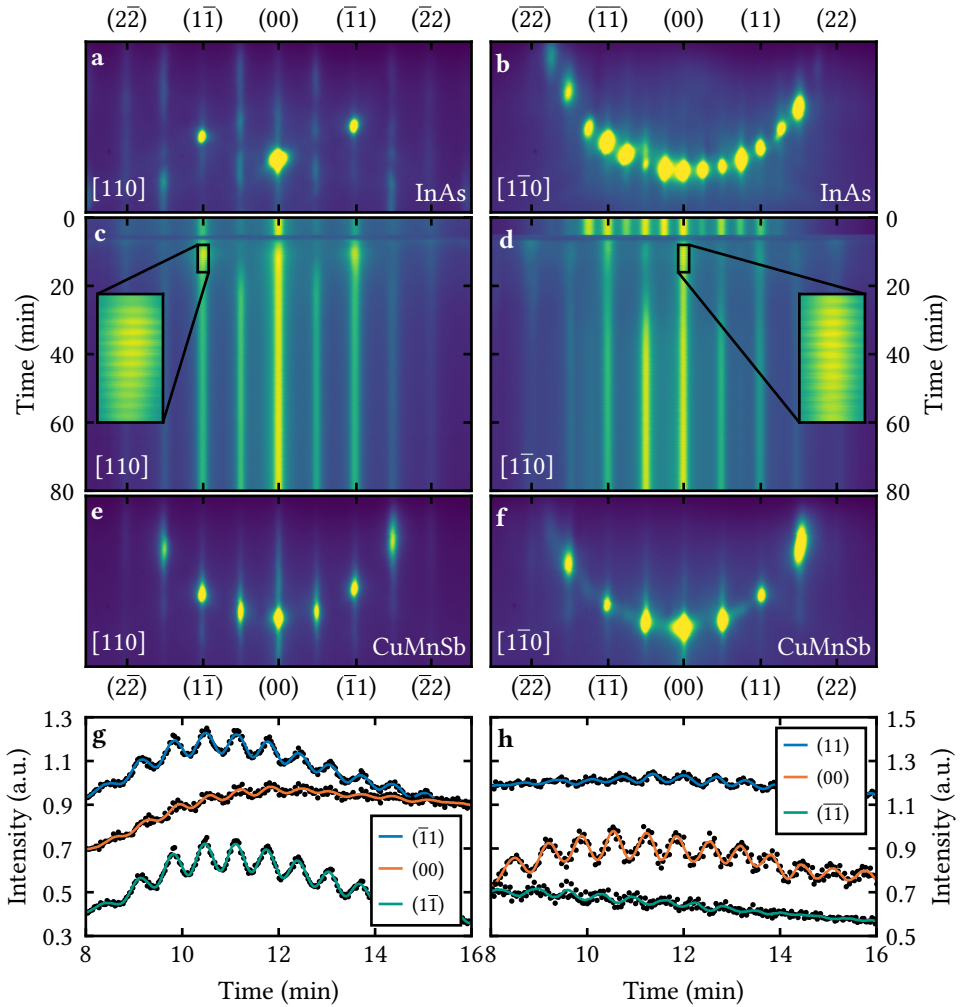
Figure 4.11: **RHEED development during CuMnSb growth.** **a** d/2 surface reconstruction of the InAs surface in [110] crystal direction. **b** d/4 surface reconstruction of the InAs surface in [1$\bar{1}$0] crystal direction. **c** Waterfall plot of the time evolution of the RHEED intensities in [110] crystal direction. The magnified section indicates intensity oscillations of the first-order streak. **d** Waterfall plot of the time evolution of the RHEED intensities in [1$\bar{1}$0] crystal direction. The magnified section indicates specular spot oscillations. **e** d/2 surface reconstruction of the CuMnSb surface in [110] crystal direction. **f** d/2 surface reconstruction of the CuMnSb surface in [1$\bar{1}$0] crystal direction. **g** Intensity oscillations in [110] crystal direction. **h** Intensity oscillations in [1$\bar{1}$0] crystal direction.

has not yet been found, but it could be related to the step-like surface of the epitaxial CuMnSb layers, with the steps showing a strong directional dependence (see

Material	InAs		GaSb	
	T (°C)	BEP (mbar)	T (°C)	BEP (mbar)
Cu (Tip/Base)	1080/996	5.5×10^{-9}	1080/1000	5.8×10^{-9}
Mn	815	8.7×10^{-9}	817	9.0×10^{-9}
Sb	424.8	4.1×10^{-8}	425.2	4.2×10^{-8}

Table 4.1: **Optimized growth parameters for CuMnSb growth on InAs and GaSb.** The given temperatures should be treated as initial guidelines since they can change (e.g. due to changing fill levels of the cells).

subsection 5.1.1), as observed for the growth of other materials [70]. Comparing the oscillation frequency with the layer thickness measured by HRXRD, one oscillation period (1 monolayer (ML)) can be related to the growth of half a unit cell of CuMnSb. This leads to a growth rate of (0.025 ± 0.002) ML/s or (0.41 ± 0.03) atoms/nm^{2}s, corresponding to an atomic flux of (0.14 ± 0.01) atoms/nm^{2}s for Cu and Mn. Due to the low substrate temperature of 250 °C, re-evaporation of these two materials can be neglected. For Sb, on the other hand, re-evaporation cannot be excluded. Thus, the atomic flux of Sb may be slightly higher.

The growth of stoichiometric CuMnSb on InAs and GaSb is realized using the growth parameters given in Table 4.1. Since the perfect growth parameters can change (e.g., due to changing fill levels of the cells), the values given are only to be regarded as initial guidelines. For more advanced calibrations towards a stoichiometric layer, please refer to chapter 5.

After CuMnSb growth, the sample is cooled down. Once the substrate temperature is below 200 °C, the sample is transferred out of the chamber for further processing.

4.4 Sᴘᴜᴛᴛᴇʀ ᴅᴇᴘᴏꜱɪᴛɪᴏɴ ᴏꜰ ᴄᴀᴘᴘɪɴɢ ʟᴀʏᴇʀꜱ

After layer growth by MBE, the samples are capped with a protective layer. This is necessary to prevent oxidation of the half-Heusler layers [71]. Depending on the application of the sample, either Ru or Al_2O_3 is used as a capping layer. Both materials are deposited at room temperature in the sputtering chamber, which is connected to the UHV cluster.

4.4.1 Rᴜ

The deposition of Ru capping layers is performed by direct current (DC)-magnetron sputtering with an Ar pressure of 5×10^{-3} mbar. In combination with a DC-power of 50 W, a deposition rate of 5 nm min^{-1} is achieved. To protect the samples from the environment, a Ru layer of 5 nm thickness has proven to be sufficiently thick. After Ru deposition, the sample is removed from the UHV cluster.
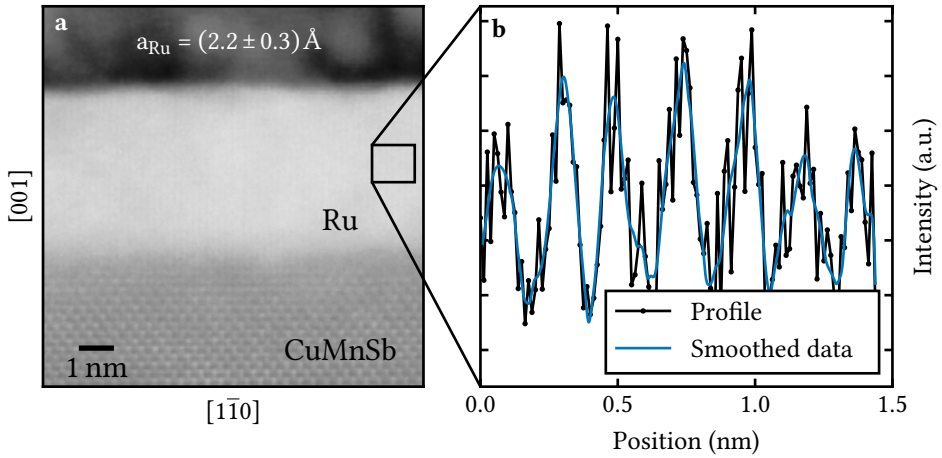
Figure 4.12: **STEM studies of the Ru/CuMnSb interface.** **a** STEM image of the Ru/CuMnSb interface 🍃 H1202 along the [110] crystal direction showing a partially crystalline Ru layer. **b** Horizontal intensity profile of the marked area in **a**. The average spacing of the maxima yields a horizontal lattice parameter of (2.2 ± 0.3) Å for the Ru layer.

STEM imaging has been performed by Martin Kamp at the RÖNTGEN-CENTER FOR COMPLEX MATERIAL SYSTEMS of the JULIUS-MAXIMILIANS-UNIVERSITÄT WÜRZBURG for further investigation of the Ru capping layer. The STEM image of the Ru/CuMnSb interface along the [110] crystal direction in Figure 4.12 **a** indicates a partially crystalline order of the Ru layer. Extracting a horizontal profile of the intensities along the Ru layer yields the curve in Figure 4.12 **b**. The average spacing of the intensity maxima leads to a horizontal lattice parameter of the Ru layer of (2.2 ± 0.3) Å. Furthermore, the interface appears partially smeared, which could indicate diffusion of Ru into the upper CuMnSb layers. It cannot be conclusively determined whether this occurs during the deposition of the Ru layer or during the preparation of the STEM lamella.

When Ru is deposited in a body-centered tetragonal phase, it is believed to exhibit ferromagnetism at room temperature [72]. In the case of the Ru capping layers investigated here, no ferromagnetic behavior in the temperature range of 4 to 300 K was observed in SQUID magnetometry measurements carried out on reference samples consisting of InAs substrate, InAs buffer layer, and Ru protective layer. Considering the lattice parameter of the Ru layer determined in the STEM measurement, it is likely that the Ru capping layers crystallize in a hexagonal close-packed phase, which is non-magnetic [73]. Furthermore, as shown in section 6.2, there is no significant difference in surface magnetism between samples with Ru cap and samples with Al_2O_3 cap. It can therefore be assumed that neither possible

Ru diffusion nor the crystalline Ru phase has any influence on the magnetism of the CuMnSb layers. At this point, a possible RuO_2 oxide layer on the surface of the Ru cap must also be considered, since RuO_2 is antiferromagnetic [74]. In the aforementioned SQUID magnetometry measurements on reference samples, no evidence was found for this either. This is either because the signal of a very thin RuO_2 layer would not be measurable, or, what is much more likely, because no RuO_2 layer forms on the surface, since temperatures above 500 K are necessary for the formation of RuO_2 on a Ru surface [75].

4.4.2 Al$_2$O$_3$

Al_2O_3 is electrically insulating. Using Al_2O_3 as a protective layer is therefore particularly advantageous for samples intended for lateral transport experiments. The deposition of Al_2O_3 on CuMnSb was developed in [76] to use Al_2O_3 not only as a protective layer but also as a tunnel barrier on CuMnSb. This process was adopted in this work for the fabrication of Al_2O_3 protective layers and is described in the following.

First, a 1.5 nm thick Al layer is deposited on the sample by DC-magnetron sputtering at a DC-power of 50 W and an Ar pressure of 5×10^{-3} mbar. The sample is then transferred to the load lock of the sputtering chamber. There, the Al layer is oxidized in pure O_2 for 6 hours. For this purpose, an O_2 pressure of 100 mbar is applied. The described process is then repeated with another Al layer of 1 nm thickness to achieve a total Al_2O_3 thickness of 2.5 nm. The capped sample is finally removed from the UHV cluster via the load lock of the sputtering chamber.

5

Physical properties of epitaxial CuMnSb

The purpose of this chapter is to present the physical properties of epitaxial CuMnSb. In particular, the influence of the material composition on the physical properties will be addressed. Since the substrate material does influence the material properties, this chapter is divided into two sections. First, the properties of CuMnSb grown on InAs are discussed. Those of CuMnSb grown on GaSb are discussed subsequently. At the end of each section, an explanation of how to achieve stoichiometric growth based on physical properties is presented.

5.1 Physical properties of epitaxial CuMnSb grown on InAs (001)

This section is largely based on *L. Scheffler et al., Molecular beam epitaxy of the half-Heusler antiferromagnet CuMnSb, Phys. Rev. Materials **4**, 114402 (2020)* [77].

5.1.1 Structural properties

Surface properties

The surface of epitaxial CuMnSb grown on InAs substrates is investigated in real space by AFM and in reciprocal space by RHEED. As mentioned in subsection 4.3.2, a 2×2 surface reconstruction along the [110] and [1$\bar{1}$0] crystal directions is observed for stoichiometric CuMnSb grown on InAs. Figures 5.1 **a**-**d** show the surface reconstructions of a stoichiometric CuMnSb layer along all four major crystal directions, [100], [010], [110] and [1$\bar{1}$0], after growth. As shown in Figures 5.1 **a** and **c**, a 2×2 surface reconstruction is also present in the [100] and [010] crystal directions.
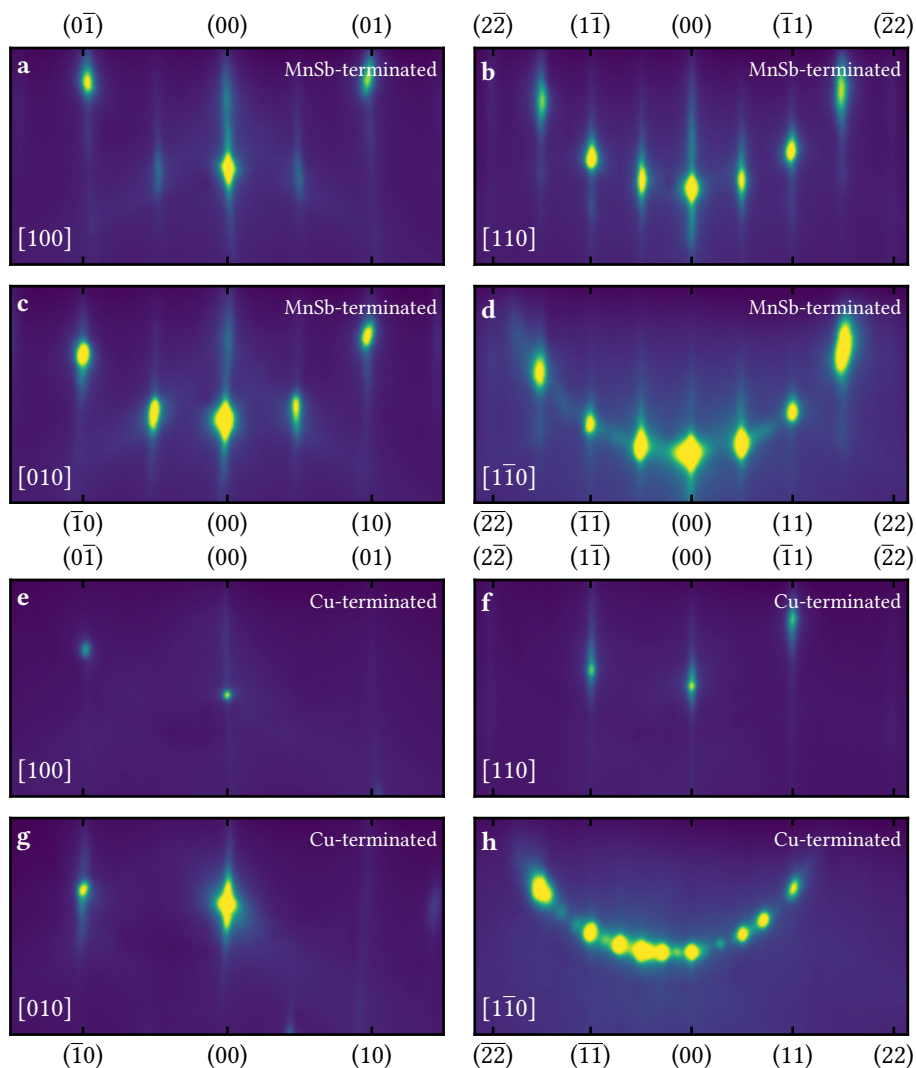
Figure 5.1: **RHEED reconstructions of the CuMnSb surface for layers grown on InAs.**
a-d Surface reconstructions of the MnSb-terminated CuMnSb surface ⬳H1202 along the
four major crystal directions [100], [010], [110] and [1$\bar{1}$0]. **e-f** Surface reconstructions of
the Cu-terminated CuMnSb surface ⬳H1229 along the four major crystal directions [100],
[010], [110] and [1$\bar{1}$0].

For growth on (001) substrates, the examined CuMnSb surface is a (001) plane
of the CuMnSb crystal. There are two types of occupied (001) planes in the CuMnSb
crystal and thus two possible terminations of the CuMnSb surface. One is exclu-
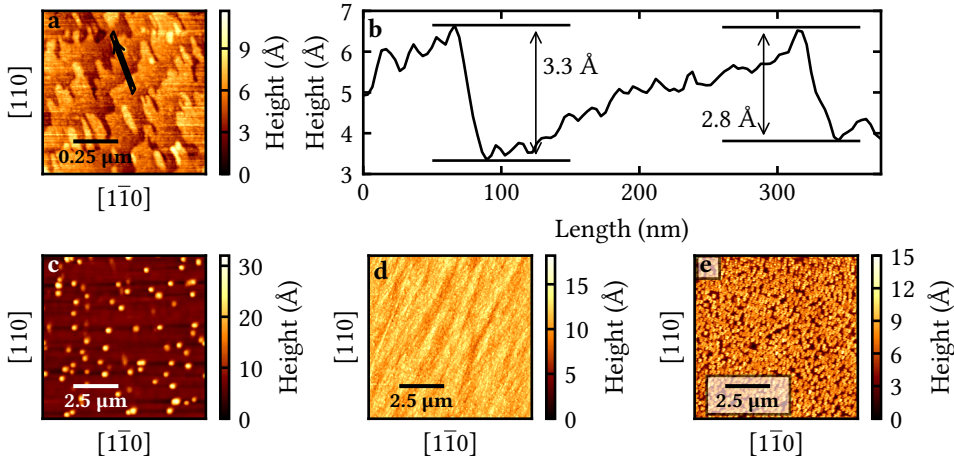
Figure 5.2: **AFM investigations of the Ru capped CuMnSb surface for samples grown on InAs.** **a** AFM image of a stoichiometric CuMnSb layer [H1202]. **b** Line profile extracted from the highlighted area in **a**. **c** AFM image of a CuMnSb layer grown with too little Sb flux [H1192]. **d** Larger area AFM image of a stoichiometric CuMnSb layer [H1202]. **e** AFM image of a CuMnSb layer grown with too much Sb flux [H1217].

sively occupied by Cu atoms and the other consists of Mn and Sb atoms. To find out which of these two possible terminations is present for the 2 × 2 surface reconstruction, two stoichiometric CuMnSb layers are grown with this reconstruction. For one of the layers, only the Cu cell shutter is closed at the end of growth. In this case, no change in surface reconstruction is detected. For the second layer, growth is terminated by closing the cell shutters of Mn and Sb. Here, the surface reconstruction changes within one minute to a 1 × 4 reconstruction in [110] and [1$\bar{1}$0] crystal directions and to a 1 × 1 reconstruction in [100] and [010] crystal directions, as can be seen in Figures 5.1 **e-h**. Consequently, it is very likely that the CuMnSb films fabricated by the growth process described in subsection 4.3.2 have an MnSb-terminated surface. Together with the frequency of the specular spot oscillations, which indicate layer-by-layer growth of monolayers of the thickness of half a unit cell, it can be assumed that a monolayer consisting of the atomic layers MnSb-Cu-MnSb is chemically stable. To date, this characteristic of CuMnSb monolayers has not been reported in the literature. In order to confirm this hypothesis, further investigations of the CuMnSb surface, e.g. by scanning tunneling microscopy, are necessary.

The fact that CuMnSb monolayers with the thickness of half a unit cell are chemically stable is supported by the AFM image of the Ru capped CuMnSb surface in Figure 5.2 **a**. It reveals the presence of atomic steps on the surface with a two to

three times higher density compared to the InAs surface (Figure 4.3 **a**) and a low RMS roughness of 0.14 nm. The line profile in Figure 5.2 **b** shows that the steps are of the height of half a lattice parameter. It is assumed that the Ru capping layer is conformal since it is deposited by sputtering. Therefore, the surface of the capped sample should adequately reflect the surface of the CuMnSb layer.

The larger area scans in Figures 5.2 **c-e** demonstrate that AFM imaging can also be of assistance in optimizing the Sb material flux for CuMnSb growth. Figure 5.2 **c** shows the surface of a sample with 2×10^{-9} mbar reduced Sb flux ($\text{BEP}_{\text{Sb}} = 3.9 \times 10^{-8}$ mbar) relative to stoichiometric composition. Compared to the sample with stoichiometric composition (Figure 5.2 **d**), the quality of the surface is significantly reduced. It is covered by dots with heights up to 3 nm. The observed areal density of these dots is ~1 μm^{-2}. Additionally, with an Sb flux increased by 2×10^{-9} mbar ($\text{BEP}_{\text{Sb}} = 4.3 \times 10^{-8}$ mbar), dots can be observed on the surface (Figure 5.2 **e**). However, they occur in a much higher density of ~20 μm^{-2} and are smaller.

5

Layer properties

Structural characterization of the CuMnSb layers grown on InAs substrates is performed by HRXRD, STEM, RBS and PIXE. Figure 5.3 summarizes the HRXRD measurements on a stoichiometric CuMnSb sample. The multiple, well-defined thickness fringes surrounding the layer peak in the $\omega - 2\theta$-diffractogram of the symmetric (002) peak in Figure 5.3 **a** demonstrate a uniform layer thickness. The lattice parameters are extracted using a full dynamical simulation, which is shown along with the experimental data. It yields a horizontal lattice parameter of $a_{\text{CuMnSb}}^{\parallel} = a_{\text{InAs}} = 6.059$ Å and a vertical lattice parameter of $a_{\text{CuMnSb}}^{\perp} = 6.136$ Å, indicating a compressive strained CuMnSb layer. This strain forces the CuMnSb crystal structure from space group $F\bar{4}3m$ to $F\bar{4}2m$, as reported for NiMnSb grown on InP substrates [78]. The thickness of the CuMnSb film is found to be 37 nm. Crystal quality is investigated using the rocking curve in Figure 5.3 **b**. A low FWHM of 7.7 ″ indicates low mosaicity and thus high crystalline order. No degradation can be seen compared to the InAs substrate, making the substrate quality the limiting factor.

Figure 5.3 **c** shows the RSM of the asymmetric (224) diffraction peak. The CuMnSb peak appears aligned to the InAs peak along the [00L] direction, confirming pseudomorphic growth of CuMnSb on InAs. Relaxation of the CuMnSb layer can be excluded since there is no broadening of the CuMnSb peak along the depicted relaxation triangle. As described in section 4.4, the CuMnSb layers are capped with Ru or Al$_2$O$_3$ to avoid oxidation. To validate the protection by Ru, the measurement of the RSM was repeated on the same sample one year after growth. The result of this lower resolution measurement is shown in Figure 5.3 **d**. Again, no relaxation of
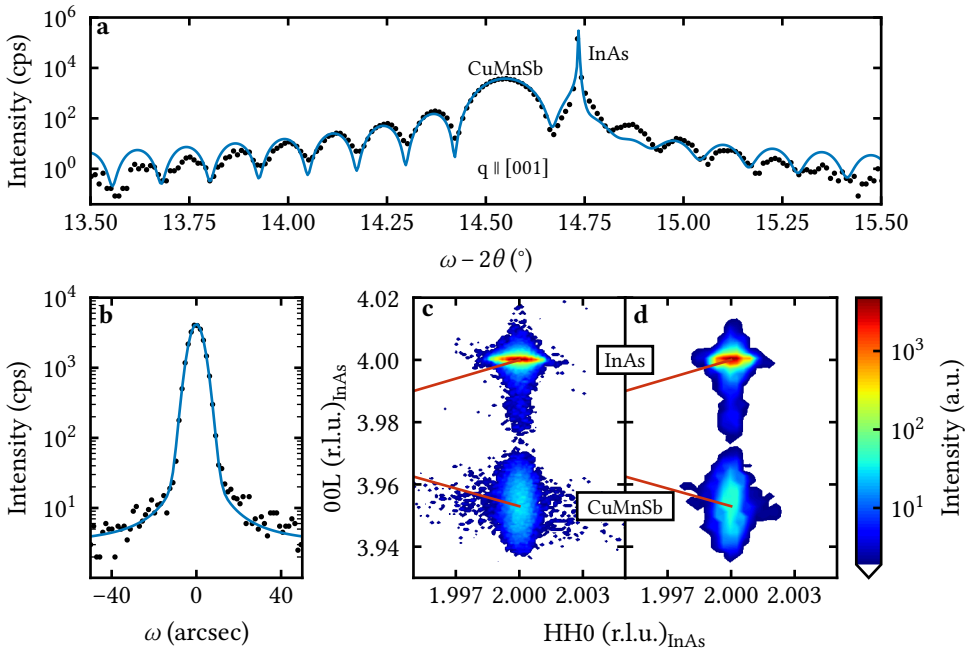
Figure 5.3: **HRXRD investigations of epitaxial CuMnSb grown on InAs.** 📚 H1202
a $\omega - 2\theta$-diffractogram of the symmetric (002) diffraction peak together with a full dynamical simulation yielding the lattice parameters and the CuMnSb thickness. **b** Rocking curve of the (002) CuMnSb diffraction peak. The Voigt profile fit yields a FWHM of 7.7 ″. **c** RSM of the asymmetric (224) diffraction peak, confirming the pseudomorphic character of the CuMnSb layer. The relaxation triangle is shown for the CuMnSb layer. **d** Rerun of the RSM from **c** one year after growth. No signs of aging or oxidation are visible. The reduced resolution of this measurement is due to the use of a different detector.

the CuMnSb layer can be seen, and the CuMnSb peak is aligned to the InAs peak in [00L] direction, providing no evidence of aging or oxidation of the CuMnSb layer.

In order to investigate the influence of an additional ZnTe buffer layer on the epitaxial CuMnSb, three samples with different CuMnSb and ZnTe layer thicknesses (20 nm ZnTe / 20 nm CuMnSb, 30 nm ZnTe / 30 nm CuMnSb and 300 nm ZnTe / 40 nm CuMnSb) grown on InAs are characterized using HRXRD. The $\omega - 2\theta$-diffractograms of the symmetric (002) peak are presented in Figure 5.4 **a** together with full dynamical simulations for extraction of the lattice parameters and film thicknesses. The measurements are shifted vertically for better visibility. While the measurements of the two thinner samples show superimposed thickness fringes of the CuMnSb and ZnTe layers, no thickness fringes are visible for the thickest sample. This finding indicates a relaxation of the CuMnSb layer on the
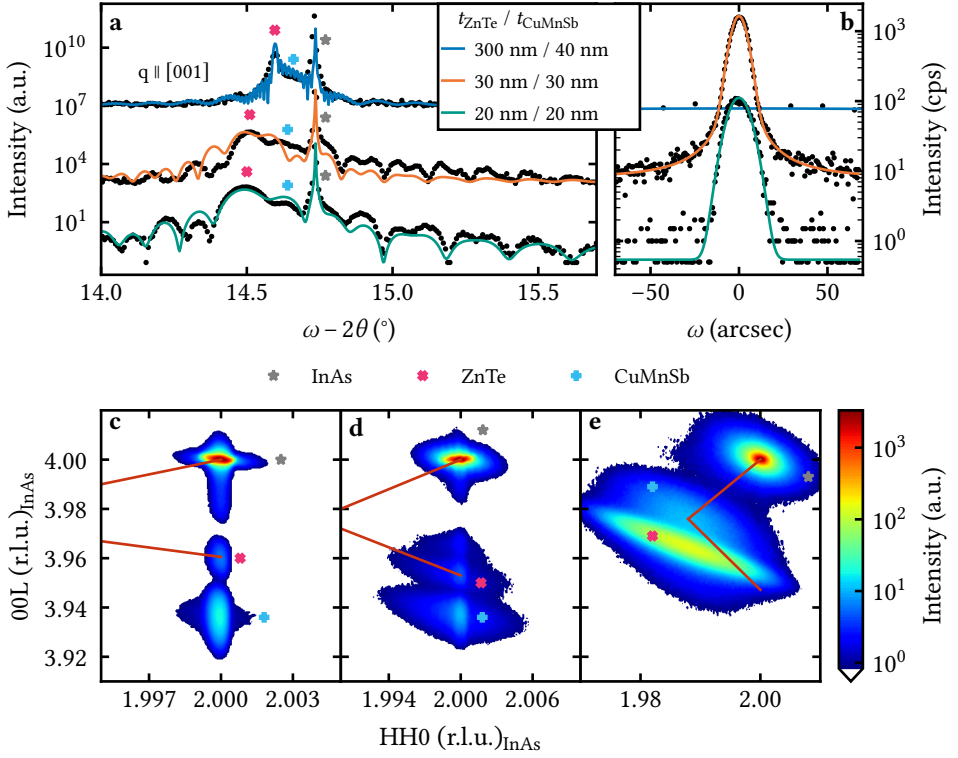
Figure 5.4: **HRXRD investigations of epitaxial CuMnSb grown on ZnTe buffer layers of different thicknesses. a** $\omega - 2\theta$-diffractograms of the symmetric (002) diffraction peak together with full dynamical simulations for extraction of lattice parameters. The measurements are shifted vertically for better visibility. **b** Rocking curves of the (002) CuMnSb diffraction peak. **c** RSM of the (224) diffraction peak of the sample with layer thicknesses of 20 nm ZnTe / 20 nm CuMnSb H1253. **d** RSM of the (224) diffraction peak of the sample with layer thicknesses of 30 nm ZnTe / 30 nm CuMnSb H1252. **e** RSM of the (224) diffraction peak of the sample with layer thicknesses of 300 nm ZnTe / 40 nm CuMnSb H1164.

thickest sample. It is not possible to draw conclusions about the thickness fringes of the thick ZnTe layer, as these would have a higher frequency at a ZnTe thickness of 300 nm than the distance between the individual measuring points.

The two thinner samples have the same vertical lattice parameters, which are $a^{\perp}_{\text{CuMnSb}} = 6.136\,\text{Å}$ and $a^{\perp}_{\text{ZnTe}} = 6.190\,\text{Å}$. A thin ZnTe buffer layer, therefore, does not influence the vertical lattice parameter of the CuMnSb layer. For the thick sample, only the ZnTe peak is clearly visible. It yields a vertical lattice parameter of $a^{\perp}_{\text{ZnTe}} = 6.115\,\text{Å}$. The reduction of $a^{\perp}_{\text{ZnTe}}$ suggests that the ZnTe layer of the thickest sample is relaxed as well, at least partially.

The influence of ZnTe buffer layers on the crystal quality of the CuMnSb layer is investigated by the rocking curves of the (002) CuMnSb diffraction peak in Figure 5.4 **b**. The Voigt profile fits yield FWHMs of 13.7 ″ and 9.6 ″ for the samples with thicknesses of 20 nm ZnTe / 20 nm CuMnSb, 30 nm ZnTe / 30 nm CuMnSb, respectively. Within the limits of the diffractometer, this is no worsening compared to CuMnSb layers grown directly on the InAs buffer layer. In contrast, the rocking curve of the 40 nm CuMnSb layer on the 300 nm ZnTe layer shows a FWHM of 977.8 ″, indicating a strong degradation of the crystal.

Pseudomorphism and relaxation of the CuMnSb and ZnTe layers are examined in more detail using RSMs of the (224) diffraction peak in Figures 5.4 **c**-**e**. The RSM of the thinnest sample (Figure 5.4 **c**) confirms the pseudomorphic character of both the CuMnSb and the ZnTe film, as both layer peaks are aligned to the InAs peak in [00L] direction. No broadening along the depicted relaxation triangle is visible. Pseudomorphic growth can also be attested for the sample with layer thicknesses of 30 nm ZnTe / 30 nm CuMnSb (Figure 5.4 **d**), while little broadening along the relaxation triangle is visible for both layers. As already indicated by the $\omega - 2\theta$-diffractogram, the RSM of the thickest sample (Figure 5.4 **e**) shows fully relaxed CuMnSb and ZnTe layers. The position of the relaxed CuMnSb peak yields a relaxed lattice parameter of $a_{\text{CuMnSb}}^{\text{relaxed}} = 6.095\,\text{Å}$, which matches the value reported for bulk CuMnSb [26]. Using this value, the compressive strain on the epitaxial CuMnSb layers grown on InAs substrates can be calculated as 0.6 %. Furthermore, it should be noted that the combined layer thickness of ZnTe and CuMnSb for pseudomorphic growth is limited by the lattice mismatch to InAs.

Further characterization of the CuMnSb crystal is performed using STEM imaging. Therefore, a lamella with its surface normal along the [110] crystal direction is prepared in a focused ion beam (FIB) system. For this orientation, only atoms of the same species are aligned along the line of sight. The STEM images are recorded at a 300 kV acceleration voltage with a high-angle annular dark-field (HAADF) detector at the Röntgen-Center for Complex Material Systems of the Julius-Maximilians-Universität Würzburg by Dr. Martin Kamp. Figure 5.5 **a** shows an overview scan of the InAs/CuMnSb/Ru layer stack. While the Ru and InAs layers appear as smooth films, the CuMnSb layer exhibits buckling, indicating partial relaxation. This can be due to any of two reasons; either the lamella is thin enough to allow the CuMnSb layer to relax, or the CuMnSb layer relaxes due to oxidation because the lamella is exposed to the environment unprotected during the transfer from the FIB system to the STEM system. Besides the partial relaxation of the CuMnSb film, no defects or stacking faults can be observed.

Both epitaxial layers (CuMnSb and InAs) show single crystalline ordering in the higher magnification STEM image shown in Figure 5.5 **b**. The interface between CuMnSb and InAs manifests as a strong contrast in the image and is atomically
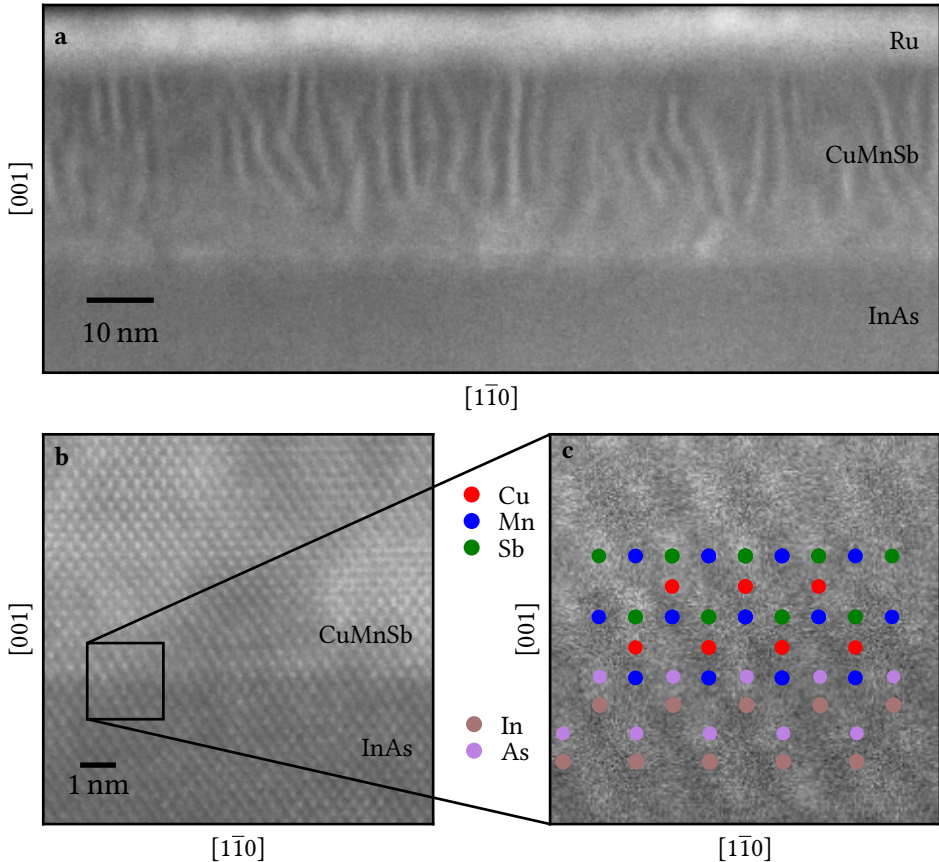
Figure 5.5: **STEM images of epitaxial CuMnSb on InAs.** 📚 H1202 **a** Overview scan of the InAs/CuMnSb/Ru layer stack. Partial relaxation of the CuMnSb film is indicated by buckling. **b** Higher magnification image of the CuMnSb/InAs interface. **c** Magnified section of **b** with overlaid crystal structures of CuMnSb and InAs.

sharp. To map the InAs and CuMnSb crystal structures to the STEM images, the HAADF images of the InAs/CuMnSb layer stack are simulated using the *computem* program developed by Kirkland [79]. The simulation suggests that the heavy atoms (Sb and In) show up as bright spots, while darker areas appear for vacant crystal positions. Furthermore, the As atoms of the InAs surface appear to be incorporated into the first CuMnSb layer by substituting the position of the Sb atoms. Using this information, the crystal structures can be overlaid to the magnified section of the HAADF-STEM image in Figure 5.5 **c**. The alignment proves that the CuMnSb
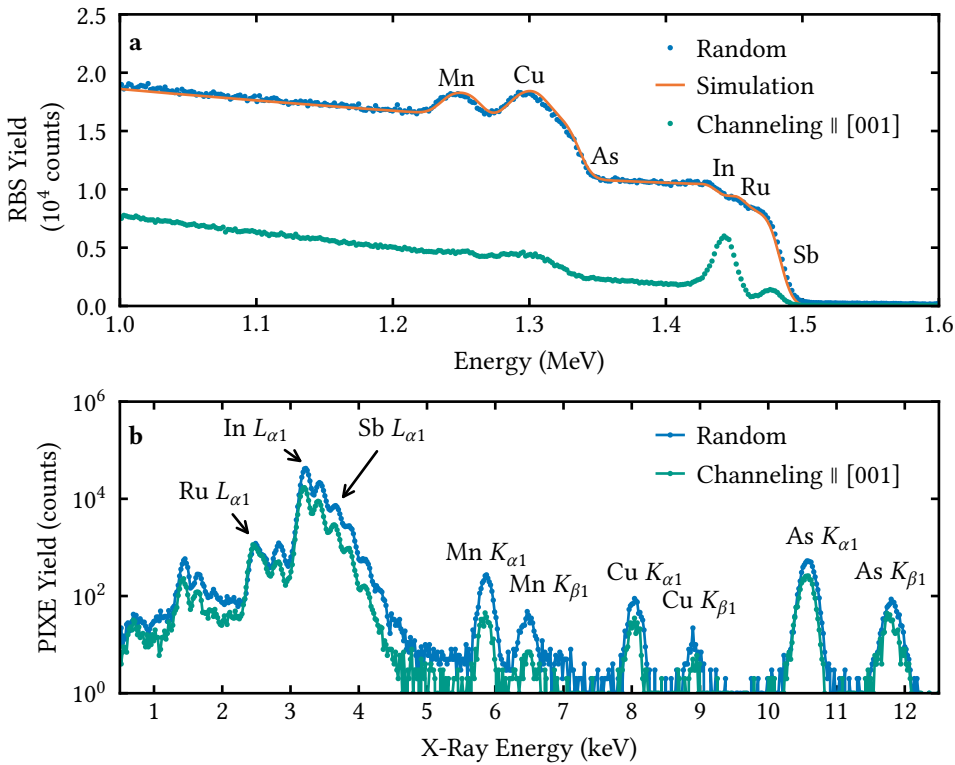
Figure 5.6: **RBS and PIXE spectra of stoichiometric CuMnSb grown on InAs.** ⬙H1202
a RBS spectra in random and channeling configuration, along with a simulation of the random signal for a $Cu_{0.334}Mn_{0.333}Sb_{0.333}$ composed layer. **b** PIXE spectra in random and channeling configuration, along with the associated X-ray emission lines of the elements present in the sample.

layers grow in the expected half-Heusler crystal structure.

Material composition is investigated by RBS and PIXE. The measurements are performed on a sample grown with the growth parameters given in subsection 4.3.2. Figure 5.6 **a** shows the RBS spectra in random and channeling configuration. A simulation of the spectrum in random configuration for a $Cu_{0.334}Mn_{0.333}Sb_{0.333}$ composed layer agrees well with the measurement. Within the limits of the RBS instrument, the studied CuMnSb layer can be considered as stoichiometric. In channeling configuration, the surface peaks of Cu, Mb, Sb, and Ru are visible. The surface peaks of In and As are absent due to the CuMnSb/InAs interface being located too deep in the sample. As the channeling yield increases only gently towards lower energies, the defect density in the CuMnSb layer appears to be low.

The collected PIXE spectra in random and channeling configuration are shown
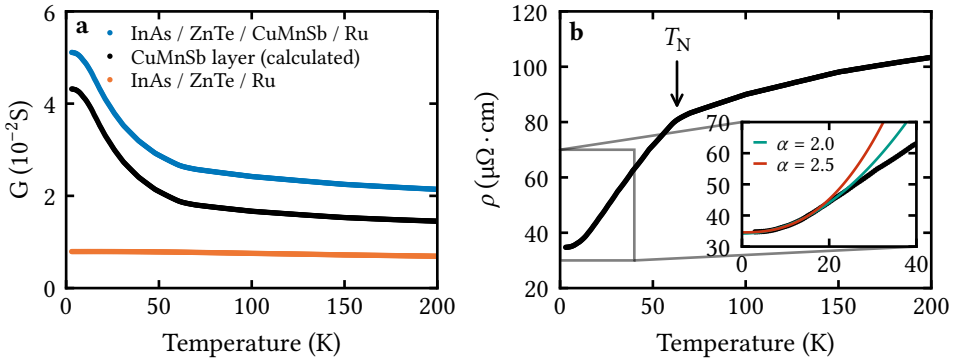
Figure 5.7: **Electrical transport measurements on epitaxial CuMnSb grown on InAs with a ZnTe buffer layer.** ⬢ H1242 **a** Conductance of a reference sample, a sample containing CuMnSb together with the calculated conductance for the CuMnSb layer. **b** Temperature dependent resistivity of epitaxial CuMnSb. The onset of antiferromagnetic order is characterized by a clear kink at 62 K. The inset shows a magnified section of the low temperature regime, together with polynomial fits that yield a residual resistivity of $\rho_0 = 35\,\mu\Omega\cdot\text{cm}$.

in Figure 5.6 **b**, along with the associated X-ray emission lines. Emission lines of all atomic species present in the layer stack are visible in the spectrum. All peaks originating from elements of epitaxial layers have a reduced yield in channeling configuration since their crystalline order allows channeling of the He+ ions. For the sputtered Ru, the yields are identical in random and channeling configuration, indicating amorphous character of the Ru layer.

5.1.2 Electrical properties

Electrical characterization is performed on a 30 nm thick CuMnSb layer grown on a 38 nm thick ZnTe buffer layer. The sample is capped by a 5 nm Ru protective layer. Rectangular stripes with the size of $250 \times 1900\,\mu\text{m}^2$ are prepared by standard optical lithography and physical dry etching. Resistance measurements are carried out in four-point geometry using a DC-current in a standard He bath cryostat with a variable temperature insert. The applied current results in a current density of $1.4 \times 10^3\,\text{A cm}^{-2}$. Contacts for probing the voltage are placed at a distance of 500 µm on the stripes. The magnetic transition and the electrical behavior at low temperatures are investigated by the temperature dependent resistivity of the CuMnSb layer.

To account for the parallel conductance of the Ru cap, the measurements are repeated for a reference sample without the CuMnSb layer. The conductance of this reference sample is then subtracted from the conductance of the sample containing

the CuMnSb layer. Figure 5.7 **a** shows the temperature dependent conductance of the reference sample, the sample containing the CuMnSb layer, and the resulting calculated conductance of the CuMnSb layer. As can be seen, subtracting the reference signal does not add any new features. With a value of $(36 \pm 4)\,\mu\Omega \cdot cm$ at 200 K, the resistivity of the 5 nm thick Ru layer lies above the literature values reported for bulk material (7.5 to $8.2\,\mu\Omega \cdot cm$) [80–82]. At a thickness of 5 nm, finite size effects such as surface scattering or grain boundary scattering are likely to increase resistivity relative to bulk material [83, 84]. Compared to the values of ~$20\,\mu\Omega \cdot cm$ reported for Ru thin films of 5 nm thickness [85], the values obtained here are only slightly larger. A contribution of a potential RuO_2 layer to the measured resistivity is very unlikely for the reasons given in subsection 4.4.1.

The calculated conductance of the CuMnSb layer is then converted to resistivity using the physical dimensions of the fabricated stripe. Figure 5.7 **b** shows the resulting temperature dependent resistivity of the CuMnSb layer. A clear kink of the resistivity is observed at a temperature of 62 K. At the onset of antiferromagnetic ordering, suppression of spin disorder scattering causes this slope change in resistivity [86]. Thus, the temperature of 62 K can be identified as T_N of epitaxial CuMnSb grown on InAs. This lies at the upper end of the range of values reported previously for bulk CuMnSb (50 - 62 K) [21, 23–26].

At low temperatures the temperature dependent resistivity can be fitted using the polynomial function:

$$\rho(T) = \rho_0 + aT^{\alpha}, \tag{5.1}$$

as shown in the inset of Figure 5.7 **b**, where the fits for two temperatures ranges are shown (0 - 15 K and 0 - 25 K). Here, ρ_0 is the residual resistivity, giving information on the scattering of charge carriers on impurities. Scattering between charge carriers is described by the second term [87]. The fits of both temperature ranges yield $\rho_0 = 35\,\mu\Omega \cdot cm$. Compared to the lowest values reported for bulk CuMnSb [26], this value is even lower. Epitaxial growth thus appears to significantly reduce the defect concentration in the CuMnSb crystal. Relative to normal metals, this value is significantly increased, which could be due to the low density of states at the Fermi level, as indicated by first principle calculations for CuMnSb [88]. This theory is supported by the low charge carrier density of $n = 2.3 \times 10^{21}\,cm^{-3}$ determined for epitaxial CuMnSb in the work of Julian Werther [68]. In the same work, Julian Werther was able to determine that electrical transport in epitaxial CuMnSb is hole dominated with a hole mobility of $\mu_h = 65\,cm^2\,V^{-1}\,s^{-1}$.

As can be seen, the value of α is strongly dependent on the temperature range used for the fit. In the lower temperature range of 0 - 15 K, α is determined to be 2.5, which lies well above the values reported for bulk CuMnSb ($\alpha = 2$ [87], $\alpha = 1.8$ [25, 89]). Increasing the temperature range for the fit up to 25 K leads to an $\alpha = 2.0$, which compares well to the previously reported values. Since the value of
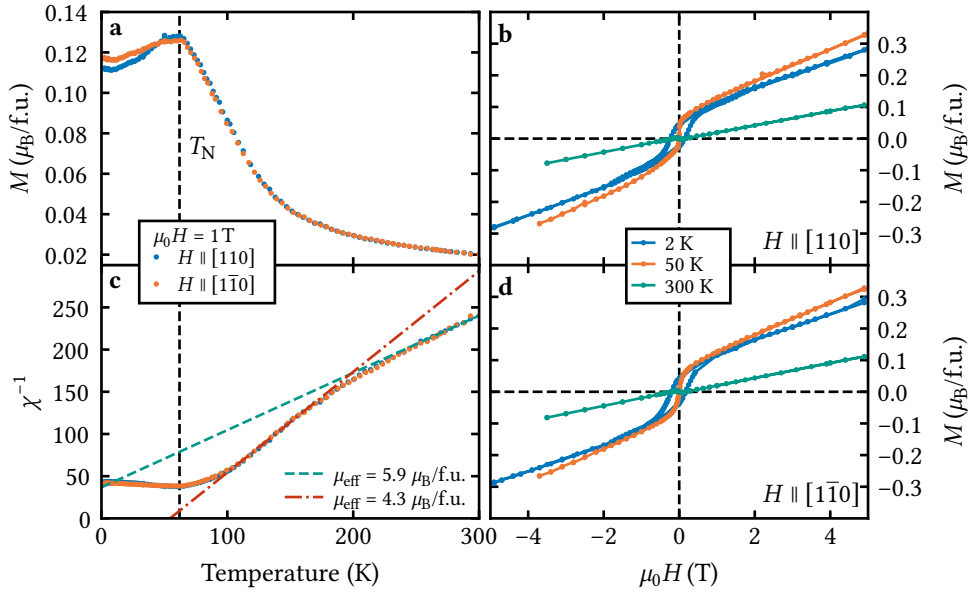
Figure 5.8: **Magnetic characterization of epitaxial CuMnSb grown on InAs.** ⬚ H1202
The measurements are compensated using the CSH method described in section 3.4. **a**
Temperature dependent magnetization during cooldown in a bias field of 1 T. **b** Magnetic
field dependent magnetization along the [110] crystal direction at various temperatures.
c Inverse susceptibility during cooldown in a bias field of 1 T. The dashed lines indicate
the Curie-Weiss fits in the two temperature regimes with linear behavior. **d** Magnetic field
dependent magnetization along the [1$\bar{1}$0] crystal direction at various temperatures.

alpha depends very strongly on the temperature range selected for the fit, it will
be refrained from drawing quantitative conclusions from the determined values at
this point. However, the fact that the value of alpha corresponds approximately
to the value 2, or exceeds 2, fits with the previous observations that CuMnSb is a
semi-metal rather than a half-metal [27, 38, 88]. For half-metals, no T^2 dependence
would be observed at low temperatures, since all states at the Fermi level are spin-
polarized and thus no spin-flip scattering is possible, which is typically responsible
for the T^2 dependence of the resistivity [90, 91].

5.1.3 Magnetic properties
Magnetic behavior of epitaxial CuMnSb grown on InAs is studied as a function of
temperature and magnetic field along the [110] and [1$\bar{1}$0] crystal directions using
the SQUID magnetometer. The measurements are performed on a 40 nm thick
CuMnSb layer capped with Ru. Compensation provided by the CSH allows for
quantitative analysis. Figure 5.8 summarizes the magnetic measurements.

Field cooling (FC) curves of the magnetization $M(T)$ recorded in a bias field of 1 T are shown in Figure 5.8 **a**. As the temperature is reduced, the magnetization increases with a nonlinear progression, indicating paramagnetic behavior of the CuMnSb layer. In this regime, the curves of the two crystal directions coincide. At a temperature of 62 K, the magnetization reaches its maximum before it decreases again towards lower temperatures, resulting in a cusp. This cusp marks the phase transition from paramagnetism to antiferromagetism since the decrease in magnetization is a consequence of antiferromagnetic ordering. The value of T_N obtained by electrical characterization is thus in agreement with the value obtained by the magnetic measurements. Below T_N, a weak anisotropy is observed, similar to that reported for bulk CuMnSb [26].

Further characterization of the paramagnetic phase is carried out based on the temperature dependent inverse susceptibility $\chi^{-1}(T)$, which is shown in Figure 5.8 **c**. Two linear regimes are present in $\chi^{-1}(T)$. Both of them can be fitted by means of the Curie-Weiss law to obtain μ_{eff} and Θ_{CW}. The fits yield μ_{eff} = 5.9 μ_B/f.u. for the temperature regime above 230 K and μ_{eff} = 4.3 μ_B/f.u. for the temperature regime between 110 K and 170 K. These values are within the range of values reported for bulk CuMnSb (3.9–6.3 μ_B/f.u.) [23–26]. Band-structure calculations suggest that CuMnSb carries a magnetic moment of 4 μ_B/f.u. [88]. Assuming that the saturation moment μ_{sat} of the antiferromagnetic and the paramagnetic phases is equal, the expected effective paramagnetic moment μ_{eff} can be calculated following [92] by using the relations:

$$\mu_{\text{eff}} = g\sqrt{J(J+1)}\mu_B \tag{5.2}$$

and

$$\mu_{\text{sat}} = gJ\mu_B \tag{5.3}$$

by

$$\mu_{\text{eff}} = g\sqrt{\frac{\mu_{\text{sat}}}{g\mu_B}\left(\frac{\mu_{\text{sat}}}{g\mu_B}+1\right)}\mu_B, \tag{5.4}$$

with g being the g-factor, and J being the angular momentum quantum number. Using Equation 5.4, the expected effective paramagnetic moment is calculated as μ_{eff} = 4.9 μ_B/f.u.

Differences to bulk samples are found for Θ_{CW}. A Θ_{CW} of −65 K is extracted from the fit in temperature range above 230 K. Typically, a ratio of $-\Theta_{\text{CW}}/T_N \approx 3$ is observed in bulk CuMnSb [26]. This value is interpreted to be indicative of geometric frustration [34]. However, the observation that the ratio is close to 1 in the case of epitaxial CuMnSb grown on InAs indicates that the geometric frustration in the magnetic structure of the CuMnSb film is reduced due to the symmetry reduction caused by the epitaxial strain. The fit of the lower temperature regime yields a positive Θ_{CW} of 55 K, indicating ferromagnetic contributions. More

detailed investigations into this second Curie-Weiss regime close to the magnetic transition can be found in section 6.1.

Figures 5.8 **b** and **d** show the magnetic field dependence of the magnetization along the [110] and [1$\bar{1}$0] crystal directions for various temperatures. As expected for the paramagnetic phase, the magnetization at 300 K shows linear behavior as a function of the magnetic field for both crystal directions. No saturation is observed for magnetic fields up to 5 T. Below T_N, non-saturating linear behavior is observed for $|\mu_0 H| \gtrsim 0.8$ T, as was demonstrated for bulk CuMnSb in fields up to 50 T [93]. For smaller fields, however, the magnetization shows nonlinear behavior. While no remanence can be observed close to T_N at 50 K, an open hysteresis develops at 2 K, which is atypical for antiferromagnets. The saturation magnetization of the nonlinear signals shows a weak anisotropy between the two crystal directions. Hysteretic behavior at low temperatures and low magnetic fields was also found for bulk samples. Spin disorder was suggested as the origin [27]. Whether the nonlinear behavior of the epitaxial CuMnSb layers is of the same origin will be investigated in detail in section 6.1.

Except for the nonlinear behavior at low magnetic fields, the magnetic measurements confirm the antiferromagnetic character of epitaxial CuMnSb thin films grown on InAs. In particular, the characteristic parameters, like T_N and μ_eff are consistent with the values published for bulk CuMnSb.

5.1.4 Achieving stoichiometry

Finding and setting the correct growth parameters for the stoichiometric growth of CuMnSb on InAs is primarily an iterative process, where the growth parameters have to be adjusted based on sample properties after each growth until the right conditions are determined. No correlation has yet been found between the structural parameters determined by HRXRD, like the vertical lattice constant, and the material composition for the growth of CuMnSb on InAs. It is nevertheless advisable to characterize all samples with rocking curves and $\omega - 2\theta$-diffractograms to exclude additional material phases and to assess the crystal quality.

However, some characteristic surface reconstructions observed by RHEED could be identified, which allow conclusions to be drawn about the deviation of the growth parameters from the stoichiometric case. The known RHEED patterns along with the resulting information on material flux conditions are shown in Figure 5.9. Thus, it can be seen that a too high Cu flux leads to a d/3 reconstruction in [110] (Figure 5.9 **a**) and a semicircle in [1$\bar{1}$0] direction (Figure 5.9 **b**). If the Cu flux is too low, a 2 × 2 reconstruction is observed along the [110] and [1$\bar{1}$0] crystal directions (Figure 5.9 **c** and **d**), which is easily confused with the surface reconstruction in stoichiometric growth. However, the significant difference to the 2 × 2 reconstruction of stoichiometric CuMnSb is the distinct modulation of the
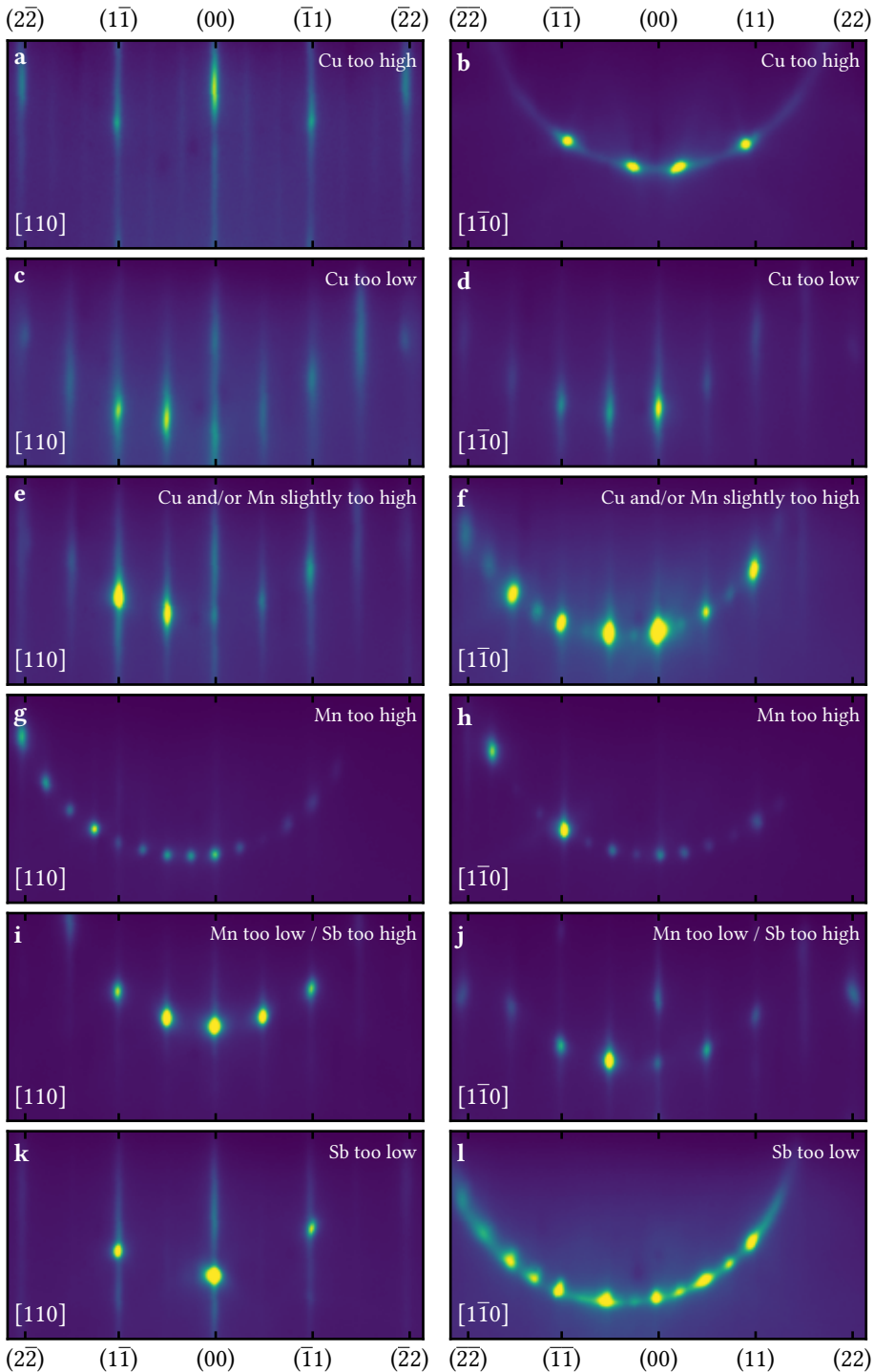
Figure 5.9: **Characteristic RHEED reconstructions for CuMnSb growth on InAs with growth parameters deviating from the stoichiometric case.**

streaks, which indicates a multilevel stepped surface [94]. The 2 × 4 reconstruction presented in Figure 5.9 **e** and **f** hints towards a slightly increased Cu and/or Mn flux. On the other hand, if the Mn flux is significantly too high and the fluxes of Cu and Sb are set correctly, the 4 × 4 reconstruction shown in Figure 5.9 **g** and **h** can be observed. Another 2 × 2 reconstruction is observed when either the Mn flux is set too low or the Sb flux is set too high (Figure 5.9 **i** and **j**). Compared to the stoichiometric case and the case with too little Cu flux, superimposed 3D transmission dots in the $[1\bar{1}0]$ direction are characteristic in this case. For a too low Sb flux, a d/1 reconstruction in [110] direction (Figure 5.9 **k**) and a semicircle in $[1\bar{1}0]$ direction (Figure 5.9 **l**) can be observed.

Initially, it is recommended to adjust the cell temperatures until the BEPs from Table 4.1 in subsection 4.3.2 are reached and grow a first sample using these conditions. Based on the observed RHEED reconstructions, cell temperatures should be changed (from sample to sample) until a known RHEED pattern is obtained. Here, the cell temperatures should be adjusted in 2 K steps for the Cu and Mn cells and in 0.4 K steps for the Sb cell. Once a known RHEED reconstruction is observed, cell temperatures can be further optimized until the 2 × 2 surface reconstruction of stoichiometric CuMnSb is achieved. For this procedure, the step size should be reduced to 1 K for Cu and Mn, and 0.2 K for Sb. Finally, the remaining physical parameters must be analyzed in order to verify that the sample is stoichiometric. For this purpose, the magnetic (T_{N}, μ_{eff} and Θ_{CW}) and electrical properties (T_{N} and ρ_0), as well as RBS measurements are particularly suitable.

5.2 Physical properties of epitaxial CuMnSb grown on GaSb (001)

This section is largely based on *L. Scheffler et al., Bulk-like magnetic properties in MBE-grown unstrained, antiferromagnetic CuMnSb, Appl. Phys. Lett.* **121**, *012401 (2022)* [95].

The characterization of epitaxial CuMnSb grown on GaSb is partially based on a series of nine samples, which differ in the flux ratio of Mn and Sb used. All nine samples were grown with identical Cu flux. An overview of the samples with the BEPs used and the resulting relative flux ratios $\Phi_{\mathrm{Mn}}/\Phi_{\mathrm{Sb}}$ of Mn and Sb is given in Table 5.1. Thereby $\Phi_{\mathrm{Mn}}/\Phi_{\mathrm{Sb}}$ is calculated per [96] by:

$$\frac{\Phi_{\mathrm{Mn}}}{\Phi_{\mathrm{Sb}}} = \frac{\mathrm{BEP}_{\mathrm{Mn}}}{\mathrm{BEP}_{\mathrm{Sb}}} \cdot \frac{\eta_{\mathrm{Sb}}}{\eta_{\mathrm{Mn}}} \cdot \sqrt{\frac{T_{\mathrm{Mn}}\mu_{\mathrm{Sb}}}{T_{\mathrm{Sb}}\mu_{\mathrm{Mn}}}}, \tag{5.5}$$

where η is the ionization efficiency, T is the effusion cell temperature, and μ is the atomic mass of the corresponding element. Since only effusion cells are used,

Sample	BEP_{Cu} $(10^{-9}$ mbar)	BEP_{Mn} $(10^{-9}$ mbar)	BEP_{Sb} $(10^{-8}$ mbar)	Φ_{Mn}/Φ_{Sb}	t_{CuMnSb} (nm)
1 H1274	5.80 ± 0.05	8.65 ± 0.05	4.23 ± 0.05	1.19 ± 0.02	39
2 H1273	5.80 ± 0.05	8.65 ± 0.05	4.10 ± 0.05	1.23 ± 0.02	37
3 H1271	5.80 ± 0.05	9.03 ± 0.05	4.23 ± 0.05	1.24 ± 0.02	40
4 H1272	5.80 ± 0.05	8.65 ± 0.05	4.00 ± 0.05	1.26 ± 0.02	39
5 H1269	5.80 ± 0.05	9.03 ± 0.05	4.10 ± 0.05	1.28 ± 0.02	40
6 H1270	5.80 ± 0.05	9.03 ± 0.05	4.00 ± 0.05	1.32 ± 0.02	39
7 H1277	5.80 ± 0.05	9.61 ± 0.05	4.23 ± 0.05	1.33 ± 0.02	41
8 H1276	5.80 ± 0.05	9.61 ± 0.05	4.10 ± 0.05	1.37 ± 0.02	40
9 H1275	5.80 ± 0.05	9.61 ± 0.05	4.00 ± 0.05	1.40 ± 0.02	39

Table 5.1: **Overview of the set of samples used for characterization of epitaxial CuMnSb grown on GaSb.**

it is understood that Mn is evaporated as single atoms and Sb as Sb_4 molecules. Since the growth time for the samples does not differ, the different material fluxes result in different CuMnSb layer thicknesses. However, it can be assumed that differences of a few nm have no influence on the investigated material properties. In the following, the measurements shown are assigned to the samples either by the sample number or by the used Φ_{Mn}/Φ_{Sb}.

5.2.1 Structural properties

Layer properties

All nine samples are characterized by $\omega - 2\theta$-diffractograms of the symmetric (002) diffraction peak using HRXRD. The lattice parameters are extracted using full dynamical simulations. Figures 5.10 **a-c** show the $\omega - 2\theta$-diffractograms for three characteristic samples that represent the three different types of observed strain (Samples 1, 5 and 9), together with the full dynamical simulations. The horizontal lattice parameter for all nine samples is found to be $a^{\parallel}_{CuMnSb} = a_{GaSb} = 6.096$ Å. In contrast to the growth on InAs, a clear dependence of the vertical lattice parameter on the material composition is observed. For instance, the lowest Mn/Sb flux ratio (Φ_{Mn}/Φ_{Sb}=1.19 ± 0.02, Figure 5.10 **a**) leads to a tensile strained CuMnSb crystal with a vertical lattice parameter of $a^{\perp}_{CuMnSb} = 6.092$ Å. An unstrained CuMnSb crystal ($a^{\parallel}_{CuMnSb} = a^{\perp}_{CuMnSb} = a_{GaSb} = 6.096$ Å) is formed at Φ_{Mn}/Φ_{Sb}=1.28 ± 0.02, as can be seen in Figure 5.10 **b**. A vertical lattice parameter of $a^{\perp}_{CuMnSb} = 6.111$ Å and thus a compressive strained CuMnSb crystal is found for the sample with the highest Φ_{Mn}/Φ_{Sb} of 1.40 ± 0.02.

The vertical lattice parameters of all nine samples are shown in Figure 5.10 **d**
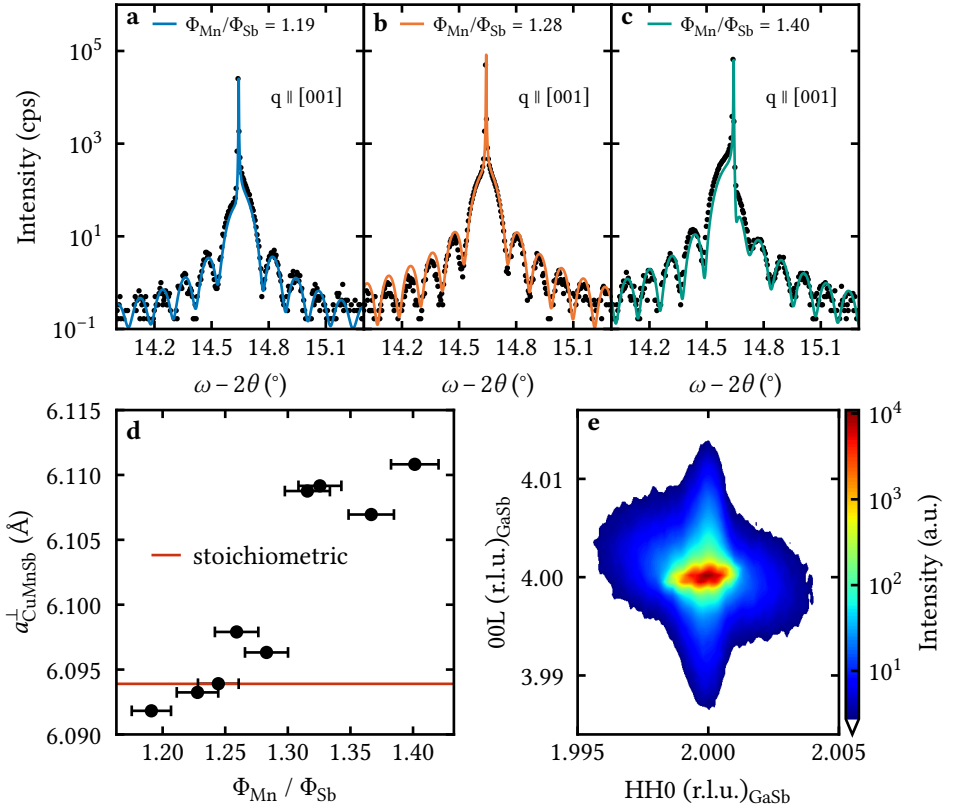
Figure 5.10: **HRXRD investigations of epitaxial CuMnSb grown on GaSb. a** $\omega - 2\theta$-diffractogram of the (002) diffraction peak with the corresponding full dynamical simulation of a sample grown with Φ_{Mn}/Φ_{Sb}=1.19 ± 0.02, revealing tensile strain of the CuMnSb crystal. **b** $\omega - 2\theta$-diffractogram of the (002) diffraction peak with the corresponding full dynamical simulation of a sample grown with Φ_{Mn}/Φ_{Sb}=1.28 ± 0.02. The measurement indicates that the CuMnSb crystal is unstrained. **c** $\omega - 2\theta$-diffractogram of the (002) diffraction peak with the corresponding full dynamical simulation of a sample grown with Φ_{Mn}/Φ_{Sb}=1.40 ± 0.02, revealing compressive strain of the CuMnSb crystal. **d** Vertical lattice parameters of all nine samples as a function of the relative Mn/Sb flux ratio. The calculated vertical lattice parameter for stoichiometric conditions is marked by the red line. **e** RSM of the asymmetric (224) diffraction peak of the stoichiometric sample.

as a function of the relative Mn/Sb flux ratio. There is a clear trend of increasing vertical lattice parameter with rising Φ_{Mn}/Φ_{Sb}. Similar behavior was also found for epitaxial NiMnSb [20, 97–99]. There it was suggested that defects like Mn_{Ni} (Mn substituting Ni) and Mn interstitials (Mn_{vac}) are responsible for the increase of $a^{\perp}_{NiMnSb}$ in NiMnSb. In CuMnSb Mn_{Cu}, Cu_{Mn} and Mn_{vac} are the defects with the

lowest formation energy [36]. It is therefore very likely that the observed variation of $a^\perp_{CuMnSb}$ is driven by the variation of the Mn content.

Based on the vertical lattice parameter calculated for CuMnSb grown on GaSb (see section 3.3), it is possible to estimate which of the samples most closely matches the stoichiometric conditions. The calculation yields $a^\perp_{stoi}$ = 6.094 Å for stoichiometric conditions. This value is marked by the red line in Figure 5.10 **d**. It is found that the vertical lattice parameter of sample 3 ($a^\perp_{CuMnSb}$ = 6.0939 Å), which was grown with a relative flux ratio of Φ_{Mn}/Φ_{Sb} = 1.24 ± 0.02, is closest to $a^\perp_{stoi}$. Sample 3 will therefore also be referred to as the stoichiometric sample in the following.

Figure 5.10 **e** shows the RSM of the asymmetric (224) diffraction peak of the stoichiometric sample. The peaks of GaSb and CuMnSb are superimposed, which is why investigations of the crystal quality of the CuMnSb layer by rocking curves are prevented. No signs of relaxation are observed, confirming the pseudomorphic character of the CuMnSb film.

SURFACE PROPERTIES

The surface of the CuMnSb films grown on GaSb is investigated by RHEED and AFM. Figure 5.11 shows the surface reconstructions along the [100], [010], [110] and [1$\bar{1}$0] crystal directions of the stoichiometric sample after growth. As for the growth on InAs, a 2 × 2 reconstruction is observed along the [100] (Figure 5.11 **a**) and [010] (Figure 5.11 **c**) crystal directions. Right after growth starts, the CuMnSb surface also exhibits a 2 × 2 reconstruction in the [110] and [1$\bar{1}$0] crystal directions. For the stoichiometric sample, this 2 × 2 reconstruction transforms into a 2 × 4 reconstruction after 10 min of growth and remains unchanged until growth is terminated. The 2 × 4 reconstruction at the end of growth is shown in Figures 5.11 **b** and **d**.

Sample	Φ_{Mn}/Φ_{Sb}	surface reconstruction	RMS roughness (nm)
1	1.19 ± 0.02	2 × 2	0.96
2	1.23 ± 0.02	2 × 4	0.26
3	1.24 ± 0.02	2 × 4	0.20
4	1.26 ± 0.02	1 × 4	0.18
5	1.28 ± 0.02	2 × 6	0.14
6	1.32 ± 0.02	1 × 1	0.33
7	1.33 ± 0.02	1 × 1	0.15
8	1.37 ± 0.02	3 × 2	0.20
9	1.40 ± 0.02	5 × 1	0.16

Table 5.2: **Surface properties of the set of samples used for characterization of epitaxial CuMnSb grown on GaSb.**
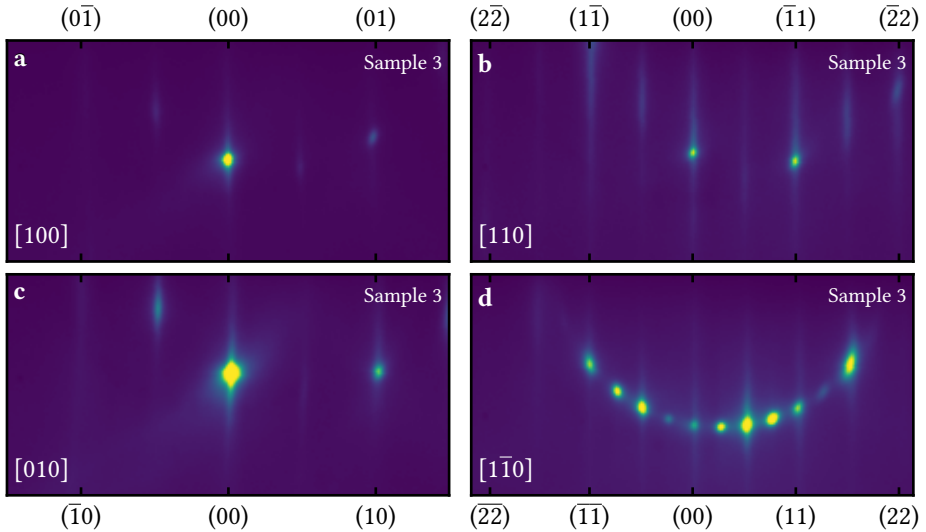
Figure 5.11: **RHEED reconstructions of the CuMnSb surface grown on GaSb under stoichiometric conditions. a** d/2 reconstruction along the [100] crystal direction. **b** d/2 reconstruction along the [110] crystal direction. **c** d/2 reconstruction along the [010] crystal direction. **d** d/4 reconstruction along the [1$\bar{1}$0] crystal direction.

In Table 5.2, the observed surface reconstructions along the [110] and [1$\bar{1}$0] crystal directions for all nine samples are given. The surface reconstruction is highly sensitive to material composition; samples grown with similar Φ_{Mn}/Φ_{Sb} [$\Delta(\Phi_{Mn}/\Phi_{Sb}) \leq 0.01$] exhibit the same surface reconstruction. Thus, the RHEED reconstructions can also be used to tune the growth parameters in the case of CuMnSb growth on GaSb.

In addition, Table 5.2 lists the RMS roughness values of the nine samples determined by AFM. Except for the sample with the lowest relative Mn/Sb flux ratio, all samples have comparable surface roughness. The lowest RMS roughness is found for the lattice-matched CuMnSb layer (Sample 5). However, more significant differences are found in the surface morphology, which is shown exemplarily for two of the samples in Figure 5.12. The surface of the stoichiometric sample shows stripes that are oriented along the [110] crystal direction, as can be seen in Figure 5.12 **a**. From the extracted line profile (Figure 5.12 **b**) heights of the stripes from 3 to 10 Å can be detected. These stripes are strongly reminiscent of an AFM-typical artifact, which can be caused by the so-called piezo drift. Measurements on the same sample in the work of Jonas Knobel [41, Fig. 4.6 f)] show these stripes as well, which weakens the suspicion of an instrumental artifact.

In contrast, the surface of the unstrained CuMnSb layer (Figure 5.12 **c**) shows
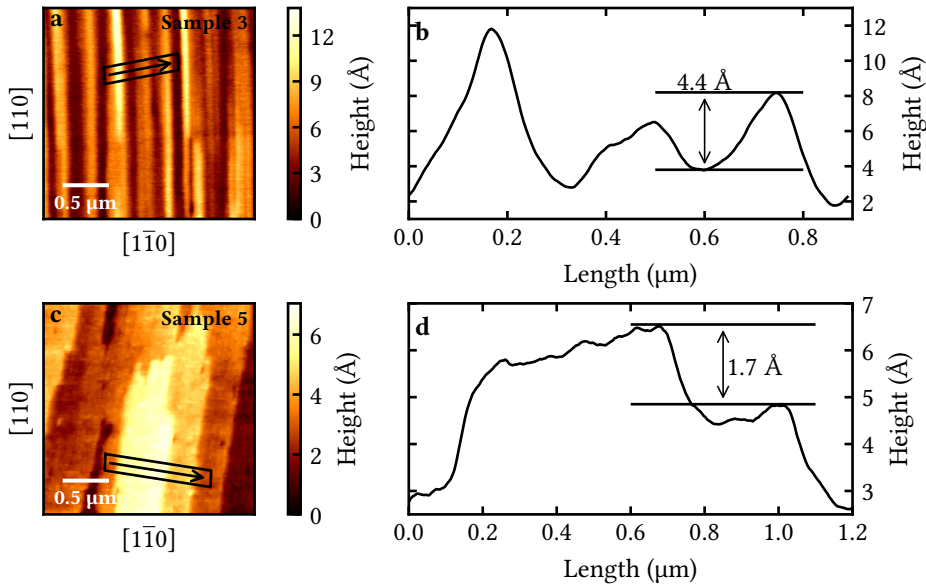
Figure 5.12: **AFM investigations of the Ru capped CuMnSb surface for samples grown on GaSb.** **a** AFM image of the stoichiometric CuMnSb sample. **b** Line profile extracted from the highlighted area in **a**. **c** AFM image of the unstrained CuMnSb sample. **d** Line profile extracted from the highlighted area in **c**.

atomic steps. According to the extracted line profile in Figure 5.12 **d**, the steps have a minimum height of one-quarter lattice parameter, corresponding to a single atomic layer (either an MnSb or a Cu layer). This is noteworthy in that both the InAs and GaSb substrates and the CuMnSb layers grown on InAs feature atomic steps with a minimum height of half a lattice parameter. Whether the stability of individual atomic layers is enhanced by the absence of strain cannot be conclusively determined. However, it can be concluded that the unstrained growth leads to the best surface quality of the CuMnSb layer.

5.2.2 Electrical properties

The electrical characterization is performed on Hall bars with a size of $180 \times 1080 \, \mu m^2$, which are fabricated by standard optical lithography. Argon dry etching followed by a wet etch step in a phosphorus-citric acid based solution is used to define the mesa. More details about the manufacturing process, as well as further in-depth electrical measurements, can be found in [68]. Again, parasitic conductivities due to the Ru protective layer and substrate are accounted for using a reference sample (see subsection 5.1.2 for details).

Figure 5.13 **a** shows the temperature dependent resistivity of the stoichiometric
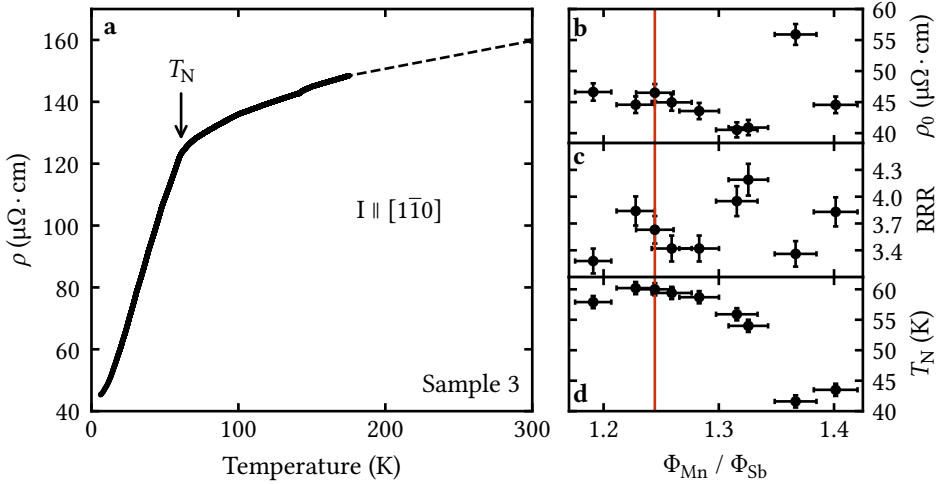
Figure 5.13: **Electrical characterization of epitaxial CuMnSb grown on GaSb. a** Temperature dependent resistivity of the stoichiometric CuMnSb sample grown on GaSb. The magnetic phase transition is indicated by a clear kink. **b**-**d** Residual resistivity, residual resistivity ratio, and Néel temperature of all nine samples as a function of the relative Mn/Sb flux ratio. The red line marks the stoichiometric composition.

sample. The magnetic phase transition is marked by a clear kink at around $T_N = 60\,\mathrm{K}$. The overall trend is comparable to the temperature dependent resistivity of CuMnSb grown on InAs. A slightly higher ρ_0 of $46\,\mu\Omega \cdot$ cm indicates a marginally degraded crystal quality. Except for the sample with Φ_{Mn}/Φ_{Sb}=1.37 ± 0.02, comparable values of ρ_0 are measured, as can be seen in Figure 5.13 **b**.

For other (half-) Heusler materials, a relation between the defect density and the residual resistivity ratio (RRR) was found [100, 101], leading to lower RRR values for higher defect concentrations. No such dependency is observed in the samples studied here. As can be seen in Figure 5.13 **c**, there is no trend of RRR as a function of Φ_{Mn}/Φ_{Sb}. However, there is a clear trend as a function of Φ_{Mn}/Φ_{Sb} for T_N, according to Figure 5.13 **d**. Around the stoichiometric composition (marked by the red line) the highest values of T_N are measured. When leaving the stoichiometric composition, a decrease of T_N is observed. Similar behavior was also observed for Co substitution in CuMnSb [27]. The two samples with the highest Φ_{Mn}/Φ_{Sb} and smallest T_N both indicated spontaneous magnetization already at room temperature. Ferromagnetic inclusions due to the high Mn concentration are the most likely explanation for this observation.

Ferromagnetic inclusions (in particular an Mn_2Sb impurity phase) were also observed in CuMnSb grown by means of optical float-zoning [26], when the CuMnSb was prepared from stoichiometric initial weight. The formation of this phase was

prevented by a slight Sb excess in the initial weight. For the resulting sample, RRR and T_N were reported to be 4.2 and 55 K, respectively. In this work, comparable values are measured for the epitaxial CuMnSb around Φ_{Mn}/Φ_{Sb}=1.33 ± 0.02, which is still too high a Mn concentration with respect to the stoichiometric composition.

5.2.3 Magnetic properties

The low lattice mismatch between CuMnSb and GaSb allows the growth of CuMnSb layers with unlimited thickness. For the magnetic characterization, stoichiometric CuMnSb layers with different thicknesses t were prepared to investigate the influence of the layer thickness on the magnetic properties. Their thickness ranges from 5 to 510 nm. The basic magnetic properties are discussed on the basis of the thickest CuMnSb layer (t = 510 nm), since the magnetic signal of this sample is the strongest. All measurements are compensated using the COMP method described in section 3.4.

First, the temperature dependence of the magnetization $M(T)$ is investigated. Figure 5.14 **a** shows the FC curves of $M(T)$ acquired in magnetic fields between 1 and 7 T along the $[1\bar{1}0]$ crystal direction. In all measurements, the characteristic cusp indicates the magnetic phase transition. It occurs independently of the magnetic field at the identical temperature. T_N can therefore be determined to 62 K, which corresponds to the highest value reported for bulk CuMnSb [27]. Qualitatively, the measurements are in agreement with those published for bulk material [26]. However, there are also significant differences to be noted. Compared to the bulk material, the values measured for magnetization are about 44 % larger. Furthermore, the $M(T)$ curves show no signs of canting of the Mn spins from the $\langle 111 \rangle$ direction below T_N. This raises the question of whether these experimental differences reveal a discrepancy that exists between stoichiometric and point-defect-affected material. To answer this question, experiments are needed that can determine the exact orientation of the local magnetic moments (e.g. neutron diffraction) and not just the projection of the external magnetic moment of the sample onto the measurement direction as SQUID magnetometry does.

To investigate a possible directional dependence of $M(T)$, further FC curves are measured at $\mu_0 H$ = 1 T along the [100] and [110] crystal directions. They are plotted together with $M(T)$ and the temperature dependent inverse susceptibility $\chi^{-1}(T)$ along the $[1\bar{1}0]$ crystal direction in Figure 5.14 **b**. In the paramagnetic state, isotropic behavior of $M(T)$ is observed above a temperature of 100 K. Below 100 K, a weak anisotropy can be identified similar to what is reported for bulk CuMnSb [26]. In particular, for both the bulk material and the epitaxial CuMnSb, the [100] direction is the magnetically softest and the [110] direction is the magnetically hardest.

In contrast to the CuMnSb layer grown on InAs, which was characterized
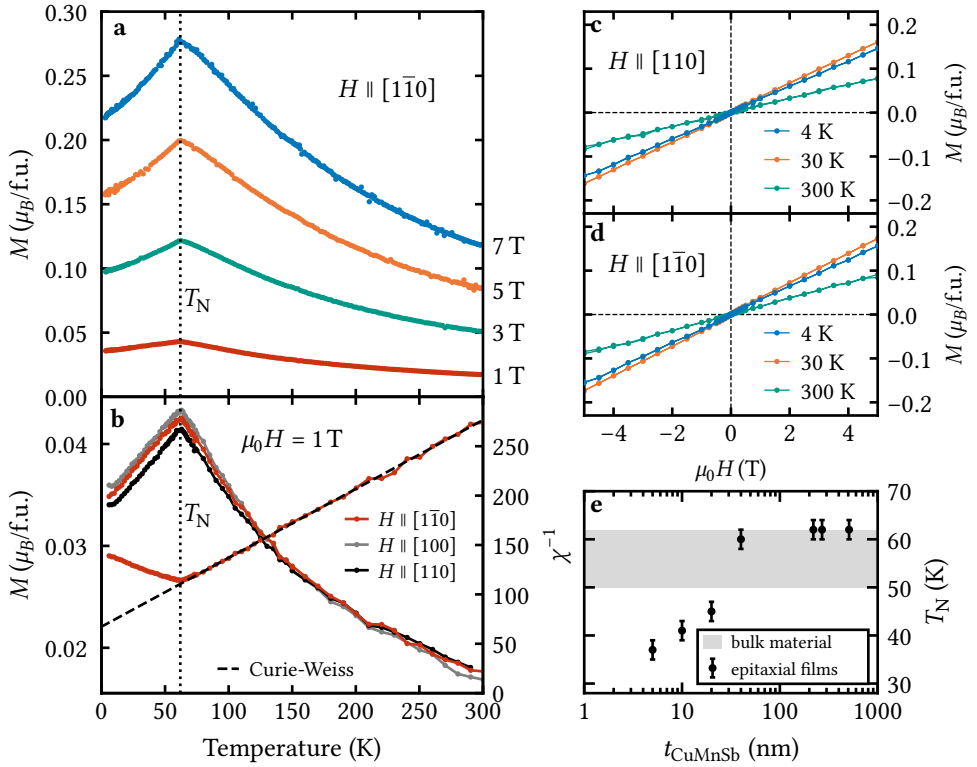
Figure 5.14: **Magnetic characterization of epitaxial CuMnSb grown on GaSb.** 🔖 H1265
The measurements are compensated using the COMP method described in section 3.4. **a**
FC curves of the magnetization $M(T)$ acquired at various magnetic fields along the $[1\bar{1}0]$
crystal direction of a 510 nm thick CuMnSb layer. T_N is marked by a dotted line. **b** $M(T)$
during cooldown of the same sample at a bias field of 1 T along the $[1\bar{1}0]$, $[100]$ and $[110]$
crystal directions (left axis) together with the temperature dependent inverse susceptibility
$\chi^{-1}(T)$ along the $[1\bar{1}0]$ crystal direction (right axis). The dashed line represents the Curie-
Weiss fit. **c** Magnetic field dependent magnetization $M(H)$ along the $[110]$ crystal direction
at various temperatures. **d** Magnetic field dependent magnetization $M(H)$ along the $[1\bar{1}0]$
crystal direction at various temperatures. **e** T_N as a function of the CuMnSb layer thickness.
The gray area marks the range of values reported for bulk CuMnSb in the literature.

magnetically in subsection 5.1.3, $\chi^{-1}(T)$ of the sample investigated here follows
a perfectly straight line in the paramagnetic phase. However, this is not due to
the different substrate, but rather to the much greater thickness of the CuMnSb
layer, which will be discussed in detail in section 6.1. Θ_{CW} and μ_{eff} are extracted
using a fit according to the Curie-Weiss law. The fit yields $\Theta_{CW} = -100$ K and
$\mu_{eff} = 5.6$ μ_B/f.u.. Compared to CuMnSb grown on InAs, Θ_{CW} is reduced by 35 K,

which is probably due to the lower strain and the resulting increased geometric frustration in the antiferromagnetic state. μ_{eff} is also slightly reduced, but is still above the theoretical expected value of 4.9 μ_{B}/f.u. [88], which is a sign for itinerant magnetism [89].

The magnetic field dependence of the magnetization $M(H)$ is investigated along the [110] (Figure 5.14 **c**) and [1$\bar{1}$0] (Figure 5.14 **d**) crystal directions. Within the measured field range of ±5 T, $M(H)$ shows a linear field dependence in both the paramagnetic and antiferromagnetic phases. Neither saturation of the magnetization nor hysteretic behavior is observed. The former fits the findings of bulk material [93] and of CuMnSb grown on InAs. The latter, however, contradicts the results of CuMnSb grown on InAs. As shown in section 6.1, the significantly increased thickness of the CuMnSb layer studied here compared to the layer grown on InAs is again responsible for this finding.

Using temperature dependent measurements of the magnetization as shown in Figure 5.14 **a**, T_{N} was determined for epitaxial CuMnSb films of different thicknesses. The measured values of T_{N} are plotted as a function of the CuMnSb thickness in Figure 5.14 **e**. The gray area marks the range of values reported previously for bulk material [21, 23–27]. A T_{N} of 62 K is found for layers with a thickness greater than 200 nm. The sample with a CuMnSb thickness of 40 nm already exhibits a slightly reduced T_{N} of 60 K. A further reduction of the layer thickness leads to a further decrease of T_{N} down to 37 K for the 5 nm thick sample. The significant decrease of T_{N} towards very thin films indicates a possible difference in the surface and volume contributions to the antiferromagnetic order.

5.2.4 Achieving stoichiometry

Similar to the growth of CuMnSb on InAs, the adjustment of growth parameters for CuMnSb growth on GaSb is an iterative process. A major advantage, however, is the dependence of the vertical lattice parameter on the material composition presented in subsection 5.2.1. In addition, the Néel temperature can be a useful tool to determine the stoichiometry of a sample.

It is again recommended that the values presented in Table 4.1 in subsection 4.3.2 for the material fluxes are set initially. The BEPs then should be adjusted until a known surface reconstruction is observed in RHEED. Steps of 2 K for the Mn cell temperature and 0.4 K for the Sb cell temperature have been found to be suitable for this process. The Cu cell temperature, on the other hand, should be kept constant, since even the smallest changes in material flux that are below the resolution limit of the flux gauge can have a significant effect on the material parameters. If a first sample with known surface reconstruction is grown, another sample with deviating Mn concentration should be grown next to check if the expected change of the vertical lattice parameter can be observed by HRXRD. If this is the case, further

optimization of the material fluxes can be performed until the stoichiometric vertical lattice parameter of $a_{\mathrm{stoi}}^{\perp} = 6.094\,\text{Å}$, and the described 2 × 4 surface reconstruction is achieved. For this purpose, the cell temperatures of the Mn and Sb cells should be adjusted in 1 K and 0.2 K steps.

The optimization process should be accompanied by measurements of T_{N}, which should be maximum for stoichiometric conditions. Another quality feature of the perfect growth conditions is a stable 2 × 4 surface reconstruction even during the growth of very thick CuMnSb layers over several hours.

5

6

Magnetism of epitaxial CuMnSb

In this chapter, the magnetic properties of epitaxial CuMnSb are discussed in more depth. Particular focus is placed on differences from the bulk material and on phenomena that have not yet been described in the literature. First, the magnetic behavior in weak magnetic fields is analyzed. In this context, both the hysteretic behavior, which is atypical for an antiferromagnet, and the temperature dependence of the magnetization are examined in more detail. This is followed by the presentation of evidence for spin-glass-like behavior at low temperatures and the investigation of the exchange bias effect by testing various ferromagnets that are sputtered onto the CuMnSb surface. Finally, first results from a muon spin rotation experiment performed on epitaxial CuMnSb are presented.

6.1 Nonlinear behavior of the field dependent magnetization

Before presenting the field dependent magnetization $M(H)$ of epitaxial CuMnSb, $M(H)$ of an idealized antiferromagnet is briefly explained with the help of Figure 6.1. Thereby two cases are considered: $M(H)$ at $T = 0\,\text{K}$, which is shown in Figure 6.1 **a**, and $M(H)$ at $T > 0\,\text{K}$, which is shown in Figure 6.1 **b**. For an ideal antiferromagnet with perfectly compensated moments, one expects a net moment of 0 when no external magnetic field is applied. By applying an external magnetic field, the magnetic moments of the antiferromagnet will be slightly tilted towards the direction of the external field, regardless of the direction at temperatures above $0\,\text{K}$, as it is shown in Figure 6.1 **b**. Thereby, the net moment increases linearly with the strength of the external magnetic field until all moments are aligned along the magnetic field and saturation (M_{sat}) is reached. The increase in net magnetization is strongest when the external field is applied along a magnetically hard axis ($H_\perp$) and weakest when the field is applied along a magnetically easy axis ($H_\parallel$). At $T = 0\,\text{K}$
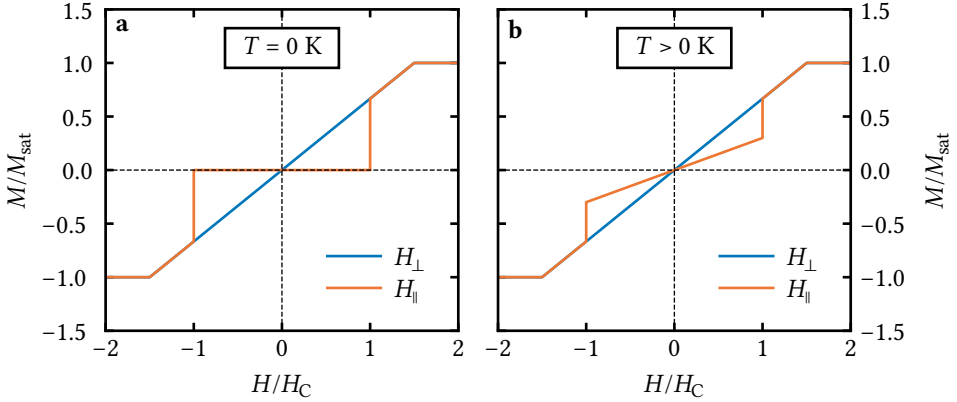
Figure 6.1: **Magnetic field dependent magnetization $M(H)$ of an idealized antiferro-magnet with perfectly compensated moments.** $M(H)$ is shown for the field applied along the magnetic easy axis ($H_\parallel$) and along the magnetic hard axis ($H_\perp$) for $T = 0\,\text{K}$ (**a**) and $T > 0\,\text{K}$ (**b**).

(Figure 6.1 **a**), the magnetic moments do not tilt when the field is applied along the magnetic easy axis because no net force of the applied field can act on the moments in this configuration. This is due to the fact that there are no temperature fluctuations of the magnetic moments at a temperature of $0\,\text{K}$. To minimize energy, it is possible for the magnetic moments to flip to a magnetically hard axis when a field that exceeds a critical field strength (H_C) is applied along the easy axis through what is known as a spin-flop transition. Such a transition is manifested by a sudden increase in magnetization towards the curve for a field applied along the hard axis, as shown for both cases in Figure 6.1.

As mentioned earlier, no saturation was observed for bulk CuMnSb at fields up to $50\,\text{T}$ [93]. Furthermore, no evidence of a spin-flop transition in CuMnSb has been reported so far. Transferred to the experimental methods available for this work (fields up to $7\,\text{T}$), it can therefore be expected that the magnetization is exclusively linear and non-saturating as a function of the magnetic field. As reported in subsection 5.1.3 (Figure 5.8), the $40\,\text{nm}$ thick stoichiometric CuMnSb layer grown on InAs and capped with Ru exhibits a nonlinear dependence on the magnetic field in the antiferromagnetic state for weak magnetic fields. At very low temperatures, even an open hysteresis can be observed. In comparison, the $510\,\text{nm}$ thick CuMnSb layer grown on GaSb, which was investigated in subsection 5.2.3 (Figure 5.14), shows a linear, non-saturating behavior at first glance.

Figures 6.2 **a** and **b** resume the measurements at $30\,\text{K}$ and $4\,\text{K}$ of the sample grown on GaSb, supplemented by measurements with the field along the [001] crystal direction. In order to examine the measurements for a nonlinear component,
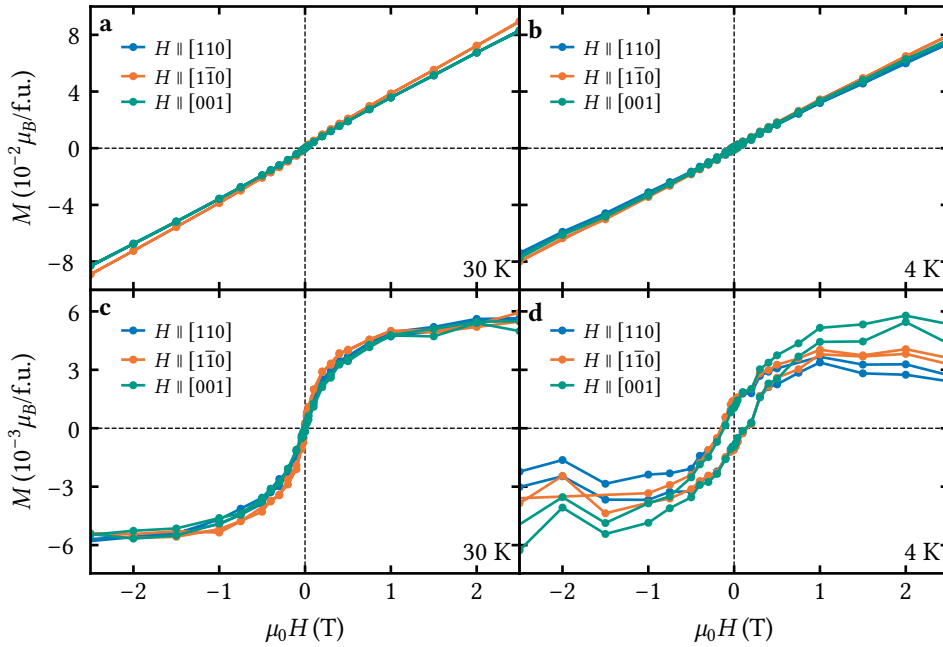
Figure 6.2: **Nonlinearity of the magnetic field dependent magnetization $M(H)$ along the [110], [1$\bar{1}$0] and [001] crystal directions of epitaxial CuMnSb grown on GaSb.** 🗏 H1265 The measurements are compensated using the COMP method described in section 3.4. **a** $M(H)$ at 30 K. **b** $M(H)$ at 4 K. **c** $M(H)$ after subtraction of the linear component at 30 K. **d** $M(H)$ after subtraction of the linear component at 4 K.

the linear component determined at high fields is subtracted from the measurements. The resulting curves are shown in Figures 6.2 **c** and **d**. A saturating nonlinear component is revealed for both temperatures. While the curve at 30 K shows superparamagnetic character, an open hysteresis develops at 4 K, as was found for the sample grown on InAs. For both temperatures, the curves are fairly isotropic. Although an open hysteresis is not expected for an ideal antiferromagnet, there are some effects that may cause net magnetic moments in real antiferromagnets, which are listed below:

a) ferromagnetic inclusions

b) spin-canting due to Dzyaloshinskii–Moriya interaction [102, 103]

c) antiferromagnetic domain walls [104]

d) uncompensated moments in the bulk crystal

e) uncompensated surface spins [105]
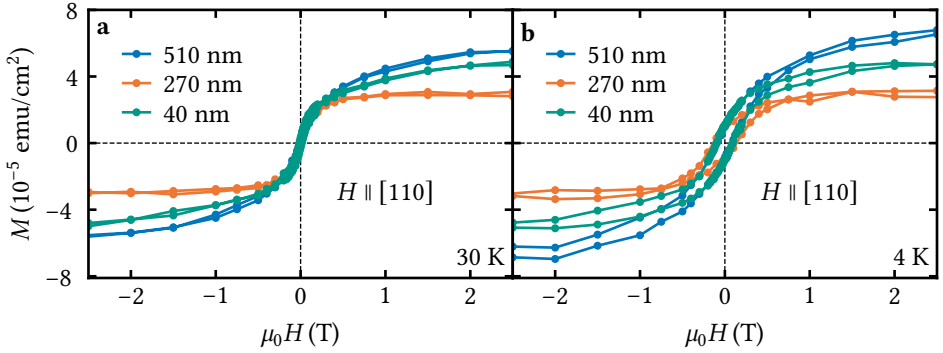
Figure 6.3: **Nonlinear component of the field dependent magnetization** $M(H)$ **of three CuMnSb layers with different thicknesses.** 🗇H1265 🗇H1232 🗇H1271 The measurements are compensated using the COMP method described in section 3.4. The linear component determined at high fields is subtracted from the original measurements. **a** $M(H)$ at 30 K. **b** $M(H)$ at 4 K.

The mechanisms a)-d) are volume effects, so their signal strength should be volume dependent. In the case of b), it must be mentioned that the Dzyaloshinskii–Moriya interaction can also be an interface effect, but at this point, it is referred to the spin-canting in bulk antiferromagnets, which can lead to weak ferromagnetism as described in [102, 103]. On the other hand, the signal strength from uncompensated surface spins is expected to be area dependent.

In order to verify whether the nonlinear component of epitaxial CuMnSb is volume or area dependent, Figure 6.3 compares the nonlinear component normalized to the area of the sample for three CuMnSb layers of different thickness. For this purpose, the linear component determined at high fields was again subtracted from the measurements and the resulting values were divided by the sample area. For both the measurements at 30 K (Figure 6.3 **a**) and 4 K (Figure 6.3 **b**), the signals of the three samples are of comparable magnitude. In particular, no correlation with the layer thickness can be seen, which indicates an area effect. This also explains why the nonlinear signal is more prominent in measurements on thinner layers, such as the CuMnSb layer grown on InAs, which was investigated in subsection 5.1.3. Whether the signal originates from the CuMnSb surface, the CuMnSb/buffer interface, or both cannot be answered at this point. Since the signal occurs independently of the cap material used, the cap can be excluded as the source.

To further investigate the signal and especially its thickness and temperature dependence, an etching experiment is performed on a 270 nm thick CuMnSb layer, which was grown on GaSb. In this experiment, the CuMnSb layer thickness and

thus the CuMnSb volume of the Ru-capped sample is reduced stepwise by argon dry etching. After each etching step, the CuMnSb layer is capped again in-situ with 5 nm Ru by DC-magnetron sputtering. The resulting CuMnSb thicknesses determined by HRXRD are 270 nm, 190 nm, 130 nm, and 100 nm. Finally, the CuMnSb layer is removed completely to obtain a reference sample for the magnetic measurements. For each of these CuMnSb thicknesses, $M(H)$ is measured at various temperatures between 80 and 20 K along the [110] and [1$\bar{1}$0] crystal directions. The magnetization is compensated using the COMP method described in section 3.4. Subsequently, the linear part of the compensated magnetization determined by a linear fit at high fields is subtracted from the compensated measurement, thus obtaining the nonlinear part of the measurement.

The resulting nonlinear part of $M(H)$, normalized to the area of the sample, is shown in Figure 6.4. For the unetched sample (t_{CuMnSb} = 270 nm), a strong anisotropy of the nonlinear signal can be observed. At all measured temperatures, it is much more pronounced along the [1$\bar{1}$0] crystal direction. This anisotropy disappears after the first etching process (t_{CuMnSb} = 190 nm). The nonlinear signal is comparable for both crystal directions. The fact that the nonlinear signal can be affected by argon dry etching indicates that the origin of the signal is localized at the surface of the CuMnSb layer since the argon ions only penetrate the CuMnSb surface and do not affect the CuMnSb/buffer interface. For argon dry etching, an ion energy of 400 eV was used. At this energy, the surface of the crystal is typically damaged to depths in the single-digit nanometer range [106]. Furthermore, amorphization of the crystal on the surface is possible.

Comparing the measurements along the [1$\bar{1}$0] crystal direction for the different CuMnSb film thicknesses, it is observed that the saturation magnetization of the nonlinear signal is slightly increased after each etching step. More importantly, the signal does not scale with the decrease in CuMnSb volume. This result reinforces the hypothesis that the nonlinear signal is not a bulk effect, but a surface or interface effect. It is therefore very likely that the nonlinear signal is generated by uncompensated moments on the CuMnSb surface, as has been demonstrated for the antiferromagnetic transition-metal monoxide NiO [105]. Since CuMnSb and NiO share the same AFM111 antiferromagnetic structure, a comparable magnetic behavior at the surface is conceivable. Furthermore, a slight increase in the coercive field can also be noticed after each of the etching steps.

Both the disappearance of the anisotropy and the slight increase of the saturation magnetization of the nonlinear signal by the argon dry etching could be explained by damage to and consequent roughening of the CuMnSb surface by the argon ions. In the case of lost anisotropy, a change in surface morphology like amorphization of the crystal could cause existing preferred directions of magnetic moments at the surface to be eliminated. Increasing saturation magnetization
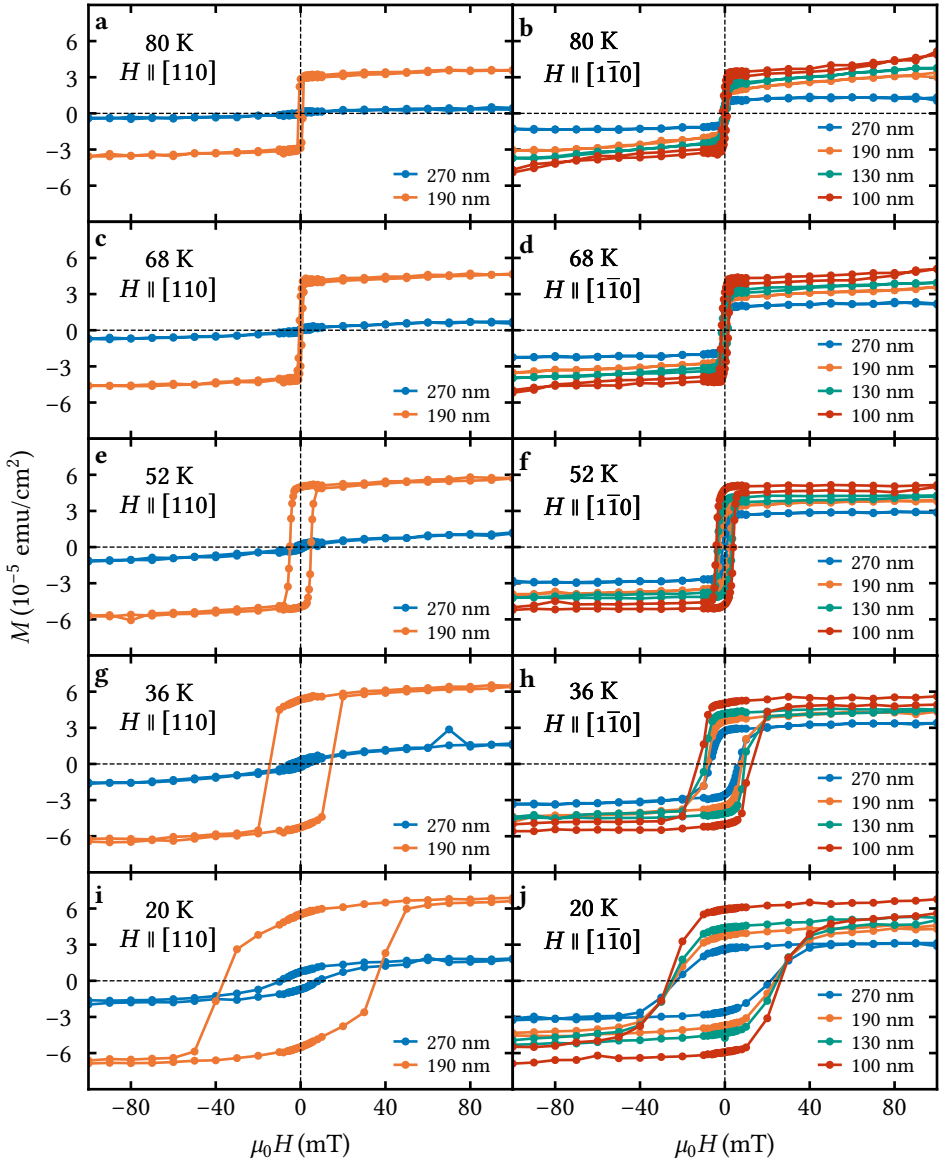
Figure 6.4: **Temperature and thickness development of the nonlinear component of the magnetic field dependent magnetization of epitaxial CuMnSb.** H1232 The CuMnSb thickness is reduced in steps by argon dry etching. The measurements are compensated using the COMP method described in section 3.4 and the linear component determined at high fields is subtracted from the original measurements.
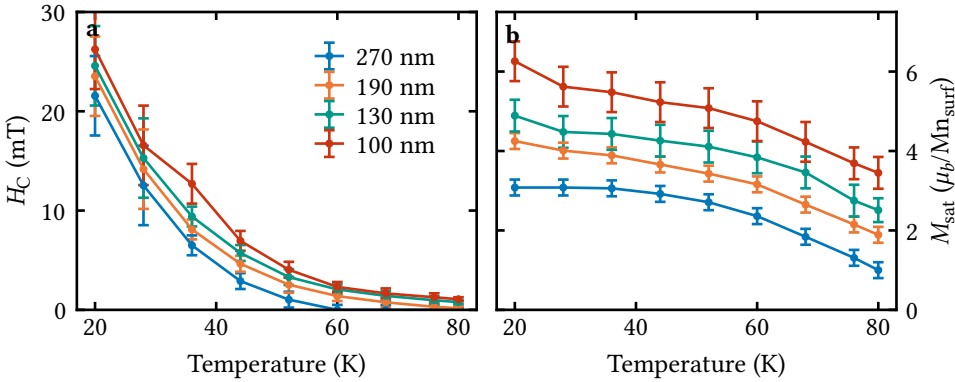
Figure 6.5: **Temperature dependence of the characteristic parameters of the non-linear component of the magnetic field dependent magnetization of epitaxial CuMnSb.** H1232 **a** Temperature dependence of the coercive field. The pronounced increase of the error bars of the coercive field towards lower temperatures is due to the lower density of measurement points of $M(H)$ at these values. **b** Temperature dependence of the saturation magnetization in units of Bohr magnetons per surface Mn atom, assuming that only one surface layer of CuMnSb with the height of one lattice parameter contributes to the nonlinear signal.

could be explained by an increase in the uncompensated surface moments due to roughening.

The characteristic parameters of the nonlinear signal along the $[1\bar{1}0]$ crystal direction, respectively the hysteresis at lower temperatures are shown in Figure 6.5 as a function of temperature. As can be seen from Figure 6.5 **a**, the coercive field decreases inversely proportional to the temperature. While a coercive field and thus an open hysteresis can be observed for the unetched sample ($t_{\text{CuMnSb}} = 270\,\text{nm}$) only below $T_{\text{N}} = 62\,\text{K}$, the etched samples already show a small coercive field above the magnetic transition. As already mentioned, each etching step increases the coercive field slightly. The temperature dependence of the saturation magnetization M_{sat} is plotted in Figure 6.5 **b**. Here, M_{sat} is converted to units of Bohr magnetons per surface Mn atom (Mn_{surf}) by assuming that only one surface layer of CuMnSb with the height of one lattice parameter contributes to the nonlinear signal. An increase in M_{sat} towards lower temperatures is clearly evident for all CuMnSb thicknesses. The individual etching steps also lead to an increase in M_{sat}. For the unetched sample, M_{sat} reaches a value of $3.1\,\mu_b/\text{Mn}_{\text{surf}}$ at 20 K, indicating that only part of the top CuMnSb layer provides uncompensated moments (assuming $\approx 4.7\,\mu_b/\text{Mn}$ as obtained from Curie-Weiss fits in subsection 5.2.3). In contrast, the sample with a CuMnSb thickness of 100 nm reaches values of $6.3\,\mu_b/\text{Mn}_{\text{surf}}$ for M_{sat}. Due to the surface damage caused by etching, several layers of CuMnSb might

therefore contribute to the nonlinear signal. Whether this is actually due to the damage to the uppermost CuMnSb layers or due to an increase in the surface area by roughening cannot be conclusively determined.

6.2 TEMPERATURE DEPENDENCE OF THE MAGNETIZATION IN WEAK MAGNETIC FIELDS

Investigations of bulk CuMnSb revealed an almost textbook-like temperature dependence of the magnetization [21, 23–26]. This is characterized by an increase in magnetization towards lower temperatures, following the Curie-Weiss law, until the phase transition from the paramagnetic to the antiferromagnetic state occurs. Below T_N, the magnetization drops as a function of decreasing temperature due to the increasing antiferromagnetic interaction and the reduction of thermal energy, forming the characteristic cusp at T_N. In the antiferromagnetic state, a weak anisotropy of the temperature dependent magnetization, as well as signatures of canting of the spins at low temperatures, was observed [26]. While the temperature at which spin-canting occurs is field dependent, the shape of the curve is not affected by the magnitude of the magnetic field. Solely the absolute value of the temperature dependent magnetization increases linearly by increasing the magnetic field up to 9 T.

Comparable behavior to bulk material was reported in subsection 5.2.3 for a 510 nm thick epitaxial CuMnSb layer grown on GaSb in magnetic fields larger than or equal to 1 T (see Figure 5.14). The only differences to the measurements of bulk CuMnSb are the absence of signs of spin canting and the absolute magnitude of the signal. In contrast, the temperature dependent magnetization $M(T)$ of the 40 nm thick CuMnSb layer grown on InAs, investigated in subsection 5.1.3, shows further discrepancies with the bulk material measurements at a magnetic field of 1 T (see Figure 5.8). In particular, the additional Curie-Weiss regime below 230 K with positive Θ_{CW} represents a significant difference, as this behavior was not yet reported for CuMnSb in literature. It will be part of this section to clarify whether this second Curie-Weiss regime is a universal property of epitaxial CuMnSb, or whether it only occurs in very thin films.

So far, no in-depth analysis of $M(T)$ of CuMnSb at weak magnetic fields has been published in the literature. However, the nonlinear behavior of $M(H)$ at low magnetic fields, which was attributed to uncompensated surface moments in section 6.1, suggests investigating also $M(T)$ more closely at low magnetic fields. For this purpose, field cooled warming (FCW) measurements of the 510 nm thick CuMnSb layer grown on GaSb, which behaves very similarly to the bulk material at higher fields, are performed at different magnetic fields. The main advantage of using this very thick layer (in the context of fabrication by MBE) is that even at
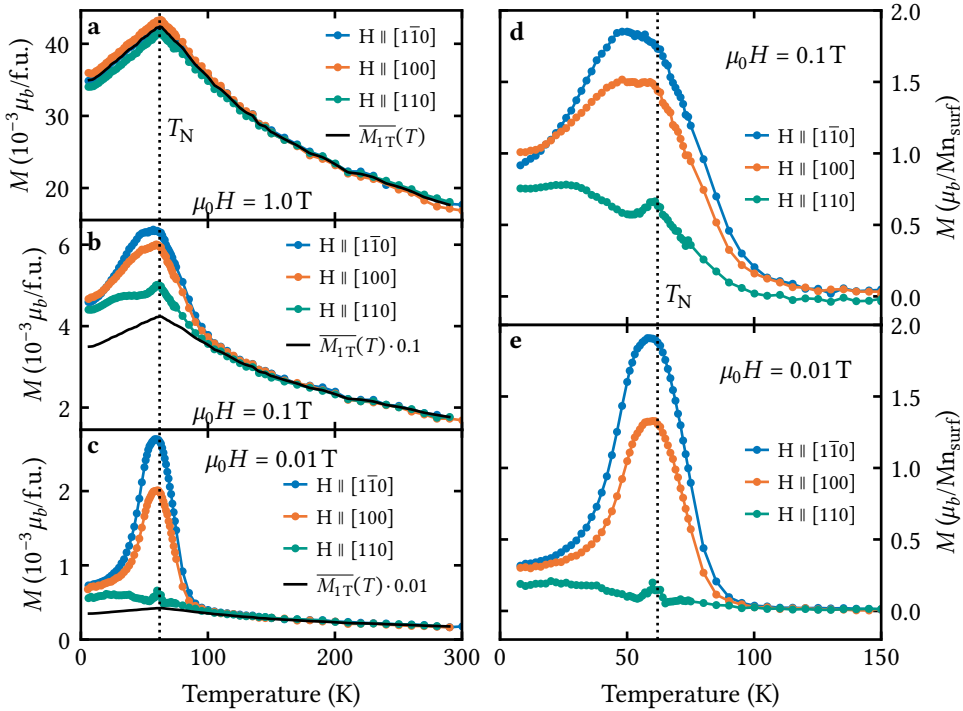
Figure 6.6: **Temperature dependent magnetization** $M(T)$ **of a 510 nm thick CuMnSb layer at weak magnetic fields.** 🍃 H1265 The measurements are compensated using the COMP method described in section 3.4. **a-c** $M(T)$ at magnetic fields of 1 T, 0.1 T and 0.01 T in the three crystal directions, [100], [110] and [1$\bar{1}$0]. The average $M(T)$ at 1 T ($\overline{M_{1T}}(T)$), which is scaled to the applied external magnetic field by assuming a linear dependence, is shown for comparison. **d**, **e** $M(T)$ at magnetic fields of 0.1 T and 0.01 T with the scaled $\overline{M_{1T}}(T)$ subtracted and converted into units of Bohr magnetons per surface Mn atom.

low magnetic fields, a sufficiently large magnetic signal can be measured with the SQUID magnetometer.

The analysis of $M(H)$ in Figure 6.6 begins by resuming the measurement at 1 T (Figure 6.6 **a**), which has already been shown in Figure 5.14 **a**. In addition to the measurements of $M(H)$ along the three crystal directions [100], [110] and [1$\bar{1}$0], the mean signal of these three measurements $\overline{M_{1T}}(T)$ is plotted as a black line. This $\overline{M_{1T}}(T)$, which is scaled to the applied external magnetic field by assuming a linear dependence, is also shown with the measurements at 0.1 T (Figure 6.6 **b**) and 0.01 T (Figure 6.6 **c**) for comparison. As shown, the curve of $\overline{M_{1T}}(T)$ is in good agreement with the measurements at lower magnetic fields for temperatures above 100 K. This fact applies to all three crystal directions, [100], [110] and [1$\bar{1}$0]. Below 100 K, however, the measurements at lower fields deviate significantly from

$\overline{M_{1\,\mathrm{T}}}(T)$.

At an external magnetic field of 0.1 T, an additional signal with a significant anisotropy between the measurements along the different crystal directions is observed below 100 K, as shown in Figure 6.6 **b**, however, the characteristic cusp at T_{N} is still visible. At very low temperatures, this anisotropy seems to diminish. The anisotropic feature is even more pronounced at a magnetic field of 0.01 T (Figure 6.6 **c**), where it nearly completely obscures the magnetic phase transition of the system. It appears to have a uniaxial in-plane magnetic anisotropy with the $[1\bar{1}0]$ direction as the easy axis as the signal is maximum in this direction. The uniaxial nature of this feature is confirmed by the fact that the magnitude of the additional dome-like $M(T)$ for the $[100]$ orientation agrees very well with the geometric 45° projection of the signal recorded for the $[1\bar{1}0]$ orientation $(M_{0.01\,\mathrm{T}}^{[100]}(60\,\mathrm{K})/M_{0.01\,\mathrm{T}}^{[1\bar{1}0]}(60\,\mathrm{K}) \approx 0.7)$.

To better investigate the magnitude of the additional signal, the scaled $\overline{M_{1\,\mathrm{T}}}(T)$ is subtracted from the 0.1 and 0.01T measurements. As for the nonlinear signal, the values are converted into units of Bohr magnetons per surface Mn atom ($\mathrm{Mn_{surf}}$), assuming that only one surface layer of CuMnSb with the height of one lattice parameter contributes to the additional signal. The resulting curves are plotted in Figure 6.6 **d** for 0.1 T and in Figure 6.6 **e** for 0.01 T. For the two magnetic field strengths, the signal is of comparable magnitude. Signal magnitudes of ~2 $\mu_b/\mathrm{Mn_{surf}}$ in $[1\bar{1}0]$ orientation again indicate that the additional feature is a surface, or interface effect. Further, the uniaxial in-plane anisotropy with easy axis along the $[1\bar{1}0]$ crystal direction suggests that the signal studied here, and the nonlinear signal presented in section 6.1 are of the same origin.

In order to verify whether the additional signal and its anisotropy is a universal property of epitaxial CuMnSb, the measurements are repeated for two additional samples, which differ in film thickness, in the material used for capping and the substrate material. Figure 6.7 shows the $M(T)$ measurements on these samples along the $[110]$ and $[1\bar{1}0]$ crystal directions at an external magnetic field of 0.1 T. As for the previous considered sample, the average signal $\overline{M_{1\,\mathrm{T}}}(T)$ measured at 1 T is scaled linearly to a field of 0.1 T. After substracting the scaled $\overline{M_{1\,\mathrm{T}}}(T)$ from the 0.1 T measurements, the obtained values are converted to units of Bohr magnetons per surface Mn atom.

Measurements of a 220 nm thick CuMnSb layer grown on GaSb and capped with $\mathrm{Al_2O_3}$ are shown in Figure 6.7 **a**. The signals along the two crystal directions begin to diverge below a temperature of 120 K and exhibit an anisotropy with a $[1\bar{1}0]$ easy axis similar to the 510 nm thick CuMnSb layer studied previously. The same statement can be made for the 40 nm thick CuMnSb layer grown on InAs and capped with Ru, which is analyzed in Figure 6.7 **b**. Only the temperature below which the measurements diverge along the different orientations is slightly
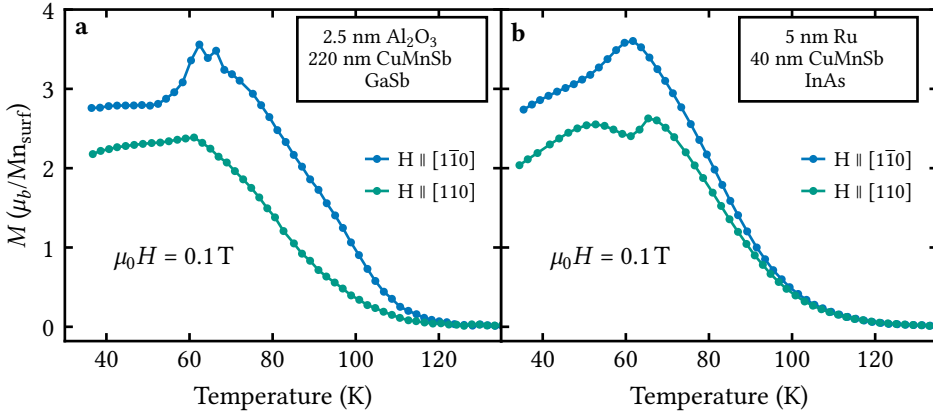
Figure 6.7: **Temperature dependent magnetization $M(T)$ of two different CuMnSb layers at weak magnetic fields.** **a** $M(T)$ at a magnetic field of 0.1 T of a 220 nm thick CuMnSb layer grown on GaSb and capped with Al_2O_3 ⬙H1300 . The measurements are compensated using the COMP method described in section 3.4. **b** $M(T)$ at a magnetic field of 0.1 T of a 40 nm thick CuMnSb layer grown on InAs and capped with Ru ⬙H1202 . The measurements are compensated using the CSH method described in section 3.4. For both samples, the average $M(T)$ at 1 T is subtracted, and the resulting values are converted into units of Bohr magnetons per surface Mn atom.

reduced. For both samples, the magnitude of the additional signal is slightly higher with ~3.5 μ_b/Mn$_{surf}$, but still of comparable size to the 510 nm thick CuMnSb layer. However, the shape of the curves differs slightly from sample to sample.

The fact that the additional feature occurs with comparable strength and anisotropy in samples with different CuMnSb film thicknesses, substrates, and cap materials strongly indicates that it is a universal property of epitaxial CuMnSb. However, the different shapes of the curves indicate that the origin of the signal is complex in nature. As already mentioned, a possible source could again be uncompensated moments on the CuMnSb surface. The strong uniaxial anisotropy of the additional signal in $M(T)$ could then result either from coupling of these uncompensated moments to the adjacent antiferromagnetically coupled moments or from the surface morphology, which might differ from sample to sample.

Up to this point, $M(T)$ of epitaxial CuMnSb has only been investigated through FC and FCW measurements, with application of an external magnetic field during cooling. The influence of this applied field on the $M(T)$ curve is analyzed through comparison of FCW $M(T)$ measurements with zero field cooled warming (ZFCW) measurements, in which the sample is cooled with no external magnetic field applied[1]. An external magnetic field is applied again to measure the magnetic

---

[1]The remanent magnetic field due to trapped magnetic flux in the superconducting magnet may be

moment during warm-up. This method allows the sample to enter its magnetic ground state during cooling without being affected by a magnetic field.

The comparison of FCW and ZFCW M(T) measurements is again performed with the 510 nm thick stoichiometric CuMnSb layer grown on GaSb to obtain a sufficiently large signal even at weaker magnetic fields. Figure 6.8 shows the resulting measurements at magnetic fields of 1 T, 0.1 T, and 0.01 T along the [110] and [1$\bar{1}$0] crystal directions. In addition to the $M(T)$ measurements shown in the left column, the differences between the FCW and ZFCW measurements are shown in the right column.

At an external magnetic field of 1 T (Figure 6.8 **a**), at first glance there is no visible difference between the FCW and ZFCW curves. However, considering the difference between the two curves in Figure 6.8 **b**, it becomes apparent that there is a deviation, especially at low temperatures. This deviation is of the same magnitude for each of the measured orientations. Due to the increased signal noise at higher temperatures[2], a statement about the temperature at which the bifurcation of the curves begins is not possible at 1 T. Reducing the external magnetic field to 0.1 T makes the bifurcation between the FCW and ZFCW $M(T)$ curves clearly visible (Figure 6.8 **c**). For both orientations, the ZFCW curves show a lower magnetization in the antiferromagnetic state. An isotropic difference between the FCW and ZFCW curves is shown in Figure 6.8 **d**. Starting at T_N, the bifurcation grows towards lower temperatures for both crystal directions. As can be seen in Figure 6.8 **e**, the magnitudes of the ZFCW measurements are further below those of the FCW measurements when the magnetic field is further reduced to 0.01 T. By analyzing the corresponding differences in Figure 6.8 **f**, bifurcation is shown not only to switch from isotropic to anisotropic but also begins well above T_N.

Several possible origins exist for the bifurcation of the ZFCW and FCW $M(T)$ measurements. The most obvious explanation for this behavior in an antiferromagnet is favoring of certain magnetic domains by the external magnetic field applied during cooling. If a field is applied when passing the magnetic phase transition, domains with perpendicular orientation of the magnetic moments to the magnetic field could be energetically more favorable than domains with magnetic moments oriented parallel to the magnetic field. This mechanism would explain, in particular, the lower magnetization of the ZFCW curves at low temperatures. In fact, if no magnetic domains are preferred by an external magnetic field, there could be domains with moments parallel to the field, which have a lower susceptibility, as well as domains with moments perpendicular to the field, which have a higher susceptibility. The signal measured when the sample is warmed up in the field then results from an average of the susceptibilities of the different domains. Obviously,

---

 up to ±1.5 mT [58]

[2]The signal noise of SQUID magnetometers increases both with temperature applied magnetic field
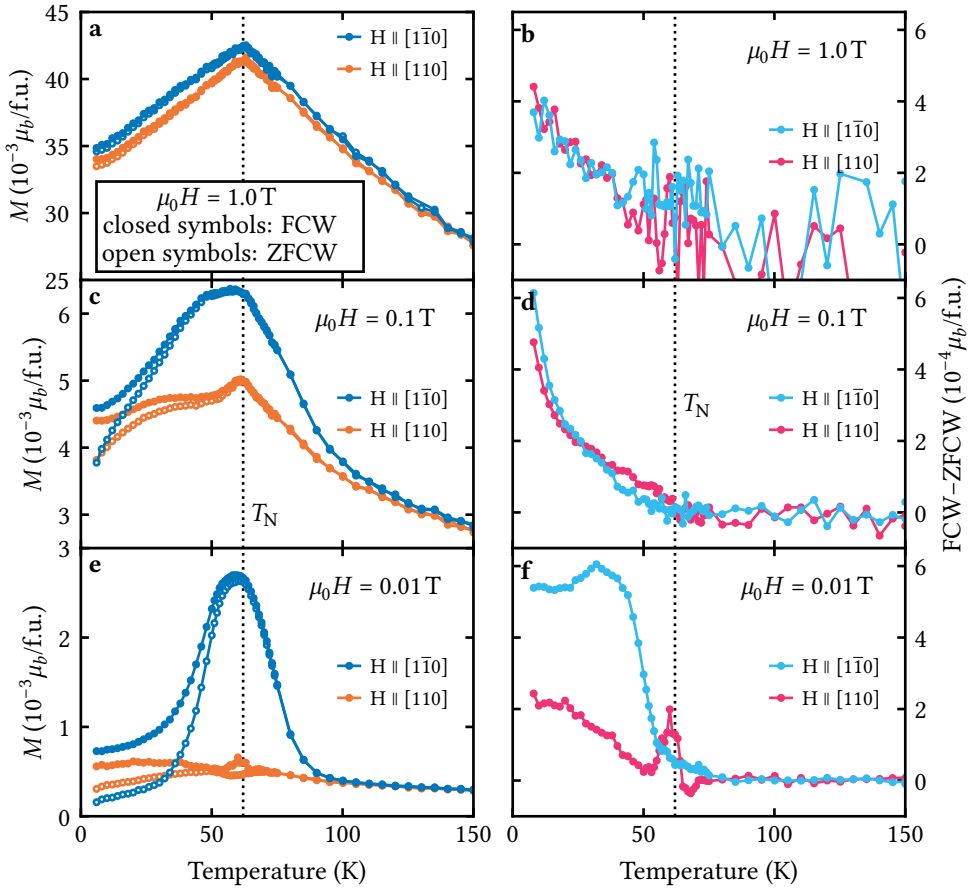
Figure 6.8: **Bifurcation of ZFCW and FCW measurements of the temperature dependent magnetization** $M(T)$ **of epitaxial CuMnSb.** 📚 H1265 The measurements are compensated using the COMP method described in section 3.4. ZFCW (open symbols) and FCW (closed symbols) $M(T)$ measurement along the crystal directions [110] and [1$\bar{1}$0] are shown in the left column for magnetic fields of 1 T (**a**), 0.1 T (**c**) and 0.01 T (**e**). The right column shows the corresponding differences between the ZFCW and FCW $M(T)$ measurement along the crystal directions [110] and [1$\bar{1}$0] for magnetic fields of 1 T (**b**), 0.1 T (**d**) and 0.01 T (**f**).

such a signal is smaller than that of exclusively high susceptible domains with moments perpendicular to the field, which may be favored by the presence of an external magnetic field during cooling, as is the case for the FCW measurements.

However, as previously reported, an uncompensated surface moment could be present at the surface of epitaxial CuMnSb. Therefore, the origin of the bifurcation could also be explained in this context. As shown in section 6.1 (Figure 6.3), the

uncompensated surface moments show signs of superparamagnetic behavior at intermediate temperatures. If they are superparamagnetic in nature, one would expect a net moment of zero at low temperatures when cooling them below their blocking temperature[3] without an applied magnetic field, which is the case for the ZFCW measurements. This would imply for the ZFCW measurements that no further contribution to the antiferromagnetic signal is to be expected from superparamagnetic surface moments. In contrast, cooling superparamagnetic surface moments below their blocking temperature in the presence of an applied magnetic field, as it happens during FCW measurements, will result in a non-zero net moment of the uncompensated surface moments. The uncompensated surface moments would thus lead to an additional signal, more precisely a positive offset, in the FCW measurements and thus, as observed, to a bifurcation between the ZFCW and FCW measurements.

As can be seen from the temperature dependent investigations of the nonlinear component of the magnetic field dependent magnetization (Figure 6.4 in section 6.1), the magnetic field required to saturate the uncompensated surface moments is very small at higher temperatures. It can therefore be assumed that the magnetic field strengths used for the FCW measurements are sufficient to bring the surface moments into saturation. The strength of the bifurcation caused by surface moments would therefore be independent of the strength of the magnetic field applied during cooling. This fact is also evident from the measurements and is a further argument for uncompensated surface moments as the cause of bifurcation. In contrast, in the case of an influence of antiferromagnetic domains, one would expect an increase of the bifurcation with the magnetic field strength, since one would expect more high susceptible domains with moments perpendicular to the magnetic field at higher cooling fields.

As mentioned before, the bifurcation at a magnetic field of 0.01 T shows an anisotropy between the crystal directions [110] and [1$\bar{1}$0]. This is strongly reminiscent of the anisotropy observed for the temperature dependent magnetization at weak magnetic fields (see Figure 6.6) and which has been attributed to the surface moments. Another common feature of the bifurcation and the additional signal of the temperature dependent measurements of the magnetization at a magnetic field of 0.01 T is that both exist above T_N. However, while the latter signal is also present for higher magnetic fields, the bifurcation vanishes above T_N for magnetic fields of 0.1 T and 1 T.

Since there are indications for and against both of the presented mechanisms, a combination of them is also possible. Thus, the uncompensated surface moments, when coupled to the antiferromagnetic moments, could also be affected by the

---

[3]Temperature below which the thermal energy becomes so low that the magnetic moments no longer fluctuate and are therefore blocked

antiferromagnetic domain structure. The bifurcation could therefore be indicative of the magnetic domain structure in CuMnSb. By magnetic measurements only, which like the SQUID magnetometer can only detect the external magnetic moment of a sample, it is difficult to make clear statements about the origin of this bifurcation. Imaging methods that can resolve the magnetic structure at the surface (like spin-polarized scanning tunneling microscopy) would be a suitable way to investigate at least the influence of the surface moments in more detail.

A bifurcation of ZFCW and FCW $M(T)$ measurements, which strengthens relative to the signal toward weaker magnetic fields, was also observed for CuMnSb bulk material, proposed to be caused by spin disorder in the system [27]. In the context of the bifurcation properties presented here, this spin disorder could be explained on the one hand by the presence of different antiferromagnetic domains. On the other hand, uncompensated moments could also play an important role in the bulk material. Their presence at the CuMnSb surface as well as at the crystalline boundaries of polycrystalline bulk material is conceivable.

In the following, it will be clarified whether the additional Curie-Weiss regime with positive Θ_{CW}, which was found for the 40 nm thick CuMnSb layer grown on InAs in subsection 5.1.3, is a universal property of epitaxial CuMnSb. Therefore, based on the $M(T)$ measurements on the 510 nm thick CuMnSb layer shown in Figure 6.6, the temperature dependence of the inverse susceptibility $\chi^{-1}(T)$ along the [$1\bar{1}0$] direction is investigated in more detail. Figure 6.9 **a** shows $\chi^{-1}(T)$ for external magnetic fields of 1 T, 0.1 T and 0.01 T. In the temperature range above 100 K all three curves coincide and follow Curie-Weiss behavior. A linear fit in this temperature range gives a Θ_{CW} of -100 K and an effective moment of $\mu_{eff} = 5.6 \, \mu_B$/f.u. as already reported in subsection 5.2.3. The Θ_{CW} of this high temperature regime is labelled as $\Theta_{CW,HT}$.

For an external magnetic field of 1 T, $\chi^{-1}(T)$ follows the indicated high temperature Curie-Weiss fit down to T_N. So only one Curie-Weiss regime can be observed. For fields smaller than 1 T, the additional signal previously attributed to uncompensated surface moments (see Figure 6.6) results in an additional linear regime, with positive Θ_{CW} below 100 K. This indicates that in this temperature range ferromagnetic or ferromagnetic-like correlations dominate antiferromagnetic correlations. Similar behavior has been observed for antiferromagnetic materials that show spin-glass behavior [107, 108]. The Θ_{CW} of this low temperature regime is labelled as $\Theta_{CW,LT}$. This second Curie-Weiss regime is similar to that found for the 40 nm thick CuMnSb layer on InAs. The fact that it occurs in this thinner CuMnSb layer even at a magnetic field of 1 T is due to the increased surface to volume ratio. In thicker CuMnSb layers, the volume signal dominates the signal of the uncompensated surface moments already at lower magnetic fields.

As shown in Figure 6.9 **a**, $\Theta_{CW,LT}$ shows a dependence on the applied magnetic
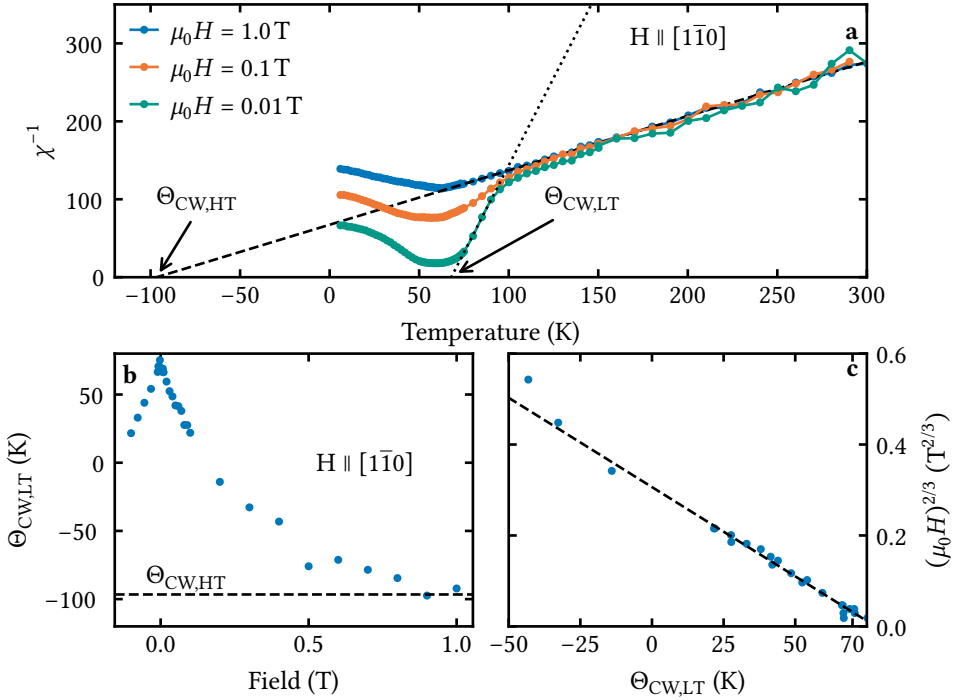
Figure 6.9: **Investigation of the second Curie-Weiss regime of epitaxial CuMnSb.** 🔖H1265 The measurements are compensated using the COMP method described in section 3.4. **a** Inverse susceptibility of CuMnSb for magnetic fields of 1 T, 0.1 T and 0.01 T along the [1$\bar{1}$0] crystal direction. Dashed lines indicate the Curie-Weiss behavior for the high and low temperature regimes. Labels indicate the high ($\Theta_{CW,HT}$) and low ($\Theta_{CW,LT}$) temperature Curie-Weiss temperature. **b** Curie-Weiss temperature obtained along the [1$\bar{1}$0] crystal direction for the low temperature regime as a function of magnetic field. The Curie-Weiss temperature obtained for the high temperature regime is indicated by a dashed line. **c** De Almeida-Thouless plot of Curie-Weiss temperatures obtained for the low temperature regime. A linear fit is indicated as a dashed line.

field. To investigate this dependence in more detail, $\Theta_{CW,LT}$ is determined for various fields ranging from −0.1 to 1 T. Figure 6.9 **b** shows the resulting $\Theta_{CW,LT}$ as a function of the applied field. Towards larger fields $\Theta_{CW,LT}$ decreases and converges to the Curie-Weiss temperature of the temperature range above 100 K ($\Theta_{CW,HT}$). The decrease towards higher fields is symmetrical around zero field.

In small fields, $\Theta_{CW,LT}$ follows an $H^{2/3}$ behavior as can be seen in Figure 6.9 **c**. According to the de Almeida-Thouless relation, such behavior is an indication of a spin-glass phase [109]. Therefore, it appears that the additional signal, which presumably comes from the uncompensated surface moments, has spin-glass-like

properties at low temperatures. Spin-glass behavior of uncompensated surface moments has also been found at the surface of NiO nanoparticles [105]. As mentioned before, NiO shares the AFM111 antiferromagnetic structure with CuMnSb. This commonality may indicate that the complex magnetism at the surface is a more general phenomenon of type-II antiferromagnets with ferromagnetic order in the {111} planes and antiferromagnetic order between the {111} planes rather than just a material property.

6.3 THERMOREMANENT MAGNETIZATION OF EPITAXIAL CuMnSb

The bifurcation of FCW and ZFCW $M(T)$ measurements suggests that epitaxial CuMnSb features a thermoremanent magnetization (TRM)[4] at low temperatures. To study this TRM in more detail, the thermoremanent state is prepared in a 60 nm thick CuMnSb layer grown on InAs by cooling it in a magnetic field of 0.1 T. Subsequently, the magnetization is measured using the SQUID magnetometer while the sample is heated without a magnetic field. In order to examine whether the TRM is due to spontaneous magnetization, the heating is carried out in thermal cycles. Thereby, the temperature is increased by a certain amount and then cooled back to the initial temperature, with the maximum temperature being increased after each cycle. The time evolution of the temperature during this procedure is shown in the inset of Figure 6.10 **a**. Since the diamagnetism of the substrate, the paramagnetism of the Ru cap, and the antiferromagnetism of the CuMnSb layer do not contribute to the signal at zero field, compensation for the TRM measurements is not required. Therefore, the raw magnetization measurements are analyzed.

The TRM measurements are performed along the [110] (Figure 6.10 **a**) and [1$\bar{1}$0] (Figure 6.10 **b**) crystal directions. Up to a temperature of ~20 K, the measured signal is comparable along the two orientations. The magnetization decreases when the sample is heated. Considering only the curve that would correspond to a continuous warm-up, a strong similarity to the bifurcation of the FCW and ZFCW $M(T)$ measurements studied in Figure 6.8 is evident. However, during recooling, the magnetization remains constant for all thermal cycles up to 20 K. The magnetization only starts to decrease again when the previous maximum temperature is exceeded. For the [110] orientation, this even applies to the entire temperature range. Such behavior has been reported to be indicative of superparamagnetism as well as spin-glass phases [111]. Furthermore, spontaneous magnetization can be excluded as a cause for the TRM. In the [1$\bar{1}$0] orientation, an additional feature appears around T_{N}, both on heating and cooling, indicating some sort of spontaneous

---

[4]Magnetization of a material that is persistent after being generated by an applied magnetic field during cooling through the magnetic phase transition of the material [110]
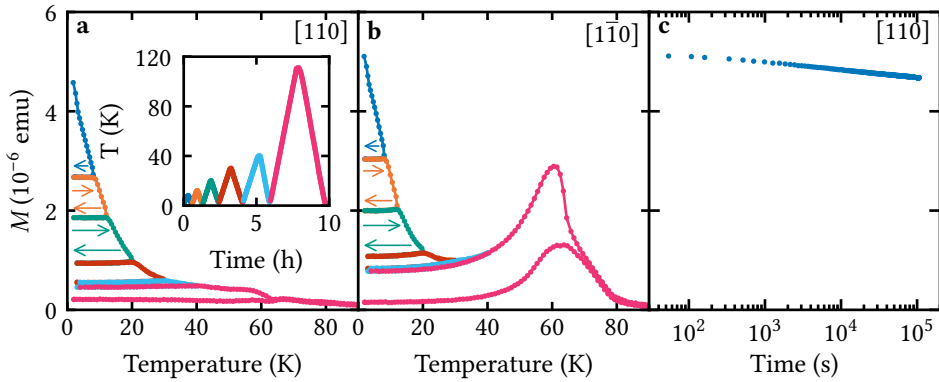
Figure 6.10: **Thermoremanent magnetization (TRM) and its behavior during thermal cycling of epitaxial CuMnSb** ❧ H1310 The measurements are uncompensated and show the raw magnetization data. A field of 0.1 T is applied during cooldown to prepare the thermoremanent state. Subsequently, the sample is heated and cooled in thermal cycles without an applied magnetic field. The maximum temperature is increased after each cycle. The inset in **a** shows the time evolution of the temperature during thermal cycling for both orientations. Each cycle is plotted with a different color for better distinguishability. **a** TRM along the [110] crystal direction. **b** TRM along the [1$\bar{1}$0] crystal direction. **c** Decay of the TRM signal over time at a constant temperature of 10 K.

magnetization. Interestingly, the signal decays toward lower temperatures. An explanation for the origin of this signal is still to be found. The development of the TRM over time at a constant temperature of 10 K is shown in Figure 6.10 **b** for [110] orientation. It shows an exponential decay of the magnetization over time which is typical for disordered systems like spin-glasses.

The TRM, in particular the behavior of the TRM during thermal cycling, is another indication of a superparamagnetic or a spin-glass phase in epitaxial CuMnSb. As explained in the previous section, its origin probably stems from uncompensated surface moments. Whether it is ultimately a superparamagnetic or a spin-glass phase cannot be concluded. A superparamagnetic phase that becomes a spin glass at lower temperatures is also conceivable. In favor of the latter is the fact that signs of superparamagnetic behavior, like the saturating nonlinear component of $M(H)$ with absent residual magnetization were found at higher temperatures, and signs of a spin glass, like the TRM and the linear $H^{2/3}$ dependence of $\Theta_{CW,LT}$ at lower temperatures.

6.4 Exchange bias

The exchange bias effect originates from exchange interactions between ferromagnetic and antiferromagnetic layers at their interface [112]. One of the goals of the development of epitaxial growth of CuMnSb is the fabrication of fully epitaxial heterostructures from antiferromagnetic CuMnSb and ferromagnetic NiMnSb. The exchange bias effect between the antiferromagnetic CuMnSb layer and the ferromagnetic NiMnSb layer can have a great influence on the functionality of possible electrical devices made of such heterostructures. It is therefore of particular interest whether and to what extent epitaxial CuMnSb exhibits the exchange bias effect at the interface with ferromagnets. For this reason, the exchange bias effect is investigated for various ferromagnetic materials deposited on the epitaxial CuMnSb.

The studied layer stacks are based on 40 nm thick CuMnSb layers grown on GaSb substrates. As soon as the substrate is cooled down below 200 °C after CuMnSb growth, the samples are transferred to the sputtering chamber without leaving the UHV. There, the ferromagnetic layers are deposited on the CuMnSb layer by means of DC-magnetron sputtering at room temperature. In total, the exchange bias effect is investigated with four different ferromagnets: Co, CoFe and NiFe as in-plane ferromagnets and a Co/Pd superlattice as an out-of-plane ferromagnet. Of the three in-plane ferromagnets, a layer with a thickness of 3 nm is deposited on the CuMnSb surface of the respective sample. Subsequently, a 5 nm thick Ta intermediate layer is deposited, followed by a 5 nm thick Ru cap. The Co/Pd superlattice is composed of 20 alternating 0.4 nm thick Co layers and 1.1 nm thick Pd layers, resulting in a total thickness of 30 nm. A Ru layer of 5 nm thickness is used to cap the Co/Pd superlattice. The parameters used for sputtering these materials are listed in Table 6.1.

The exchange bias measurements are performed using the following protocol by the SQUID magnetometer: First, the sample is cooled from 300 K to 4 K in a magnetic field of 500 mT, which is above the saturation field of the used ferromagnets. The

Material	DC-power (W)	Ar pressure (mbar)	deposition rate (nm min^{-1})
Co	50	5×10^{-3}	6.0
CoFe	100	5×10^{-3}	9.0
NiFe	50	5×10^{-3}	5.5
Co/Pd SL	22/23	5×10^{-3}	2.4/6.0
Ta	50	5×10^{-3}	5.0

Table 6.1: **Parameters used for sputter deposition of the ferromagnetic layers and the Ta layer.**
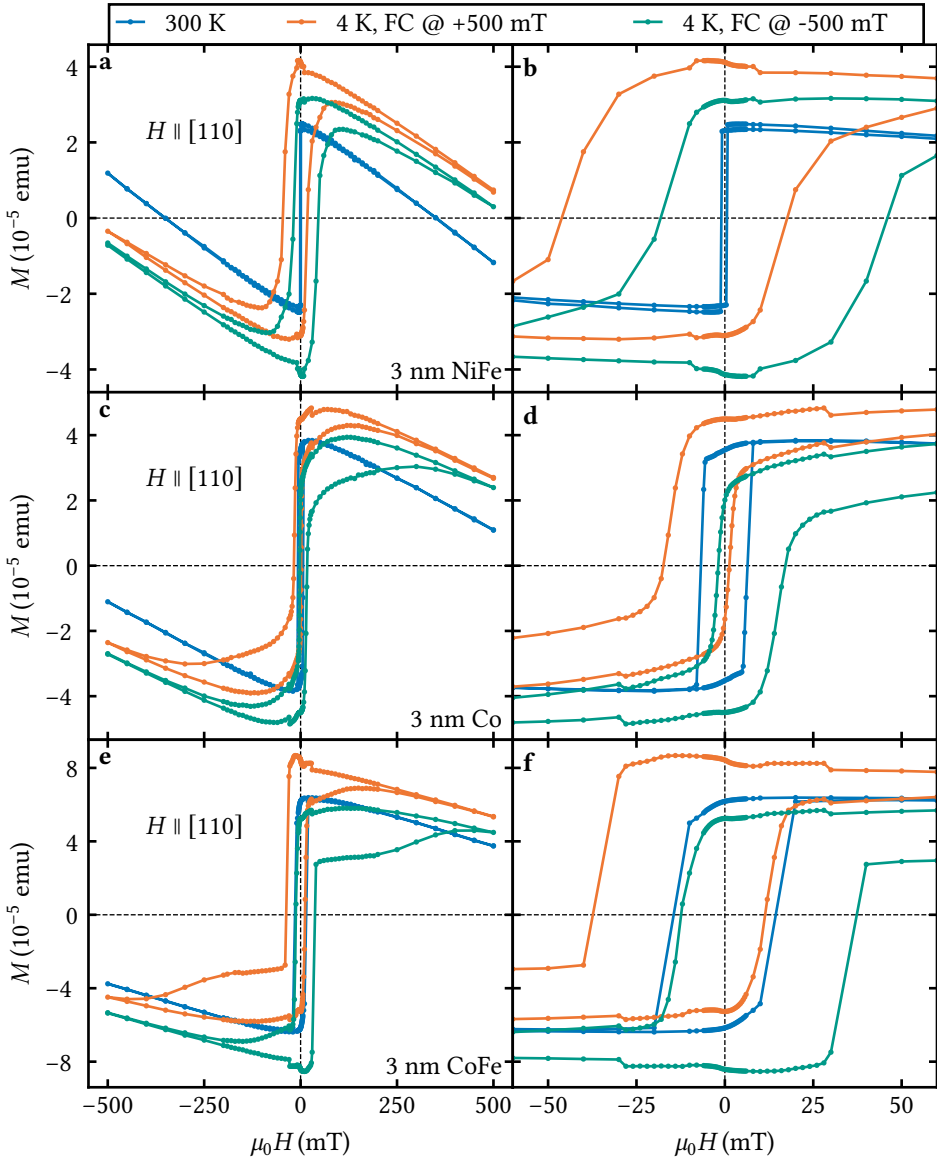
Figure 6.11: **Investigation of the exchange bias effect on epitaxial CuMnSb in combination with in-plane ferromagnets. a** Exchange bias measurements with 3 nm NiFe as the ferromagnetic layer ⬚H1301. **b** magnification of **a**. **c** Exchange bias measurements with 3 nm Co as the ferromagnetic layer ⬚H1302. **d** magnification of **a**. **e** Exchange bias measurements with 3 nm CoFe as the ferromagnetic layer ⬚H1303. **f** magnification of **a**.

CuMnSb layer thus undergoes the magnetic phase transition from the paramagnetic to the antiferromagnetic state while the magnetic moments in the ferromagnetic layer are aligned to the external magnetic field. A hysteresis curve is then recorded at 4 K. Afterward, the sample is warmed again to 300 K. The magnetic field is then applied in the opposite direction (−500 mT), and the procedure described above is repeated.

Figure 6.11 summarizes the measurements for the three in-plane ferromagnetic materials. Measurements at 4 K of the sample with NiFe as the ferromagnetic layer in Figure 6.11 **a** show a vertical shift that can be attributed to the TRM resulting from the cooling of the CuMnSb layer in a magnetic field, as described in section 6.3. In the magnification of these measurements in Figure 6.11 **b**, one can clearly observe a horizontal shift due to the exchange bias effect as well. The exchange bias field is determined to be 18 mT for the sample containing the NiFe layer. Figure 6.11 **c** and Figure 6.11 **d** show the exchange bias measurements for the sample with 3 nm Co. Also for this sample a vertical, as well as a horizontal shift can be observed for the measurements at 4 K. The horizontal shift and thus the exchange bias field is 8 mT. Finally, the exchange bias effect is also observed for the third investigated in-plane ferromagnet, CoFe. The horizontal shift of the measurements at 4 K is clearly visible in Figure 6.11 **e** and Figure 6.11 **f**. The exchange bias field is 13 mT.

Figure 6.12 shows the exchange bias measurements on the sample with the Co/Pd superlattice, which is an out-of-plane ferromagnet. Looking at the raw data in Figure 6.12 **a**, as with the in-plane ferromagnets, a vertical shift between the measurements with opposite cooling fields can be seen. This can again be attributed to the TRM. The magnification of the raw data in Figure 6.12 **c** also suggests a horizontal shift in the two curves. Subtracting the linear background, however, Figure 6.12 **b** and the magnification in Figure 6.12 **d** reveal that without the TRM signal from the CuMnSb layer, the two curves coincide. Thus, no exchange bias can be observed for the out-of-plane ferromagnet.

The exchange bias effect is a result of an exchange interaction of the uppermost moments of the antiferromagnet and the lower moments of the ferromagnet. Therefore, to find a possible reason why the exchange bias effect occurs in in-plane ferromagnets but not in out-of-plane ferromagnets, the CuMnSb surface must be considered. In section 6.2 a strong uniaxial in-plane anisotropy was found for the surface moments of CuMnSb. It is likely that these surface moments play a major role in the exchange interaction leading to the exchange bias. The strong in-plane anisotropy seems to favor an exchange interaction with in-plane ferromagnets. An exchange interaction with out-of-plane ferromagnets, on the other hand, is apparently prevented.
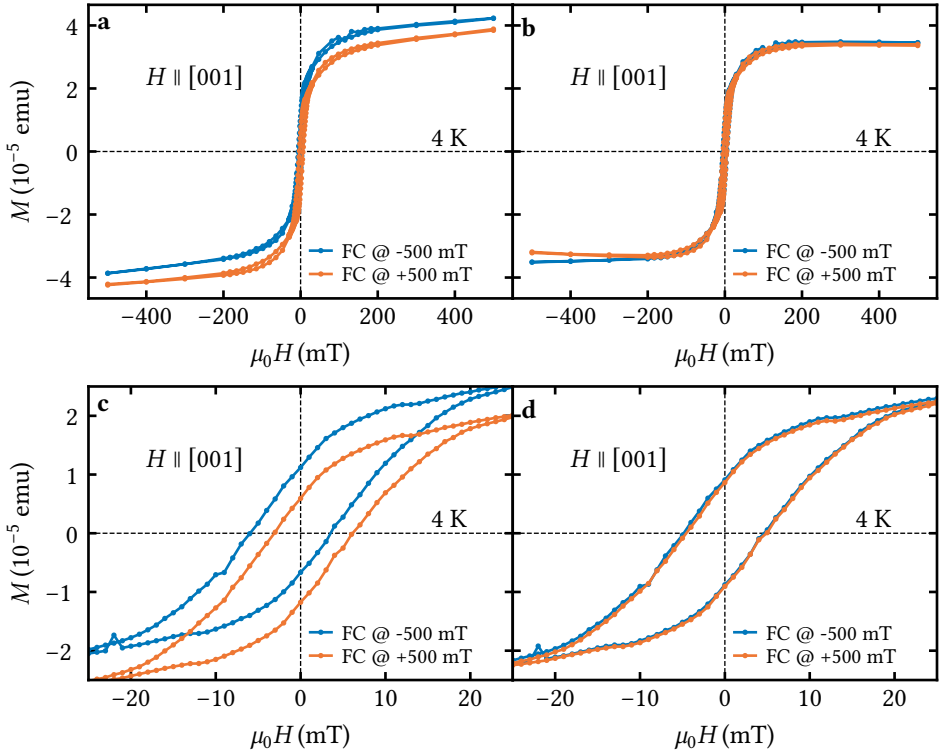
Figure 6.12: **Investigation of the exchange bias effect on epitaxial CuMnSb in combination with a Co/Pd superlattice as an out-of-plane ferromagnet.** 📚 H1373 **a** Raw exchange bias measurements. **b** Exchange bias measurements with linear background subtracted. **c** magnification of **a**. **d** magnification of **b**.

6.5 Low-energy muon spin rotation experiment on epitaxial CuMnSb

Muon spin rotation (μSR) can be used to study local magnetic properties in crystals. It is based on the fact that the motion of the muon spin of spin-polarized muons previously implanted into the crystal depends on the local magnetic field surrounding the muon. A detailed introduction to μSR can be found in [113]. To further investigate the magnetism of epitaxial CuMnSb, μSR experiments were performed on two CuMnSb samples at the low-energy μSR spectrometer (LE-μSR) at the μE4 beamline [114] of the Swiss Muon Source (Paul Scherrer Institute, Switzerland). The experiment was conducted and the results evaluated by Dr. Thomas Prokscha, Dr. Xiaojie Ni, and Maria Inès Mendes Martins from the aforementioned facility. The first results of this experiment are presented in the following.

As mentioned above, spin-polarized muons are implanted into the sample for the μSR experiment. In the experimental setup used, the muons can therefore be tuned to implantation energies between 1 and 30 keV before they hit the sample. This energy range corresponds to penetration depths between 1 and 300 nm. Inside the sample, the muons come to rest mainly at interstitial sites or atomic vacancies before decaying after an average lifetime of 2.2 μs into a positron and two neutrinos. Since the positrons produced by this decay are emitted preferentially in the direction of the muon spin, the muon spin at the time of the decay can be inferred from the direction of motion of the positron.

The results presented in this section are performed in the so-called transverse field configuration. In this configuration, a weak external magnetic field of 5 mT is applied perpendicular to the muon spin during the experiment. Here, the muon spin is in the plane of the sample and the external magnetic field is perpendicular to the sample surface. The external magnetic field causes the muon spin to precess at the Larmor frequency in the plane of the sample. Detecting the spatial emission of positrons originating from the decay of a muon ensemble in this configuration as a function of time will thus give information on the time evolution of the muon spin. The spatial resolution is achieved by using four positron detectors, each of which covers a sector of 90° of the precession plane of the muon spins. Considering the measured values of the entire muon ensemble, this results in an oscillating signal for each of the detectors as a function of time. The initial amplitude of this signal is called the initial decay asymmetry. If, in addition to the external magnetic field, internal local magnetic fields (e.g. due to magnetic moments), which vary in time and/or space, are present, the individual muon spins of the ensemble will have different precession frequencies. As a result, the phase relation of the individual muon spins decreases, which leads to an attenuation of the signal and a decrease in the initial decay asymmetry. The initial decay asymmetry can therefore be used to infer which fraction of the volume of the sample is magnetic and which is not. Typically, the non-magnetic volume fraction (NMVF) is used as a measure for this purpose.

The NMVF is shown for the investigated samples as a function of temperature and implantation energy in Figure 6.13. An implantation energy of 8 keV is used for the temperature dependent measurements. This corresponds to a muon penetration depth of ~40 nm. Figure 6.13 **a** shows the temperature dependence of the NMVF for a 220 nm thick CuMnSb layer grown on GaSb with Al_2O_3 cap. At temperatures above 60 K, in the paramagnetic state, a NMVF of ~ 0.7 is measured. Note that a value of 1 is not measured for the NMVF in the paramagnetic state because some muons miss the sample and depolarize rapidly in the Ni backing of the sample holder. The magnetic phase transition results in a sharp drop in the NMVF at 60 K towards lower temperatures. There is no difference in the measurement of
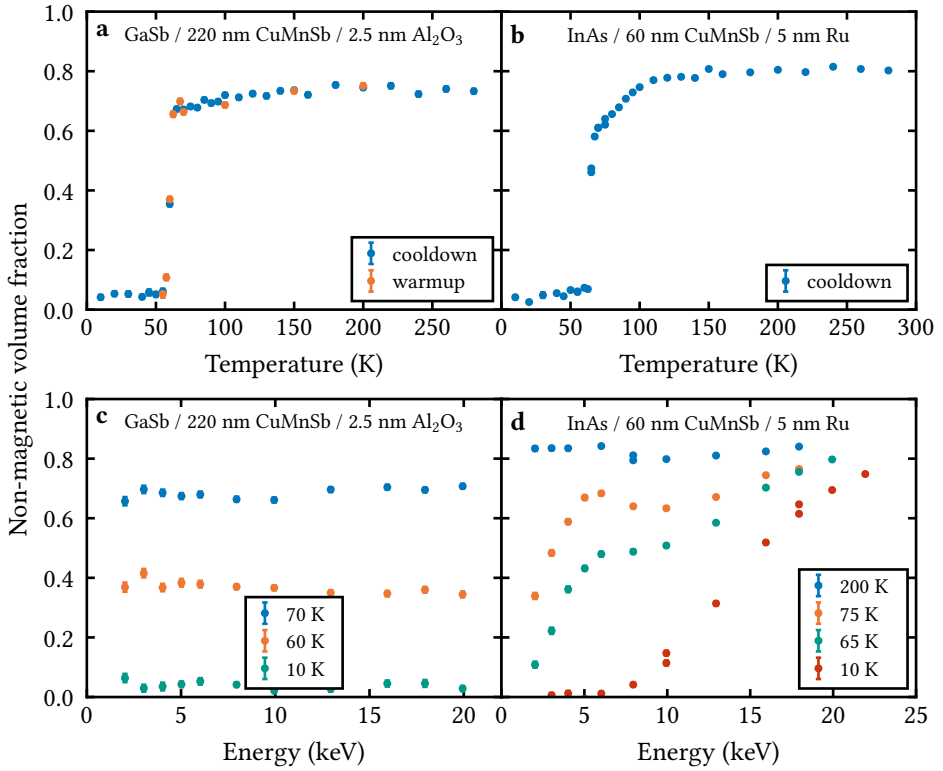
Figure 6.13: **Results of the μSR experiment performed on epitaxial CuMnSb.** All measurements are performed in the transverse field configuration with an external magnetic field of 5 mT. The temperature dependent non-magnetic volume fraction (NMVF) is measured at an implantation energy of 8 keV, corresponding to a penetration depth of ~40 nm. **a** Temperature dependend NMVF of a 220 nm thick CuMnSb layer grown on GaSb and capped with Al_2O_3 ⬙H1300. **b** Temperature dependend NMVF of a 60 nm thick CuMnSb layer grown on InAs and capped with Ru ⬙H1310. **c** Implantation energy dependend NMVF of a 220 nm thick CuMnSb layer grown on GaSb and capped with Al_2O_3 at temperatures of 70 K, 60 K, and 10 K. **d** Implantation energy dependend NMVF of a 60 nm thick CuMnSb layer grown on InAs and capped with Ru at temperatures of 200 K, 75 K, 65 K, and 10 K.

the NMVF between warming up and cooling down. The good agreement with T_N determined in other experiments shows that the magnetic phase transition of epitaxial CuMnSb can be well studied using μSR.

Compared to the sharp phase transition of the CuMnSb layer grown on GaSb, the NMVF of a 60 nm thick CuMnSb layer grown on InAs and capped with Ru shows a decrease already at a temperature of 100 K, as can be seen in Figure 6.13 **b**.

This observation indicates that regions with large internal magnetic fields are already formed in the sample above T_N. Similar behavior was also observed for the additional signal in the investigations of the temperature dependence of magnetization in weak magnetic fields in section 6.2. The magnetic transition from the paramagnetic state to the antiferromagnetic state is again indicated by a sharp drop in NMVF. The corresponding T_N value of 65 K is consistent with the value determined by SQUID magnetometry measurements for this sample.

Figure 6.13 **c** and **d** shows the NMVF at different temperatures as a function of the implantation energy of the two CuMnSb samples. In this way, the NMVF can be investigated for the respective temperature in a depth dependent manner. The CuMnSb layer grown on GaSb shows a constant NMVF over the entire energy range for all temperatures investigated (Figure 6.13 **c**). At T_N, an NMVF of about half the value of the paramagnetic state is seen over the entire energy range, indicating that the magnetic phase transition occurs homogeneously throughout the CuMnSb layer. In contrast, the CuMnSb layer grown on InAs shows a much more complex behavior (Figure 6.13 **d**). While in the paramagnetic state, at a temperature of 200 K, a constant NMVF can be observed over the entire energy range, a decrease in NMVF towards lower energies can be seen at temperatures of 75 K, 65 K and 10 K. At temperatures of 75 K and 65 K, a low NMVF is only observed at very low implantation energies. This indicates magnetization at the sample surface and supports the conclusions drawn from the SQUID magnetometry measurements, which indicate surface magnetism at the CuMnSb surface. It is noteworthy that this magnetization already occurs above T_N, which again fits the observations from section 6.2. At 10 K, the CuMnSb layer seems to be completely magnetic, as shown by the low values of the NMVF up to energies of ~10 keV. Why there is no sharp transition to the diamagnetic InAs substrate is not yet understood. However, due to the antiferromagnetism in the CuMnSb layer, stray fields can be excluded. The NMVF measurements of the CuMnSb layer grown on GaSb show no additional magnetic signal at the surface, although for this sample the previously identified characteristic features for surface magnetism were found in SQUID magnetometry measurements. As so far only the two samples presented in this work have been investigated by μSR, it is not possible to draw a definite conclusion from this contradiction. μSR measurements on further samples are necessary to determine whether this is an isolated case and the surface signals measured by μSR and SQUID magnetometry are of the same origin, or whether two separate effects are observed.

The results presented here show that μSR is a suitable method for the investigation of the magnetism of epitaxial CuMnSb. Combined with SQUID magnetometry measurements, which provide a global picture of the magnetization, μSR as a local probe of the magnetization can be used to provide a more complete understanding of the complex magnetism of CuMnSb. In particular, the ability to control the muon

penetration depth by adjusting the implantation energy holds great potential to help in understanding the origin of surface magnetism of epitaxial CuMnSb.

6

7

CuMnSb/NiMnSb
heterostructures

The IEEE Roadmap for Emerging Materials for Spintronic Device Applications [115] predicts that all-Heusler ferromagnetic/antiferromagnetic junctions will play an important role in future spintronic applications. In the case of antiferromagnetic CuMnSb, ferromagnetic half-Heusler NiMnSb would be an ideal candidate material for the realization of such fully epitaxial heterostructures. Therefore, this chapter reports on the first attempts to fabricate fully epitaxial CuMnSb/NiMnSb heterostructures. First, the growth process of these heterostructures on InP substrates is presented, with initial structural studies performed using RHEED. Structural characterization is performed using HRXRD and secondary-ion mass spectrometry (SIMS). Furthermore, magnetic measurements are used to investigate the exchange bias effect between CuMnSb and NiMnSb.

7.1 Growth process

For the realization of the first fully epitaxial CuMnSb/NiMnSb heterostructures, InP is chosen as the substrate. Accordingly, the preparation of the samples starts with the growth of a (In,Ga)As buffer layer following the procedure described in subsection 4.2.3. Before the sample is transferred to the Heusler specific MBE chamber after buffer growth, this chamber is prepared for the growth of CuMnSb and NiMnSb. For this purpose, the cells for Cu, Ni, Mn, and Sb are heated to the required temperatures, and the cell shutters are cleaned according to the method described in section 4.3. Optimum material fluxes are calibrated by growing CuMnSb and NiMnSb single layers on InP substrates. The determined BEP values are 6.1×10^{-9} mbar for Cu, 5.1×10^{-9} mbar for Ni, 1.1×10^{-8} mbar for Mn and 5.5×10^{-8} mbar for Sb. Differences, in particular of Mn and Sb fluxes, to the stoichiometric growth of CuMnSb

on InAs and GaSb (cf. subsection 4.3.2), result from the fact that identical Mn and Sb fluxes were targeted for both CuMnSb and NiMnSb growth. This means that the cell temperatures do not have to be adjusted when changing from CuMnSb to NiMnSb growth.

After the sample is transferred to the Heusler specific MBE chamber, it is heated to the growth temperature of 250 °C with the main shutter closed. The growth of the CuMnSb layer is then carried out analogous to the process described in subsection 4.3.2. Once the desired CuMnSb layer thickness is reached, growth is interrupted by closing the main shutter and the shutter of the Cu cell. To prepare the growth of the NiMnSb layer, the shutter of the Ni cell is then opened, and the Ni flux is stabilized for 5 min. Subsequently, NiMnSb growth is initiated by opening the main shutter. Finally, NiMnSb growth is terminated by closing the main shutter and all cell shutters. After cooling, the sample is transferred to the sputtering chamber, where it is capped with a 5 nm thick Ru protective layer.

The surface reconstruction of the sample is extensively monitored by RHEED during the growth of the heterostructures. Figure 7.1 analyzes the surface reconstructions along the [110] and [1$\bar{1}$0] crystal directions at the three key stages of heterostructure growth, namely before CuMnSb growth, after CuMnSb growth, and after NiMnSb growth. The investigated heterostructure consists of 20 nm CuMnSb and 5 nm NiMnSb. Before CuMnSb growth the typical 4 × 3 reconstruction of (In,Ga)As is observed, as can be seen in Figure 7.1 **a** and **b**. During CuMnSb growth, this changes to a 4 × 4 reconstruction, which persists until the end of CuMnSb growth. The surface reconstruction after CuMnSb growth is shown in Figure 7.1 **c** and **d**. Another change in surface reconstruction results from the growth of NiMnSb. As shown in Figure 7.1 **c** and **d**, the NiMnSb surface shows a 2 × 2 reconstruction.

Figures 7.1 **g** and **h** show the RHEED intensities extracted from Figures 7.1 **a-f** by integrating over an horizontal area normalized to the maximum intensity. Along both the [110] and [1$\bar{1}$0] crystal directions, the positions of the first-order main streaks from the (In,Ga)As and the CuMnSb surfaces coincide. The horizontal lattice parameter of the CuMnSb surface thus matches that of the (In,Ga)As buffer layer, which is a sign of pseudomorphic growth of the CuMnSb layer. However, the positions of the first-order main streaks of the NiMnSb surface do not match those of the CuMnSb and (In,Ga)As layers. In detail, the distance between the two first-order main streaks of the NiMnSb surface is reduced, which is a sign of relaxation. Since the horizontal lattice parameter of the InP substrate and thus that of the (In,Ga)As buffer layer is known, the horizontal lattice parameter of the NiMnSb surface after growth can be inferred from the spacing of the first-order main streaks. With $a^{\parallel}_{\text{CuMnSb}} = a^{\parallel}_{\text{(In,Ga)As}} = a_{\text{InP}} = 5.87$ Å the horizontal lattice parameter of the NiMnSb surface can be calculated to be $a^{\parallel}_{\text{NiMnSb}} = 5.98$ Å.
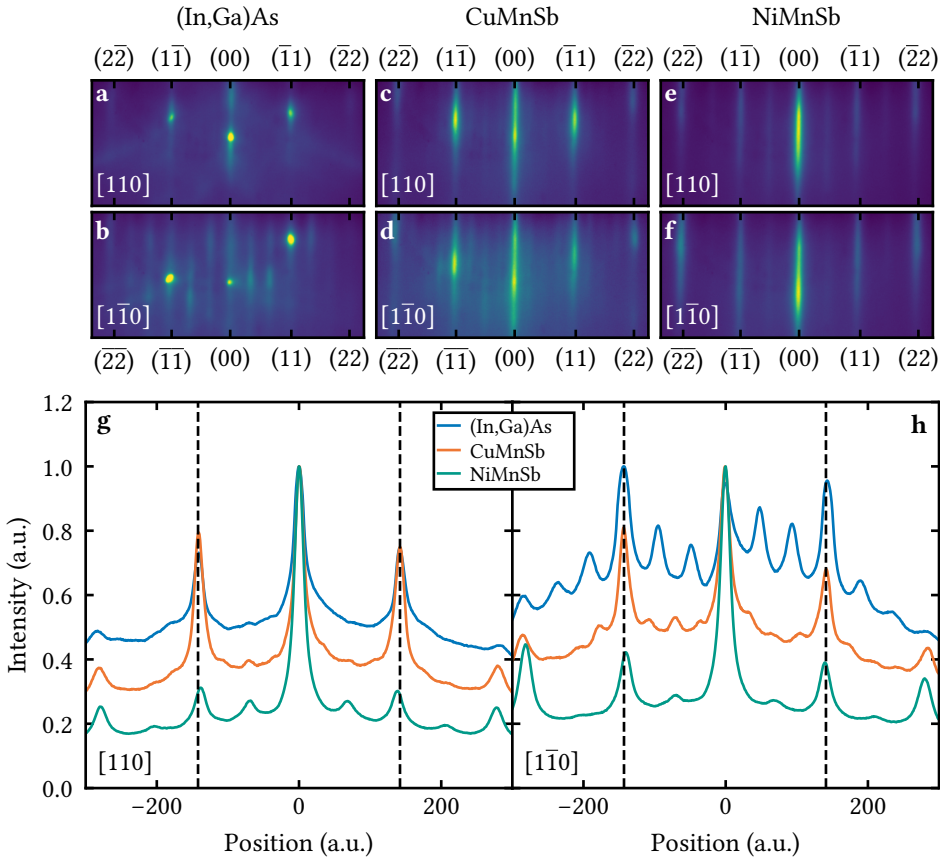
Figure 7.1: **RHEED development during growth of CuMnSb/NiMnSb heterostructures. a** d/4 surface reconstruction of the (In,Ga)As surface before CuMnSb growth in [110] crystal direction. **b** d/3 surface reconstruction of the (In,Ga)As surface before CuMnSb growth in [1$\bar{1}$0] crystal direction. **c** d/4 surface reconstruction of the CuMnSb surface after CuMnSb growth in [110] crystal direction. **d** d/4 surface reconstruction of the CuMnSb surface after CuMnSb growth in [1$\bar{1}$0] crystal direction. **e** d/2 surface reconstruction of the NiMnSb surface after NiMnSb growth in [110] crystal direction. **f** d/2 surface reconstruction of the NiMnSb surface after NiMnSb growth in [1$\bar{1}$0] crystal direction. **g** RHEED intensities along the [110] crystal directions normalized to the maximum intensity extracted from **a**, **c** and **e**. **h** RHEED intensities along the [1$\bar{1}$0] crystal directions normalized to the maximum intensity extracted from **b**, **d** and **f**.

The fact that the relaxation only occurs during NiMnSb growth is surprising in the sense that the CuMnSb layer has a much larger lattice mismatch to InP. One would therefore expect that relaxation is more likely to occur during CuMnSb growth. Therefore, in the next section, one of the aspects that are investigated

in more detail is the relaxation based on RSM measurements. Regardless of the occurrence of relaxation, the continuous two-dimensional surface reconstruction during the growth of the heterostructures can be considered as evidence that fully epitaxial growth of CuMnSb/NiMnSb heterostructures is possible.

7.2 Structural properties

The RHEED studies of the NiMnSb surface presented in the previous section show evidence of relaxation of CuMnSb/NiMnSb heterostructures grown on InP substrates. With the help of RSM measurements, the relaxation of the epitaxial layers will be investigated in more detail. Since the relaxation could only be observed during NiMnSb growth, a 40 nm thick CuMnSb single layer grown on InP, which did not show signs of relaxation in RHEED, is also examined in addition to the CuMnSb/NiMnSb heterostructure.

The RSM of the (224) diffraction peak of the CuMnSb single layer is shown together with the corresponding relaxation triangle in Figure 7.2 **a**. Since the material composition of the (In,Ga)As growth in this sample resulted in an (In,Ga)As buffer layer perfectly lattice-matched to the InP substrate, the diffraction peaks of InP and (In,Ga)As coincide. As can be seen, the CuMnSb peak is elongated along the relaxation triangle, which is a sign of partial relaxation. Apparently, this relaxation is not strong enough to be observed by RHEED investigations of the CuMnSb surface during growth.

Figure 7.2 **b** shows the RSM of the (224) diffraction peak for the CuMnSb/NiMnSb heterostructure with a CuMnSb thickness of 20 nm and a NiMnSb thickness of 5 nm. The relaxation triangles are drawn for both half-Heusler layers. Due to the imperfect calibration of the (In,Ga)As composition, the (In,Ga)As diffraction peak is slightly shifted along the [00L] direction below that of the InP substrate. The alignment along the [00L] direction is indicative of pseudomorphic growth of the (In,Ga)As buffer layer. Compared to the sample with a CuMnSb single layer, the CuMnSb diffraction peak no longer appears elongated but rather round. The peak position is very close to that of intrinsic CuMnSb, indicating a fully relaxed CuMnSb layer. The same observation can be made for the diffraction peak of the NiMnSb layer. Interestingly, both the CuMnSb and NiMnSb peaks are slightly shifted towards each other with respect to the intrinsic peak positions. Especially in comparison to the CuMnSb single layer, it can be stated that the additional NiMnSb layer leads to a complete relaxation of the CuMnSb layer.

For the fabrication of electrical devices from CuMnSb/NiMnSb heterostructures, pseudomorphic growth of both half-Heusler layers is essential. The relaxation of the epitaxial layers must therefore be prevented. This could be realized in the future either by growing thinner layers on InP substrates or by using a different substrate. In particular, growth on InAs is viable because the lattice parameter of InAs is
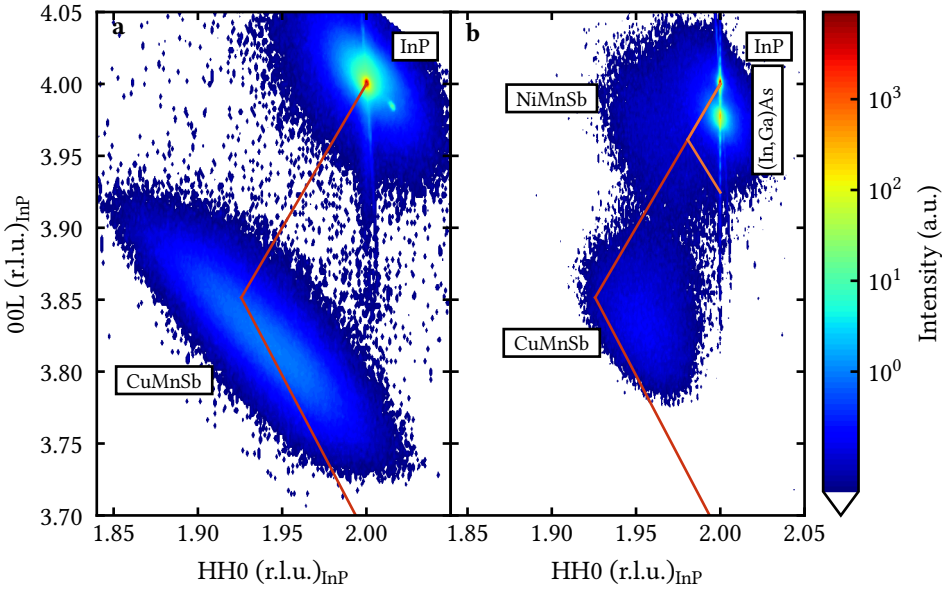
Figure 7.2: **RSM measurements of fully epitaxial CuMnSb/NiMnSb heterostructures grown on InP substrates. a** RSM of the (224) diffraction peak of a 40 nm thick CuMnSb single layer grown on InP as a reference ❧H1314 . The relaxation triangle of CuMnSb is drawn in red. **b** RSM of the (224) diffraction peak of a CuMnSb/NiMnSb heterostructure grown on InP ❧H1316 . The thickness of the CuMnSb layer is 20 nm and the thickness of the NiMnSb layer is 5 nm. Relaxation triangles are drawn for both CuMnSb (red) and NiMnSb (orange).

intermediate between those of CuMnSb and NiMnSb, however, InAs is less suitable for electrical transport experiments due to its high conductivity. Nevertheless, the RHEED and HRXRD studies show that fully epitaxial heterostructures from CuMnSb and NiMnSb can be fabricated on InP substrates. Further investigation of these heterostructures is therefore worthwhile.

SIMS measurements are used to further investigate the layer sequence of the fabricated CuMnSb/NiMnSb heterostructures. A general introduction to SIMS can be found in [116]. The SIMS measurements were performed by Margit Wagenbrenner at the department of Technische Physik of the Julius-Maximilians-Universität Würzburg. SIMS spectra of the sample with 20 nm CuMnSb and 5 nm NiMnSb are taken both in positive ion mode using O_2 ions and in negative ion mode using Cs ions for sputtering (Figure 7.3). In positive ion mode (Figure 7.3 **a**), the interface between the 5 nm thick Ru cap and the NiMnSb layer can be clearly identified by a drop in the Ru intensity and a rise in the intensities of Ni, Mn, and Sb. Contrary to expectations, however, an increase in Cu intensity can also be observed at this
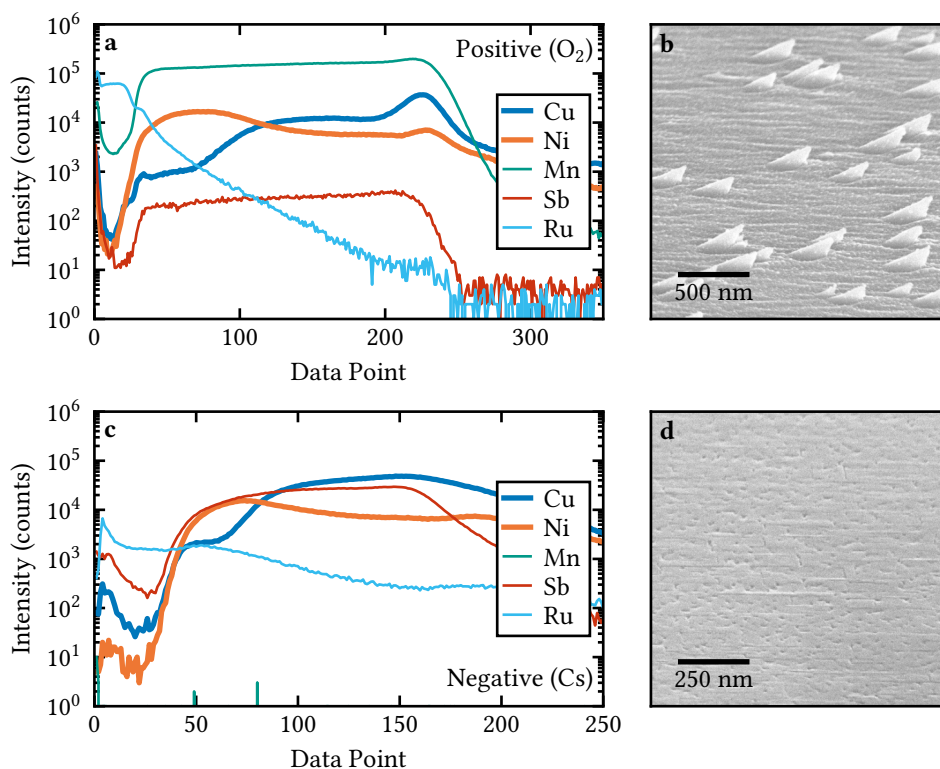
Figure 7.3: **SIMS measurements on fully epitaxial CuMnSb/NiMnSb heterostructures grown on InP substrates.** 📑 H1316 The data points are recorded according to equidistant time intervals and thus reflect the time evolution of the spectrum during the recording. **a** SIMS spectrum collected in positive ion mode using O_2 ions for sputtering. **b** Scanning electron microscope (SEM) image of the sample surface after collection of the SIMS spectrum in positive ion mode using O_2 ions for sputtering. **c** SIMS spectrum collected in negative ion mode using Cs ions for sputtering. **d** SEM image of the sample surface after collection of the SIMS spectrum in negative ion mode using Cs ions for sputtering.

point. At a certain depth, presumably close to the NiMnSb/CuMnSb interface, the Ni intensity starts to decrease and the Cu intensity starts to increase. However, this does not happen in such an abrupt way as one would expect for a sharp interface of two epitaxial layers. Furthermore, until the (In,Ga)As layer is reached, as indicated by the drop in Mn and Sb intensities, a Ni intensity continues to be measured. As can be seen from the scanning electron microscope (SEM) image of the sample surface in Figure 7.3 **b**, the collection of the SIMS spectrum in positive ion mode leaves a rough surface with pyramid-like structures, indicating that the sputtering did not occur completely uniform. This could be a possible explanation for the

absence of abrupt transitions between the individual layers and for the different positions of the signal edges of Mn and Sb. Another cause for the former could be the diffusion of individual elements between the layers, which is discussed in more detail below. The previous statements also apply to the SIMS spectrum in negative ion mode, with the exceptions that Mn produces no measurable signal and the Ru intensity drop at the NiMnSb interface cannot be observed (Figure 7.3 **c**). The SEM image of the sample surface after collection of the SIMS spectrum in negative ion mode is shown in Figure 7.3 **d**. Although there are no such pronounced structures on the surface, the surface is also characterized by roughness, which suggests a non-uniform sputtering process.

Both the increase in Cu intensity at the Ru/NiMnSb interface and the absence of a drop in Ni intensity at the NiMnSb/CuMnSb interface indicate diffusion of Ni and Cu atoms between the two half-Heusler layers. Similar interdiffusion effects have also been observed in sputtered PtMnSb/CuMnSb multilayer films [117]. This suggests that the diffusion of transition metals located on the tetrahedral interstitials of the $C1_b$ half-Heusler lattice is a general problem in heterostructures made of CuMnSb and other half-Heusler materials. The interdiffusion of Ni and Cu is a major drawback for the realization of all-(half-)Heusler junctions since this prevents a sharp interface between the two half-Heusler layers. It appears that the Ni and Cu atoms have very high mobility in the half-Heusler crystal. Since the growth temperature of 250 °C is already very low, it is unlikely that diffusion will be prevented by further lowering the substrate temperature during growth. Diffusion could be prevented by inserting a diffusion barrier, but this would eliminate the direct interface between CuMnSb and NiMnSb. In order to make CuMnSb/NiMnSb heterostructures suitable for use in future spintronic applications, it is necessary to realize diffusion prevention in future work.

7.3 MAGNETIC PROPERTIES

Epitaxial NiMnSb thin films are known to exhibit in-plane ferromagnetism with a rich magnetic in-plane anisotropy [98, 118]. Section 6.4 revealed that the exchange bias effect can be observed for in-plane ferromagnets deposited on the CuMnSb surface, therefore it is likely that the exchange bias effect can also be observed on epitaxial CuMnSb/NiMnSb heterostructures.

Before the exchange bias effect on the CuMnSb/NiMnSb heterostructures is investigated in more detail using field dependent magnetic measurements $M(H)$, temperature dependent magnetic measurements $M(T)$ of the CuMnSb single layer grown on InP are first used to verify whether it is antiferromagnetic. FCW and ZFCW $M(T)$ measurements of the CuMnSb single layer at a magnetic field of 500 mT are shown in Figure 7.4 **a**. The ZFCW measurement shows the typical behavior of antiferromagnetic CuMnSb with a cusp at the magnetic phase transition. With
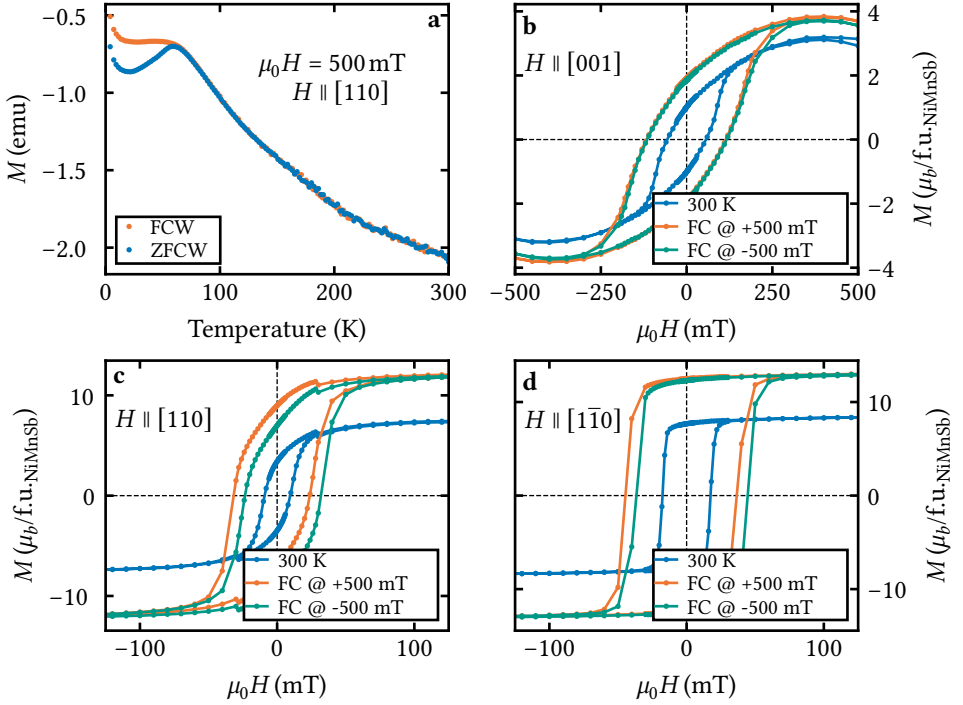
Figure 7.4: **Magnetic characterization of epitaxial CuMnSb/NiMnSb heterostructures.** The measurements are uncompensated. **a** Temperature dependent magnetization of a 40 nm tick CuMnSb single layer grown on InP along the [110] crystal direction ❦H1314. **b** Exchange bias measurements with linear background subtracted in [001] crystal direction ❦H1315. **c** Exchange bias measurements with linear background subtracted in [110] crystal direction ❦H1315. **d** Exchange bias measurements with linear background subtracted in [1\overline{1}0] crystal direction ❦H1315.

T_N=60 K, there is no difference in the magnetic transition temperature between growth on InP and growth on InAs or GaSb. In the antiferromagnetic phase a large bifurcation of the FCW and ZFCW measurements can be observed. This bifurcation leads to a vertical shift in the exchange bias measurements due to the opposing cooling fields. By subtracting the linear signal at high magnetic fields, this vertical shift is removed from the following $M(H)$ measurements.

The exchange bias effect of the CuMnSb/NiMnSb heterostructure with a CuMnSb thickness of 20 nm and a NiMnSb thickness of 5 nm is studied at 4 K for cooling fields of 500 mT and −500 mT along the crystal directions [001], [110] and [1\overline{1}0]. As a reference, M(T) is also measured at 300 K. For a detailed description of the measurement protocol, please refer to section 6.4. Figure 7.4 **b** shows the

$M(T)$ measurements along the out-of-plane crystal direction [001]. Field cooling has no effect on the $M(T)$ measurements, except for an increase in the saturation magnetization and coercive field compared to the measurement at 300 K. Both are obviously due to the temperature difference. Signs of exchange bias, such as a horizontal shift of the $M(T)$ measurements, are not observed.

The situation is different for the $M(T)$ measurements along the in-plane crystal directions [110] and [1$\bar{1}$0], which are shown in Figure 7.4 **c** and Figure 7.4 **d**, respectively. For both orientations, the saturation magnetization and the coercive field also increase as a result of cooling. As can be seen, a small horizontal shift of $M(T)$ at 4 K can be observed, which depends on the direction of the cooling field. This is an indication of the existence of the exchange bias effect at the CuMnSb/NiMnSb interface. The exchange bias field is fairly isotropic but weak. It measures 4.5 mT in [110] direction and 4.0 mT in [1$\bar{1}$0] direction.

The magnetization is plotted in units of Bohr magnetons per formula unit of NiMnSb in Figures 7.4 **b-d**. For both in-plane orientations, the saturation magnetization already significantly exceeds the 4 μ_b/f.u. expected for NiMnSb at 0 K. At 4 K, it is up to three times larger at approximately ~12 μ_b/f.u.. This deviation from the expected saturation magnetization of the NiMnSb layer is due to the diffusion of Cu and Ni atoms between the two half-Heusler layers, which was reported in section 7.2. In comparison to a pure CuMnSb crystal, a small substitution of Cu atoms by Ni atoms leads to a massive increase in the saturation magnetization in $Cu_xNi_{1-x}MnSb$ compounds [119]. If this is transferred to the CuMnSb/NiMnSb heterostructures studied here, this is indicative that the Ni-doped CuMnSb layer also makes a non-negligible contribution to the saturation magnetization. This leads to a significant increase in saturation magnetization when it is calculated solely for the NiMnSb layer.

7

8

CONCLUSIONS & OUTLOOK

In order to exploit the potential of CuMnSb as a model system in electrical transport experiments, high-quality thin films with well-defined interfaces to other materials are needed. Material growth by means of MBE is ideally suited for such requirements. In this work, a newly developed growth process for CuMnSb films using MBE and an intensive characterization of the structural, electrical, and magnetic material properties of the grown films are presented.

For the growth of epitaxial CuMnSb, InAs and GaSb were found to be suitable substrates. CuMnSb was also successfully grown on InP substrates, but, due to the high lattice mismatch, relaxation of the CuMnSb layer was observed even at low layer thicknesses. While InAs is suitable as a substrate for vertical transport applications due to its high conductivity, as demonstrated in [76], GaSb substrates are conversely suitable for lateral transport devices due to their lower conductivity. However, by inserting a non-conducting ZnTe interlayer, lateral transport experiments can also be realized on CuMnSb layers grown on InAs. Due to the lattice mismatch, this is only possible for thin CuMnSb layers. To protect the epitaxial CuMnSb layers from the environment, both sputtered Ru and Al_2O_3 caps were deemed suitable.

The use of MBE enables a new level of material quality of CuMnSb, confirmed by various characterization techniques. For example, HRXRD rocking curves show a low FWHM of only 7.7″, indicating very low mosaicity in the grown CuMnSb crystals. A high order in the CuMnSb crystal was also confirmed by STEM images. Basic transport experiments showed a residual resistance of $\rho_0 = 35\,\mu\Omega \cdot cm$, below the lowest values reported for CuMnSb [26]. This indicates a reduction of the defect concentration compared to the bulk material.

Similar to the growth of NiMnSb [20, 98, 99], a high sensitivity of the material parameters to the ratios of the material fluxes used during growth was observed for

CuMnSb MBE. Of particular note is the dependence of the vertical lattice parameter of CuMnSb on the Mn/Sb flux ratio for growth on GaSb substrates. This enables CuMnSb layers to be grown tensile strained, unstrained and compressive strained on a single substrate material. As the type of strain directly affects the space group of the CuMnSb crystal, this feature could be of particular interest for future SOT switching experiments. The good controllability of the material composition during epitaxial growth in combination with neutron diffraction experiments could be used in the future to experimentally verify the influence of point defects on the magnetic ground state of CuMnSb proposed by Máca *et al.* [36]. Furthermore, it could be shown that maximum T_N is reached at stoichiometric material composition. Therefore, it is possible that T_N can be utilized as a useful selection tool to detect stoichiometric composition of CuMnSb.

The magnetic behavior of CuMnSb was found to be consistent with that of bulk material. However, the epitaxial CuMnSb layers show an additional complex magnetic phase which is likely localized at the CuMnSb surface. This signal is particularly measurable in thin films, due to the increased surface to volume ratio. In thicker epitaxial CuMnSb layers, this signal is only observable at low magnetic fields. The additional magnetic phase behaves nonlinearly in the magnetic field and is reflected by a second temperature regime with Curie-Weiss behavior in temperature dependent measurements. Both superparamagnetic and spin-glass-like behavior can be assigned to the additional magnetic phase. Based on the available evidence, it seems most likely that this signal is generated by uncompensated moments on the CuMnSb surface. In conclusion, however, this hypothesis can only be tested by intensive investigation of the surface magnetization, e.g., by using spin-polarized scanning tunneling microscopy. Furthermore, investigations on bulk CuMnSb have to be performed to determine whether this additional magnetic phase is exclusive to epitaxial CuMnSb or an intrinsic property of CuMnSb.

The major challenges on the way to the use of epitaxial CuMnSb in novel spintronic device applications remain the proof that SOT switching experiments with CuMnSb are possible and the fabrication of fully epitaxial NiMnSb/CuMnSb heterostructures. For the latter, the first attempts were presented in this work. It was found that the interdiffusion of Cu and Ni between CuMnSb and NiMnSb is a major difficulty in the realization of high-quality interfaces between these materials. Future studies will have to show whether this diffusion can be prevented by technical methods such as growing at very low temperatures. The switching of the Néel vector of epitaxial CuMnSb, fabricated during this work, using current pulses has already been investigated in the work of Julian Werther [68]. Switching could not be observed so far. Further development steps are therefore also necessary at this point, possibly through the combination of CuMnSb with other materials.

A

MBEᴘʏ

At the beginning of this work, various programs were used to control the MBE chambers of the UHV cluster. Some of them were rudimentary command line programs without a graphical user interface, which only allowed the control of the cell and substrate temperatures, as well as the control of the cell shutters. Monitoring of various chamber metrics was not possible, nor was the execution of complex growth programs. To change these circumstances I developed a new control software for MBE chambers during this work, called MBEᴘʏ. MBEᴘʏ was developed with the goal of creating a universal, platform independent, remote controllable, and extensible control software for MBE chambers.

Based on the programming languages Pʏᴛʜᴏɴ, JᴀᴠᴀSᴄʀɪᴘᴛ, HTML and CSS, MBEᴘʏ is a client/server application. The server application runs on the control computer, which is connected to all instruments and devices of the MBE chamber. The user interface can then be accessed locally or via the internet using a web browser.

Due to a driver-based architecture, the software can be adapted to various MBE systems. For example, to integrate a new temperature controller, only standardized functions that define the communication to the controller have to be implemented. It is likely this ease of extensibility that has led to MBEᴘʏ now being used to control almost all of the MBE chambers in the UHV cluster.

The three most important features of MBEᴘʏ for this work are monitoring chamber functions, running complex growth programs, and capturing RHEED images. Monitoring the chamber metrics serves two main purposes. First, it serves to control the growth parameters during sample growth. For this purpose, the course of temperatures and pressures are displayed in graphs, as well as an overview of the momentary values. Figure A.1 shows a screenshot of the so-called dashboard, on which all this information is merged. Secondly, it is used to monitor the chamber
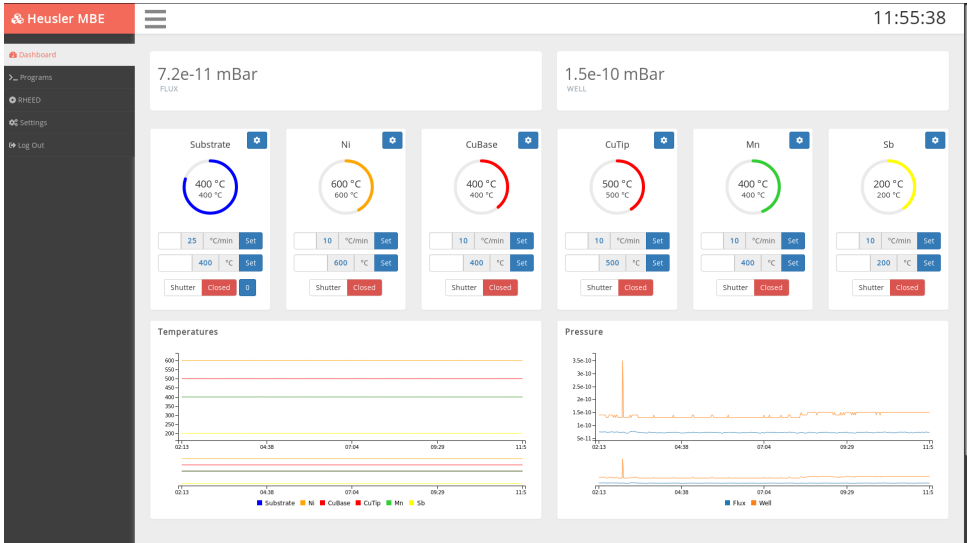
Figure A.1: **Screenshot of the MBEpy dashboard.**

while no growth is taking place. For this purpose, all measured values are written to log files to facilitate troubleshooting in case of problems. Secondly, all values are constantly checked to ensure that they are within specified tolerances. If this is not the case, warnings are sent to all users of the MBE chambers. In this way, major disasters can often be avoided by rapid reaction.

A programming language based on Python was developed for running complex growth programs. It provides simplified commands for MBE typical commands like opening and closing shutters or setting a temperature. However, all language elements of Python can be used, which allows for example the execution of loops and the checking of conditions. Basically, there is no restriction on the functionality of the growth programs. The programs can be created, edited, and started in the MBEpy user interface.

Example A.1 shows as an example program used in this work for the growth of CuMnSb, which is structured as follows: Lines 1–10 define the key parameters for the growth. The variables `sample_name`, `buffer_number`, `comments` and `layerstack` are mainly used for documentation. With this information, a new directory is automatically created by the command `createHeuslerSample(...)` in lines 16–18 for each sample in the folder structure of the institute, in which all important information about the growth is automatically stored. In addition to the information defined in the program, the cell temperatures for the respective sample are stored there as well. The variables `growth_time` and `delay` define the growth time for the CuMnSb layer and how long the cell shutter should be open before the CuMnSb

growth is initiated by opening the main shutter. The while loop in lines 12 and 13 ensures that the substrate temperature has reached its setpoint before any other commands are executed. As already mentioned, growth documentation is largely automated by MBEᴘʏ. This also includes that all metrics of the chamber during growth are saved in a separate file. The start of this recording is triggered by the command `startMeasurement(...)` in line 15.

Example A.1: Growth program used for CuMnSb growth with MBEᴘʏ.

```
1  sample_name = "Hxxx"
2  growth_time = 80 * 60
3  cooldown = True
4  delay = 5
5  buffer_number = "C21.1-xxxx"
6  comments = {"purpose": "CuMnSb␣Growth"}
7  layerstack = [{"material": "GaSb:lowTe", "height": "Substrate"},
8                {"material": "GaSb", "height": "150␣nm"},
9                {"material": "CuMnSb", "height": "40␣nm"},
10               {"material": "Ru", "height": "5␣nm"}]
11
12 while getTemp("Substrate") < 250:
13     wait(1)
14
15 startMeasurement(sample_name)
16 createHeuslerSample(sample_name, growth_time,
17                     buffer_number, comments,
18                     layerstack)
19 image_positions = [{"tag": "1-10", "angle": 0},
20                    {"tag": "010", "angle": 45},
21                    {"tag": "110", "angle": 90},
22                    {"tag": "100", "angle": 135}]
23 offset = -delay
24 collectImages(1, image_positions, offset, hdr=[2,1])
25 close("Substrate")
26 open("CuBase","Mn","Sb")
27 wait(delay*60)
28 open("Substrate")
29 wait(growth_time)
30 close("Substrate", "CuBase","Mn","Sb")
31 stopMotor()
32 stopMeasurement()
33 setTemp("Substrate", 200)
34 if cooldown:
35     setTemp("CuBase", 400)
36     setTemp("CuTip", 500)
37     setTemp("Mn", 400)
38     setTemp("Sb", 200)
```

As can be seen in line 24 of the example program, the RHEED recordings are started by the command `collectImages(...)`. These recordings are also controlled and processed by MBEᴘʏ. Thus, the control computer is connected to both a stepper motor and a CCD camera. Before growth, the sample must be aligned along a crystal direction defined in the program in a separate window of the user interface. For

A

this purpose, arrows are available for moving the motor, as well as a video stream of the camera. Through this calibration, MBEpy knows the current orientation of the sample and can approach all further orientations in relation to the first set crystal direction. The orientations for which the recordings are to be made are defined in lines 19–22. A further feature concerning RHEED recordings is the recording of high dynamic range images. For this purpose, several RHEED images with different exposure times are taken for one crystal direction. By stitching these images together, the dynamic range of the RHEED images can be increased enormously.

The actual growth process is executed by the commands, which are self-explanatory, in lines 25–30. When growth is complete, the chamber is returned to standby mode in lines 31–38. If desired, the cells are cooled down to their standby temperatures.

MBEpy is constantly being further developed and adapted to other MBE systems. The complete source code with instructions and documentation can be found on the GitLab server of EP3 at `https://gitlabep3.physik.uni-wuerzburg.de/lus66ad/MBEpy`.

B

B

LIST OF SAMPLES

Sample	Substrate	Epitaxial layers	Sputtered layers
C21.1-1624	InP:Fe	(In,Ga)As (~150 nm)	
C21.1-1906	InAs:un	InAs (~150 nm)	
C21.1-1990	GaSb:un	GaSb (~150 nm)	
C21.1-2045	GaSb:un	GaSb (~150 nm)	
H1126	InP:Fe	(In,Ga)As (~150 nm) / NiMnSb (40 nm)	Ru (2 nm)
H1127	InAs:un	InAs (~150 nm) / CuMnSb (8 nm)	Ru (2 nm)
H1128	InP:Fe	(In,Ga)As (~150 nm) / NiMnSb (40 nm)	Ru (2 nm)
H1129	InP:Fe	(In,Ga)As (~150 nm) / NiMnSb (40 nm)	Ru (2 nm)
H1130	InP:Fe	(In,Ga)As (~150 nm) / NiMnSb (40 nm)	
H1131	InP:Fe	(In,Ga)As (~150 nm) / NiMnSb (40 nm)	
H1132	InP:Fe	(In,Ga)As (~150 nm) / NiMnSb (40 nm)	
H1133	InP:Fe	(In,Ga)As (~150 nm) / NiMnSb (40 nm)	
H1134	InP:Fe	(In,Ga)As (~150 nm) / NiMnSb (6 nm)	
H1135	InP:Fe	(In,Ga)As (~150 nm) / NiMnSb (40 nm)	Ru (2 nm)
H1136	InP:Fe	(In,Ga)As (~150 nm) / NiMnSb (40 nm)	Ru (2 nm)
H1137	InP:Fe	(In,Ga)As (~150 nm) / NiMnSb (40 nm)	Ru (2 nm)
H1138	InP:Fe	(In,Ga)As (~150 nm) / NiMnSb (40 nm)	Ru (2 nm)
H1139	InP:Fe	(In,Ga)As (~150 nm) / NiMnSb (40 nm)	Ru (2 nm)
H1140	InP:Fe	(In,Ga)As (~150 nm) / NiMnSb (40 nm)	Ru (2 nm)
H1141	InP:Fe	(In,Ga)As (~150 nm) / NiMnSb (40 nm)	Ru (2 nm)
H1142	InP:Fe	(In,Ga)As (~150 nm) / NiMnSb (40 nm)	Ru (2 nm)
H1143	InP:Fe	(In,Ga)As (~150 nm) / NiMnSb (40 nm)	Ru (2 nm)
H1144	InP:Fe	(In,Ga)As (~150 nm) / NiMnSb (40 nm)	Ru (10 nm)
H1145	InP:Fe	(In,Ga)As (~150 nm) / NiMnSb (30 nm)	
H1146	InP:Fe	(In,Ga)As (~150 nm) / NiMnSb (40 nm)	
H1147	InP:Fe	(In,Ga)As (~150 nm) / NiMnSb (40 nm)	
H1148	InAs:un	InAs (~150 nm) / CuMnSb (39 nm)	
H1149	InP:Fe	(In,Ga)As (~150 nm) / NiMnSb (40 nm)	
H1150	InAs:un	InAs (~150 nm) / CuMnSb (39 nm)	Ru (5 nm)
H1151	InAs:un	InAs (~150 nm) / CuMnSb (39 nm)	Ru (5 nm)
H1152	InAs:un	InAs (~150 nm) / CuMnSb (39 nm)	Ru (5 nm)
H1153	InAs:un	InAs (~150 nm) / CuMnSb (39 nm)	Ru (5 nm)
H1154	InAs:un	InAs (~150 nm) / ZnTe (70 nm) / CuMnSb (40 nm)	
H1155	InAs:un	InAs (~150 nm) / ZnTe (70 nm) / CuMnSb (40 nm)	Ru (5 nm)
H1156	InAs:un	InAs (~150 nm) / ZnTe (70 nm) / CuMnSb (40 nm)	Ru (5 nm)
H1157	InAs:un	InAs (~150 nm) / CuMnSb (39 nm)	Ru (5 nm)
H1158	InAs:un	InAs (~150 nm) / CuMnSb (39 nm)	Ru (5 nm)
H1159	InAs:un	InAs (~150 nm) / CuMnSb (39 nm)	Ru (5 nm)
H1160	InAs:un	InAs (~150 nm) / CuMnSb (39 nm)	Ru (5 nm)
H1161	InAs:un	InAs (~150 nm) / CuMnSb (39 nm)	Ru (5 nm)
H1162	InAs:un	InAs (~150 nm) / CuMnSb (39 nm)	Ru (5 nm)
H1163	InAs:un	InAs (~150 nm) / ZnTe (20 nm) / CuMnSb (30 nm)	Ru (5 nm)
H1164	InAs:un	InAs (~150 nm) / ZnTe (300 nm) / CuMnSb (40 nm)	Ru (5 nm)
H1165	InAs:un	InAs (~150 nm) / CuMnSb (39 nm)	Ru (5 nm)
H1166	InAs:un	InAs (~150 nm) / CuMnSb (39 nm)	Ru (5 nm)
H1167	InAs:un	InAs (~150 nm) / CuMnSb (39 nm)	
H1168	InAs:un	InAs (~150 nm) / CuMnSb (27 nm)	

B

Sample	Substrate	Epitaxial layers	Sputtered layers
H1169	InAs:un	InAs (~150 nm) / CuMnSb (39 nm)	Ru (5 nm)
H1170	InAs:un	InAs (~150 nm) / CuMnSb (39 nm)	Ru (5 nm)
H1171	InAs:un	InAs (~150 nm) / CuMnSb (39 nm)	Ru (5 nm)
H1172	InAs:un	InAs (~150 nm) / CuMnSb (39 nm)	
H1173	InAs:un	InAs (~150 nm) / CuMnSb (39 nm)	Ru (5 nm)
H1174	InAs:un	InAs (~150 nm) / CuMnSb (39 nm)	Ru (5 nm)
H1175	InAs:un	InAs (~150 nm) / CuMnSb (39 nm)	Ru (5 nm)
H1176	InAs:un	InAs (~150 nm) / CuMnSb (39 nm)	Ru (5 nm)
H1177	InAs:un	InAs (~150 nm) / CuMnSb (33 nm)	Ru (5 nm)
H1178	InAs:un	InAs (~150 nm) / CuMnSb (10 nm)	
H1179	InAs:un	InAs (~150 nm) / CuMnSb (10 nm)	
H1180	InAs:un	InAs (~150 nm) / CuMnSb (22 nm)	
H1181	InAs:un	InAs (~150 nm) / CuMnSb (39 nm)	Ru (5 nm)
H1182	InAs:un	InAs (~150 nm) / CuMnSb (10 nm)	
H1183	InAs:un	InAs (~150 nm) / CuMnSb (20 nm)	
H1184	InAs:un	InAs (~150 nm) / CuMnSb (9 nm)	
H1185	InAs:un	InAs (~150 nm) / CuMnSb (39 nm)	Ru (5 nm)
H1186	InAs:un	InAs (~150 nm) / CuMnSb (39 nm)	
H1187	InAs:un	InAs (~150 nm) / CuMnSb (39 nm)	
H1188	InAs:un	InAs (~150 nm) / CuMnSb (39 nm)	
H1189	InAs:un	InAs (~150 nm) / CuMnSb (39 nm)	
H1190	InAs:un	InAs (~150 nm) / CuMnSb (39 nm)	
H1191	InAs:un	InAs (~150 nm) / CuMnSb (39 nm)	
H1192	InAs:un	InAs (~150 nm) / CuMnSb (39 nm)	
H1193	InAs:un	InAs (~150 nm) / CuMnSb (39 nm)	
H1194	InAs:un	InAs (~150 nm) / CuMnSb (39 nm)	
H1195	InAs:un	InAs (~150 nm) / CuMnSb (39 nm)	
H1196	InAs:un	InAs (~150 nm) / CuMnSb (39 nm)	
H1197	InAs:un	InAs (~150 nm) / CuMnSb (39 nm)	
H1198	InAs:un	InAs (~150 nm) / CuMnSb (39 nm)	
H1199	InAs:un	InAs (~150 nm) / CuMnSb (39 nm)	
H1200	InAs:Zn	InAs (~150 nm) / CuMnSb (39 nm)	
H1201	InAs:un	InAs (~150 nm) / CuMnSb (37 nm)	Ru (5 nm)
H1202	InAs:un	InAs (~150 nm) / CuMnSb (37 nm)	Ru (5 nm)
H1203	InAs:un	InAs (~150 nm) / CuMnSb (37 nm)	Ru (5 nm)
H1204	InAs:un	InAs (~150 nm) / CuMnSb (37 nm)	
H1205	InAs:un	InAs (~150 nm) / CuMnSb (37 nm)	Ru (5 nm)
H1206	InAs:un	InAs (~150 nm) / CuMnSb (37 nm)	
H1207	InAs:un	InAs (~150 nm) / CuMnSb (37 nm)	Ru (5 nm)
H1208	InAs:un	InAs (~150 nm) / CuMnSb (37 nm)	
H1209	InAs:un	InAs (~150 nm) / CuMnSb (37 nm)	
H1210	InAs:un	InAs (~150 nm) / CuMnSb (37 nm)	Ru (5 nm)
H1211	InAs:un	InAs (~150 nm) / CuMnSb (37 nm)	
H1212	InAs:un	InAs (~150 nm) / CuMnSb (37 nm)	Ru (5 nm)
H1213	InAs:un	InAs (~150 nm) / CuMnSb (37 nm)	
H1214	InAs:un	InAs (~150 nm) / CuMnSb (37 nm)	Ru (5 nm)
H1215	InAs:un	InAs (~150 nm) / CuMnSb (37 nm)	Ru (5 nm)
H1216	InAs:un	InAs (~150 nm) / CuMnSb (37 nm)	Ru (5 nm)
H1217	InAs:un	InAs (~150 nm) / CuMnSb (37 nm)	Ru (5 nm)
H1218	InAs:un	InAs (~150 nm) / CuMnSb (37 nm) / ZnTe (20 nm)	
H1219	InAs:un	InAs (~150 nm) / CuMnSb (37 nm)	
H1220	InAs:un	InAs (~150 nm) / CuMnSb (37 nm)	Ru (5 nm)
H1221	InAs:un	InAs (~150 nm) / ZnTe (20 nm) / CuMnSb (15 nm)	Ru (5 nm)
H1222	InAs:un	InAs (~150 nm) / CuMnSb (10 nm) / ZnTe (20 nm)	
H1223	InAs:un	InAs (~150 nm) / CuMnSb (37 nm)	NiFe (10 nm) / Ta (5 nm) / Ru (5 nm)
H1224	InAs:un	InAs (~150 nm) / CuMnSb (15 nm)	
H1225	InAs:un	InAs (~150 nm) / CuMnSb (37 nm)	NiFe (10 nm) / Ta (5 nm) / Ru (5 nm)
H1226	InAs:un	InAs (~150 nm) / CuMnSb (37 nm)	Ru (5 nm)
H1227	GaSb:un	GaSb (~150 nm) / CuMnSb (37 nm)	Ru (5 nm)
H1228	InAs:un	InAs (~150 nm) / CuMnSb (15 nm) / ZnTe (70 nm)	
H1229	InAs:un	InAs (~150 nm) / CuMnSb (15 nm) / ZnTe (70 nm)	
H1230	InAs:un	InAs (~150 nm) / CuMnSb (15 nm) / ZnTe (70 nm)	
H1231	InAs:un	InAs (~150 nm) / CuMnSb (15 nm) / ZnTe (70 nm)	
H1232	GaSb:un	GaSb (~150 nm) / CuMnSb (270 nm)	Ru (5 nm)
H1233	InAs:un	InAs (~150 nm) / CuMnSb (15 nm) / ZnTe (70 nm)	
H1234	InAs:un	InAs (~150 nm) / CuMnSb (15 nm) / ZnTe (70 nm)	
H1235	InAs:un	InAs (~150 nm) / CuMnSb (15 nm) / ZnTe (70 nm)	
H1236	InAs:un	InAs (~150 nm) / CuMnSb (15 nm) / ZnTe (70 nm)	
H1237	InAs:un	InAs (~150 nm) / CuMnSb (37 nm)	MgO (5 nm)
H1238	GaSb:Zn	GaSb (~150 nm) / CuMnSb (37 nm)	MgO (5 nm)
H1239	GaSb:un	GaSb (~150 nm) / CuMnSb (37 nm)	MgO (5 nm)
H1240	GaSb:un	GaSb (~150 nm) / CuMnSb (37 nm)	
H1241	InAs:un	InAs (~150 nm) / CuMnSb (15 nm) / ZnTe (25 nm)	
H1242	InAs:un	InAs (~150 nm) / ZnTe (30 nm) / CuMnSb (40 nm)	Ru (5 nm)
H1243	GaSb:un	GaSb (~150 nm) / CuMnSb (5 nm)	Ru (5 nm)
H1244	GaSb:un	GaSb (~150 nm) / CuMnSb (40 nm)	Ru (5 nm)

Sample	Substrate	Epitaxial layers	Sputtered layers
H1245	GaSb:un	GaSb (~150 nm) / CuMnSb (40 nm)	Ru (5 nm)
H1246	GaSb:un	GaSb (~150 nm) / CuMnSb (40 nm)	Ru (5 nm)
H1247	GaSb:un	GaSb (~150 nm) / CuMnSb (40 nm)	Ru (5 nm)
H1248	GaSb:un	GaSb (~150 nm) / CuMnSb (40 nm)	Ru (5 nm)
H1249	GaSb:un	GaSb (~150 nm) / CuMnSb (20 nm)	Ru (5 nm)
H1250	GaSb:un	GaSb (~150 nm) / CuMnSb (5 nm)	Ru (5 nm)
H1251	GaSb:un	GaSb (~150 nm) / CuMnSb (10 nm)	Ru (5 nm)
H1252	InAs:un	InAs (~150 nm) / ZnTe (30 nm) / CuMnSb (30 nm)	Ru (5 nm)
H1253	InAs:un	InAs (~150 nm) / ZnTe (20 nm) / CuMnSb (20 nm)	Ru (5 nm)
H1254	InAs:un	InAs (~150 nm) / CuMnSb (40 nm)	Ru (5 nm)
H1255	InAs:un	InAs (~150 nm) / CuMnSb (40 nm)	Ru (5 nm)
H1256	InAs:un	InAs (~150 nm) / CuMnSb (40 nm)	Ru (5 nm)
H1257	InAs:un	InAs (~150 nm) / CuMnSb (40 nm)	Ru (5 nm)
H1258	InAs:un	InAs (~150 nm) / CuMnSb (40 nm)	Ru (5 nm)
H1259	InAs:un	InAs (~150 nm) / CuMnSb (40 nm)	Ru (5 nm)
H1260	InAs:un	InAs (~150 nm) / CuMnSb (40 nm)	Ru (5 nm)
H1261	InAs:un	InAs (~150 nm) / CuMnSb (40 nm)	Ru (5 nm)
H1262	InAs:un	InAs (~150 nm) / CuMnSb (40 nm)	Ru (5 nm)
H1263	InAs:un	InAs (~150 nm) / CuMnSb (40 nm)	
H1264	GaSb:un	GaSb (~150 nm) / CuMnSb (40 nm)	Ru (5 nm)
H1265	GaSb:un	GaSb (~150 nm) / CuMnSb (510 nm)	Ru (5 nm)
H1266	InAs:un	InAs (~150 nm) / CuMnSb (40 nm)	
H1267	InAs:un	InAs (~150 nm) / CuMnSb (40 nm)	
H1268	InAs:un	InAs (~150 nm) / CuMnSb (5 nm)	Ru (5 nm)
H1269	GaSb:lowTe	GaSb (~150 nm) / CuMnSb (40 nm)	Ru (5 nm)
H1270	GaSb:lowTe	GaSb (~150 nm) / CuMnSb (40 nm)	Ru (5 nm)
H1271	GaSb:lowTe	GaSb (~150 nm) / CuMnSb (40 nm)	Ru (5 nm)
H1272	GaSb:lowTe	GaSb (~150 nm) / CuMnSb (40 nm)	Ru (5 nm)
H1273	GaSb:lowTe	GaSb (~150 nm) / CuMnSb (40 nm)	Ru (5 nm)
H1274	GaSb:lowTe	GaSb (~150 nm) / CuMnSb (40 nm)	Ru (5 nm)
H1275	GaSb:lowTe	GaSb (~150 nm) / CuMnSb (40 nm)	Ru (5 nm)
H1276	GaSb:lowTe	GaSb (~150 nm) / CuMnSb (40 nm)	Ru (5 nm)
H1277	GaSb:lowTe	GaSb (~150 nm) / CuMnSb (40 nm)	Ru (5 nm)
H1278	InAs:un	InAs (~150 nm) / CuMnSb (40 nm)	Ru (5 nm)
H1279	InAs:un	InAs (~150 nm) / CuMnSb (40 nm)	
H1280	InAs:un	InAs (~150 nm) / CuMnSb (40 nm)	
H1281	InAs:un	InAs (~150 nm) / CuMnSb (40 nm)	
H1282	InAs:un	InAs (~150 nm) / CuMnSb (40 nm)	
H1283	InAs:un	InAs (~150 nm) / CuMnSb (40 nm)	Al_2O_3 (1.3 nm)
H1284	InAs:un	InAs (~150 nm) / CuMnSb (40 nm)	
H1285	InAs:un	InAs (~150 nm) / CuMnSb (40 nm)	
H1286	GaSb:un	GaSb (~150 nm) / CuMnSb (40 nm)	Ru (5 nm)
H1287	GaSb:highTe	GaSb (~150 nm) / CuMnSb (40 nm)	Ru (5 nm)
H1288	InAs:un	InAs (~150 nm) / CuMnSb (40 nm)	Al_2O_3 (2.7 nm)
H1289	InAs:un	InAs (~150 nm) / CuMnSb (40 nm)	Al_2O_3 (1.8 nm)
H1290	GaSb:lowTe	GaSb (~150 nm) / CuMnSb (40 nm)	Ru (5 nm)
H1291	GaSb:lowTe	GaSb (~150 nm) / CuMnSb (40 nm)	Ru (5 nm)
H1292	GaSb:lowTe	GaSb (~150 nm) / CuMnSb (40 nm)	Ru (5 nm)
H1293	GaSb:lowTe	GaSb (~150 nm) / CuMnSb (40 nm)	Ru (5 nm)
H1294	GaSb:lowTe	GaSb (~150 nm) / CuMnSb (40 nm)	Ru (5 nm)
H1295	GaSb:lowTe	GaSb (~150 nm) / CuMnSb (5 nm)	Al_2O_3 (2.5 nm)
H1296	GaSb:lowTe	GaSb (~150 nm) / CuMnSb (10 nm)	Al_2O_3 (2.5 nm)
H1297	GaSb:lowTe	GaSb (~150 nm) / CuMnSb (40 nm)	Al_2O_3 (2.5 nm)
H1298	GaSb:lowTe	GaSb (~150 nm) / CuMnSb (40 nm)	Ru (5 nm)
H1299	InAs:un	InAs (~150 nm) / CuMnSb (40 nm)	Ru (5 nm)
H1300	GaSb:lowTe	GaSb (~150 nm) / CuMnSb (210 nm)	Al_2O_3 (2.5 nm)
H1301	GaSb:lowTe	GaSb (~150 nm) / CuMnSb (40 nm)	NiFe (3 nm) / Ta (5 nm) / Ru (5 nm)
H1302	GaSb:un	GaSb (~150 nm) / CuMnSb (40 nm)	Co (3 nm) / Ta (5 nm) / Ru (5 nm)
H1303	GaSb:lowTe	GaSb (~150 nm) / CuMnSb (40 nm)	CoFe (3 nm) / Ta (5 nm) / Ru (5 nm)
H1304	GaSb:lowTe	GaSb (~150 nm) / CuMnSb (40 nm)	Ru (5 nm)
H1305	GaSb:lowTe	GaSb (~150 nm) / CuMnSb (40 nm)	Ru (5 nm)
H1306	InAs:un	InAs (~150 nm) / CuMnSb (40 nm)	Al_2O_3 (2.3 nm)
H1307	InAs:un	InAs (~150 nm) / CuMnSb (40 nm)	Al_2O_3 (2.3 nm)
H1308	InAs:un	InAs (~150 nm) / CuMnSb (40 nm)	Al_2O_3 (2.3 nm)
H1309	InAs:un	InAs (~150 nm) / CuMnSb (40 nm)	Al_2O_3 (2.3 nm)
H1310	InAs:un	InAs (~150 nm) / CuMnSb (60 nm)	Ru (5 nm)
H1311	InAs:un	InAs (~150 nm) / CuMnSb (60 nm)	
H1312	GaSb:lowTe	GaSb (~150 nm) / CuMnSb (10 nm)	Ru (5 nm)
H1313	InP:Fe	(In,Ga)As (~150 nm) / CuMnSb (10 nm)	Ru (5 nm)
H1314	InP:Fe	(In,Ga)As (~150 nm) / CuMnSb (40 nm)	Ru (5 nm)
H1315	InP:Fe	(In,Ga)As (~150 nm) / CuMnSb (20 nm) / NiMnSb (5 nm)	Ru (5 nm)
H1316	InP:Fe	(In,Ga)As (~150 nm) / CuMnSb (20 nm) / NiMnSb (7.5 nm)	Ru (5 nm)
H1317	InAs:un	InAs (~150 nm) / CuMnSb (40 nm)	Ru (5 nm)
H1318	InAs:un	InAs (~150 nm) / CuMnSb (40 nm)	Ru (5 nm)
H1319	InAs:un	InAs (~150 nm) / CuMnSb (40 nm)	
H1320	InAs:un	InAs (~150 nm) / CuMnSb (40 nm)	Ru (5 nm)

B

Sample	Substrate	Epitaxial layers	Sputtered layers
H1321	InAs:un	InAs (~150 nm) / CuMnSb (40 nm)	Ru (5 nm)
H1322	InAs:un	InAs (~150 nm) / CuMnSb (40 nm)	Ru (5 nm)
H1323	InAs:un	InAs (~150 nm) / CuMnSb (40 nm)	Ru (5 nm)
H1324	InAs:un	InAs (~150 nm) / CuMnSb (40 nm)	Ru (5 nm)
H1325	InAs:un	InAs (~150 nm) / CuMnSb (40 nm)	Ru (5 nm)
H1326	InAs:un	InAs (~150 nm) / CuMnSb (40 nm)	Ru (5 nm)
H1327	InAs:un	InAs (~150 nm) / CuMnSb (40 nm)	Ru (5 nm)
H1328	GaSb:lowTe	GaSb (~150 nm) / CuMnSb (40 nm)	Ru (5 nm)
H1329	GaSb:lowTe	GaSb (~150 nm) / CuMnSb (40 nm)	Ru (5 nm)
H1330	GaSb:un	GaSb (~150 nm) / CuMnSb (40 nm)	Ru (5 nm)
H1331	GaSb:lowTe	GaSb (~150 nm) / CuMnSb (40 nm) / Sb (10 nm)	
H1332	InAs:un	InAs (~150 nm) / CuMnSb (40 nm)	Ru (5 nm)
H1333	InAs:un	InAs (~150 nm) / CuMnSb (40 nm)	Ru (5 nm)
H1334	GaSb:lowTe	GaSb (~150 nm) / CuMnSb (40 nm)	
H1335	GaSb:lowTe	GaSb (~150 nm) / CuMnSb (40 nm)	Ru (5 nm)
H1336	GaSb:lowTe	GaSb (~150 nm) / CuMnSb (40 nm)	
H1337	GaSb:lowTe	GaSb (~150 nm) / CuMnSb (40 nm)	
H1338	GaSb:lowTe	GaSb (~150 nm) / CuMnSb (40 nm)	
H1339	GaSb:lowTe	GaSb (~150 nm) / CuMnSb (40 nm)	Ru (5 nm)
H1340	GaSb:lowTe	GaSb (~150 nm) / CuMnSb (40 nm)	Ru (5 nm)
H1341	GaSb:lowTe	GaSb (~150 nm) / CuMnSb (40 nm)	Ru (5 nm)
H1342	GaSb:lowTe	GaSb (~150 nm) / CuMnSb (40 nm)	Ru (5 nm)
H1343	GaSb:lowTe	GaSb (~150 nm) / CuMnSb (40 nm)	Ru (5 nm)
H1344	GaSb:lowTe	GaSb (~150 nm) / CuMnSb (40 nm)	Ru (5 nm)
H1345	GaSb:lowTe	GaSb (~150 nm) / CuMnSb (40 nm)	Ru (5 nm)
H1346	GaSb:lowTe	GaSb (~150 nm) / CuMnSb (40 nm) / Sb (10 nm)	
H1347	GaSb:lowTe	GaSb (~150 nm) / CuMnSb (40 nm)	Ru (5 nm)
H1348	GaSb:lowTe	GaSb (~150 nm) / CuMnSb (40 nm)	Ru (5 nm)
H1349	GaSb:lowTe	GaSb (~150 nm) / CuMnSb (40 nm)	Ru (5 nm)
H1350	GaSb:lowTe	GaSb (~150 nm) / CuMnSb (40 nm)	Ru (5 nm)
H1351	GaSb:lowTe	GaSb (~150 nm) / CuMnSb (40 nm)	Ru (5 nm)
H1352	GaSb:lowTe	GaSb (~150 nm) / CuMnSb (40 nm)	Ru (5 nm)
H1353	GaSb:lowTe	GaSb (~150 nm) / CuMnSb (40 nm)	Ru (5 nm)
H1354	GaSb:lowTe	GaSb (~150 nm) / CuMnSb (40 nm)	Ru (5 nm)
H1355	GaSb:lowTe	GaSb (~150 nm) / CuMnSb (40 nm)	Ru (5 nm)
H1356	GaSb:lowTe	GaSb (~150 nm) / CuMnSb (40 nm)	Ru (5 nm)
H1357	GaSb:lowTe	GaSb (~150 nm) / CuMnSb (40 nm)	Ru (5 nm)
H1358	InAs:un	InAs (~150 nm) / CuMnSb (40 nm)	Ru (5 nm)
H1359	InAs:un	InAs (~150 nm) / CuMnSb (40 nm)	Ru (5 nm)
H1360	InAs:un	InAs (~150 nm) / CuMnSb (40 nm)	Ru (5 nm)
H1361	GaSb:lowTe	GaSb (~150 nm) / CuMnSb (40 nm)	Ru (5 nm)
H1362	GaSb:lowTe	GaSb (~150 nm) / CuMnSb (40 nm)	Ru (5 nm)
H1363	InAs:un	InAs (~150 nm) / CuMnSb (40 nm)	Ru (5 nm)
H1364	InAs:un	InAs (~150 nm) / CuMnSb (40 nm)	Ru (5 nm)
H1365	InAs:un	InAs (~150 nm) / CuMnSb (40 nm)	Ru (5 nm)
H1366	InAs:un	InAs (~150 nm) / CuMnSb (40 nm)	Ru (5 nm)
H1367	GaSb:lowTe	GaSb (~150 nm) / CuMnSb (40 nm)	Ru (5 nm)
H1368	GaSb:lowTe	GaSb (~150 nm) / CuMnSb (40 nm)	Ru (5 nm)
H1369	GaSb:lowTe	GaSb (~150 nm) / CuMnSb (40 nm)	Ru (5 nm)
H1370	GaSb:lowTe	GaSb (~150 nm) / CuMnSb (40 nm)	Al_2O_3 (2.5 nm)
H1371	GaSb:lowTe	GaSb (~150 nm) / CuMnSb (20 nm)	Al_2O_3 (2.5 nm)
H1372	GaSb:lowTe	GaSb (~150 nm) / CuMnSb (10 nm)	Al_2O_3 (2.5 nm)
H1373	GaSb:lowTe	GaSb (~150 nm) / CuMnSb (40 nm)	Co/Pd SL (30 nm)
H1374	GaSb:lowTe	GaSb (~150 nm) / CuMnSb (10 nm)	Co/Pd SL (30 nm)
H1375	GaSb:lowTe	GaSb (~150 nm) / CuMnSb (20 nm)	Co/Pd SL (30 nm)
Y421	InAs:un	InAs (~150 nm) / ZnTe (20 nm)	

Table B.1: **List of samples.**

List of Publications

- Engineering the magnetic anisotropy axes in epitaxial half-Heusler NiMnSb by Pt and Ta capping.
  F. Gerhard, M. Baussenwein, **L. Scheffler**, J. Kleinlein, C. Gould, and L. W. Molenkamp,
  Appl. Phys. Lett. **111**, 172402 (2017).
- Molecular beam epitaxy of the half-Heusler antiferromagnet CuMnSb.
  L. Scheffler, K. Gas, S. Banik, M. Kamp, J. Knobel, H. Lin, C. Schumacher, C. Gould, M. Sawicki, J. Kleinlein, and L. W. Molenkamp,
  Phys. Rev. Materials **4**, 114402 (2020).
- Bulk-like magnetic properties in MBE-grown unstrained, antiferromagnetic CuMnSb.
  L. Scheffler, J. Werther, K. Gas, C. Schumacher, C. Gould, M. Sawicki, J. Kleinlein, and L. W. Molenkamp,
  Appl. Phys. Lett. **121**, 012401 (2022).

Acknowledgements

This work would not have been possible without the help, support, and cooperation of specific people. I would therefore like to thank all those who were involved in the making of this work. A special thanks is expressed to the following people:

- Prof. Dr. Laurens W. Molenkamp, danke ich für die Aufnahme als Doktorand an seinem Lehrstuhl für Experimentelle Physik 3.

- Meinem Betreuer, Dr. Johannes Kleinlein, danke ich für seine Unterstützung und Anleitung während des gesamten Projekts.

- Prof. Dr. Maciej Sawicki and Dr. Katarzyna Gas. Kasia, thank you so much for all the work and time you have put into this project. Mike, it is very difficult for me to find the right words to thank you, because it is almost impossible to express my gratitude in words. Without you, this work would not have been possible. Thank you for all the work and brainpower you put into this project. But I thank you much more for all that we were able to experience together. P.S.: Thanks for introducing me to the polish Apfelstrudel.

- Dr. Claus Schumacher, vielen Dank für alle fachlichen und (vorallem) alle nicht fachlichen Diskussionen, für dein offenes Ohr bei jeglicher Art von Problemen, für deien Zynismus und für deine Unterstützung. Danke, dass ich dich kennenlernen durfte!

- Dr. Felicitas Brüne, vielen Dank für die Einführung in die hohe Kunst des Heusler-Wachstums.

- Dr. Shengqiang Zhou, thank you for the RBS and PIXE measurements, as well as the interesting discussions.

- Dr. Martin Kamp, vielen Dank für STEM Aufnahmen.

- Margit Wagenbrenner, vielen Dank für die SIMS Messungen.

- Many thanks to Dr. Thomas Prokscha, Dr. Xiaojie Ni, and Maria Inès Mendes Martins for conducting and evaluating the μSR experiment.

- Einen besonderen Dank möchte ich an Carmen Bundschuh und Petra Wolf-Müller für die Probenvorbereitung sowie an Martin Zipf und Volkmar Hock für die technische Unterstützung im MBE-Labor und im Reinraum aussprechen. Vorallem möchte ich mich bei euch jedoch dafür bedanken, dass ich euch als Menschen kennenlernen durfte.

- Many thanks to all members of the Heusler group, including the students I was allowed to supervise in their work, notably Jonas Knobel, Philipp Stein, Nolan Heim, Dr. Sanjib Banik, Dr. Haicheng Lin, and Nils Plähn.

- Dr. Tobias Kiessling, vielen Dank für dein immer offenes Ohr und deine Unterstützung, vorallem auch in schwierigen Zeiten.

- I would like to thank all MBE people and participants of the MBE coffee for the great cooperation and the interesting conversations. In particular, I would like to thank Lukas Lunczer, Dr. Jan Hajer, Dr. Steffen Schreyeck, Czcibor Ciostek, Boby Chrisol Joseph, Alwyn Antony, and Lena Fürst. A special thanks also goes to Prof. Dr. Grzegorz Karczewski, for all the fruitful discussions.

- Vielen Dank an die Skifahrer und ehemaligen EP3 Kollegen Martin Baußenwein, Simon Hartinger, Johannes Baumann, Dr. Philip Leubner, Dr. David Mahler und Dr. Jonas Wiedenmann für die genialen Urlaube.

- Julian Werther und Dr. Jonas Strunz, vielen Dank, dass ich durch euch zwei neue Freunde gewinnen durfte.

- Schließlich möchte ich mich bei meinen Freunden und meiner Familie, insbesondere bei Elena und meinen Eltern, für ihre bedingungslose Unterstützung bedanken. Danke, dass ihr da seid.

Bibliography

References

[1] M. N. Baibich, J. M. Broto, A. Fert, F. N. V. Dau, F. Petroff, P. Etienne, G. Creuzet, A. Friederich, and J. Chazelas, *Giant Magnetoresistance of (001)Fe/(001)Cr Magnetic Superlattices,* Phys. Rev. Lett **61**, 2472 (1988).

[2] G. Binasch, P. Grünberg, F. Saurenbach, and W. Zinn, *Enhanced magnetoresistance in layered magnetic structures with antiferromagnetic interlayer exchange,* Phys. Rev. B **39**, 4828 (1989).

[3] T. Jungwirth, J. Sinova, A. Manchon, X. Marti, J. Wunderlich, and C. Felser, *The multiple directions of antiferromagnetic spintronics,* Nat. Phys. **14**, 200 (2018).

[4] P. Wadley, B. Howells, J. Železný, C. Andrews, V. Hills, R. P. Campion, V. Novák, K. Olejník, F. Maccherozzi, S. S. Dhesi, S. Y. Martin, T. Wagner, J. Wunderlich, F. Freimuth, Y. Mokrousov, J. Kuneš, J. S. Chauhan, M. J. Grzybowski, A. W. Rushforth, K. W. Edmonds, B. L. Gallagher, and T. Jungwirth, *Electrical switching of an antiferromagnet,* Science **351**, 587 (2016).

[5] S. Y. Bodnar, L. Šmejkal, I. Turek, T. Jungwirth, O. Gomonay, J. Sinova, A. A. Sapozhnik, H.-J. Elmers, M. Kläui, and M. Jourdan, *Writing and reading antiferromagnetic Mn_2Au by Néel spin-orbit torques and large anisotropic magnetoresistance,* Nat. Commun. **9** (2018).

[6] X. Chen, R. Zarzuela, J. Zhang, C. Song, X. Zhou, G. Shi, F. Li, H. Zhou, W. Jiang, F. Pan, and Y. Tserkovnyak, *Antidamping-Torque-Induced Switching in Biaxial Antiferromagnetic Insulators,* Phys. Rev. Lett. **120**, 207204 (2018).

[7] T. Moriyama, K. Oda, T. Ohkochi, M. Kimata, and T. Ono, *Spin torque control of antiferromagnetic moments in NiO,* Sci. Rep. **8** (2018).

[8] L. Baldrati, O. Gomonay, A. Ross, M. Filianina, R. Lebrun, R. Ramos, C. Leveille, F. Fuhrmann, T. Forrest, F. Maccherozzi, S. Valencia, F. Kronast, E. Saitoh, J. Sinova, and M. Kläui, *Mechanism of Néel Order Switching in Antiferromagnetic Thin Films Revealed by Magnetotransport and Direct Imaging,* Phys. Rev. Lett. **123**, 177201 (2019).

[9] C. Chiang, S. Huang, D. Qu, P. Wu, and C. Chien, *Absence of Evidence of Electrical Switching of the Antiferromagnetic Néel Vector,* Phys. Rev. Lett. **123**, 227203 (2019).

[10] Z. Kašpar, M. Surýnek, J. Zubáč, F. Krizek, V. Novák, R. P. Campion, M. S. Wörnle, P. Gambardella, X. Marti, P. Němec, K. W. Edmonds, S. Reimers, O. J. Amin, F. Maccherozzi, S. S. Dhesi, P. Wadley, J. Wunderlich, K. Olejník, and T. Jungwirth, *Quenching of an antiferromagnet into high resistivity states using electrical or ultrashort optical pulses,* Nat. Electron. **4**, 30 (2020).

[11] Z. Kašpar, *Quench Switching of Antiferromagnetic CuMnAs*, Ph.D. thesis, Univerzita Karlova (2021).

[12] F. Krizek, S. Reimers, Z. Kašpar, A. Marmodoro, J. Michalička, O. Man, A. Edström, O. J. Amin, K. W. Edmonds, R. P. Campion, F. Maccherozzi, S. S. Dhesi, J. Zubáč, D. Kriegner, D. Carbone, J. Železný, K. Výborný, K. Olejník, V. Novák, J. Rusz, J.-C. Idrobo, P. Wadley, and T. Jungwirth, *Atomically sharp domain walls in an antiferromagnet,* Sci. Adv. **8** (2022).

[13] P. Wadley, V. Novák, R. Campion, C. Rinaldi, X. Martí, H. Reichlová, J. Železný, J. Gazquez, M. Roldan, M. Varela, D. Khalyavin, S. Langridge, D. Kriegner, F. Máca, J. Mašek, R. Bertacco, V. Holý, A. Rushforth, K. Edmonds, B. Gallagher, C. Foxon, J. Wunderlich, and T. Jungwirth, *Tetragonal phase of epitaxial room-temperature antiferromagnet CuMnAs,* Nat. Commun. **4** (2013).

[14] N. Rinaldi-Montes, P. Gorria, D. Martínez-Blanco, A. B. Fuertes, I. Puente-Orench, L. Olivi, and J. A. Blanco, *Size effects on the Néel temperature of antiferromagnetic NiO nanoparticles,* AIP Adv. **6**, 056104 (2016).

[15] V. M. T. S. Barthem, C. V. Colin, H. Mayaffre, M.-H. Julien, and D. Givord, *Revealing the properties of Mn_2Au for antiferromagnetic spintronics,* Nat. Commun. **4** (2013).

[16] J. Železný, H. Gao, A. Manchon, F. Freimuth, Y. Mokrousov, J. Zemen, J. Mašek, J. Sinova, and T. Jungwirth, *Spin-orbit torques in locally and globally noncentrosymmetric crystals: Antiferromagnets and ferromagnets,* Phys. Rev. B **95**, 014403 (2017).

[17] D.-F. Shao, S.-H. Zhang, G. Gurung, W. Yang, and E. Tsymbal, *Nonlinear Anomalous Hall Effect for Néel Vector Detection,* Phys. Rev. Lett. **124**, 067203 (2020).

[18] P. Bach, *Growth and Characterization of NiMnSb-based Heterostructures*, Ph.D. thesis, Universität Würzburg (2006).

[19] F. Lochner, *Epitaxial growth and characterization of NiMnSb layers for novel spintronic devices*, Ph.D. thesis, Universität Würzburg (2011).

[20] F. I. V. Gerhard, *Controlling structural and magnetic properties of epitaxial NiMnSb for application in spin torque devices*, Ph.D. thesis, Universität Würzburg (2014).

[21] K. Endo, T. Ohoyama, and R. Kimura, *Antiferromagnetism of CuMnSb,* J. Phys. Soc. Japan **25**, 907 (1968).

[22] R. H. Forster, G. B. Johnston, and D. A. Wheeler, *Studies on the heusler alloys—III. The antiferro-magnetic phase in the Cu-Mn-Sb system,* J. Phys. Chem. Solids **29**, 855 (1968).

[23] K. Endo, *Magnetic Studies of $C1_b$-Compounds CuMnSb, PdMnSb and Cu_{1-x} (Ni or $Pd)_x$ MnSb,* J. Phys. Soc. Japan **29**, 643 (1970).

[24] R. B. Helmholdt, R. A. de Groot, F. M. Mueller, P. G. van Engen, and K. H. J. Buschow, *Magnetic and crystallographic properties of several $C1_b$ type Heusler compounds,* J. Magn. Magn. Mater. **43**, 249 (1984).

[25] J. Bœuf, C. Pfleiderer, and A. Faißt, *Low-temperature properties of the semi-heusler compound CuMnSb,* Phys. Rev. B. **74**, 024428 (2006).

[26] A. Regnat, A. Bauer, A. Senyshyn, M. Meven, K. Hradil, P. Jorba, K. Nemkovski, B. Pedersen, R. Georgii, S. Gottlieb-Schönmeyer, and C. Pfleiderer, *Canted antiferromagnetism in phase-pure CuMnSb,* Phys. Rev. Mater. **2**, 054413 (2018).

[27] A. Bandyopadhyay, S. K. Neogi, A. Paul, C. Meneghini, S. Bandyopadhyay, I. Dasgupta, and S. Ray, *Development of half metallicity within mixed magnetic phase of $Cu_{1-x}Co_xMnSb$ alloy,* J. Condens. Matter Phys. **30**, 205802 (2018).

[28] F. Heusler, W. Starck, and E. Haupt, *Magnetisch-chemische studien,* Verh. Dtsch. Phys. Ges **5**, 219 (1903).

[29] F. Heusler, *Über magnetische manganlegierungen,* Verh. Dtsch. Phys. Ges **5**, 219 (1903).

[30] T. Graf, C. Felser, and S. S. Parkin, *Simple rules for the understanding of Heusler compounds,* Prog. Solid State Ch. **39**, 1 (2011).

[31] L. Castelliz, *Über eine mischkristallreihe zwischen zwei terären vertretern des C1-Typs,* Monatsh. Chem. **83**, 1314 (1952).

[32] H. Nowotny and B. Glatzl, *Neue Vertreter ternärer Verbindungen mit C1-Struktur,* Monatsh. Chem. Verw. Teile. Anderer Wiss. **83**, 237 (1952).

[33] F. Máca, J. Mašek, O. Stelmakhovych, X. Martí, H. Reichlová, K. Uhlířová, P. Beran, P. Wadley, V. Novák, and T. Jungwirth, *Room-temperature antiferromagnetism in CuMnAs,* J. Magn. Magn. Mater. **324**, 1606 (2012).

[34] A. P. Ramirez, *Strongly Geometrically Frustrated Magnets,* Annu. Rev. Mater. Sci. **24**, 453 (1994).

[35] C. G. Shull, W. A. Strauser, and E. O. Wollan, *Neutron Diffraction by Paramagnetic and Antiferromagnetic Substances,* Phys. Rev. **83**, 333 (1951).

[36] F. Máca, J. Kudrnovský, V. Drchal, I. Turek, O. Stelmakhovych, P. Beran, A. Llobet, and X. Marti, *Defect-induced magnetic structure of CuMnSb,* Phys. Rev. B **94**, 094407 (2016).

[37] J. Bœuf, A. Faisst, and C. Pfleiderer, *Unconventional Antiferromagnetism of Mn_3Si and CuMnSb,* Acta Phys. Pol. Ser. B. **34**, 395 (2003).

[38] C. Pfleiderer, *Are Mn_3Si and CuMnSb antiferromagnetic half-metals?* Phys. B Condens. Matter **329-333**, 1085 (2003).

[39] W. Braun, *Applied RHEED : reflection high-energy electron diffraction during crystal growth* (Springer, Berlin New York, 1999).

[40] A. Ichimiya and P. I. Cohen, *Reflection High-Energy Electron Diffraction* (Cambridge University Press, 2010).

[41] J. Knobel, *Molecular beam epitaxy of the half-Heusler antiferromagnet CuMnSb on GaSb,* Master's thesis, Universität Würzburg (2020).

[42] B. Voigtländer, *Scanning Probe Microscopy* (Springer Berlin Heidelberg, 2015).

[43] S. Amelinckx, *Handbook of microscopy : applications in materials science, solid-state physics, and chemistry* (VCH, Weinheim New York, 1997).

[44] M. A. Herman and H. Sitter, *Molecular Beam Epitaxy* (Springer Berlin Heidelberg, 2013).

[45] N. Ashcroft and N. D. Mermin, *Solid state physics* (Holt, Rinehart and Winston, New York, 1976).

[46] B. E. Warren, *X-Ray Diffraction,* Dover Books on Physics (Dover Publications, 2012).

[47] C. Suryanarayana and M. G. Norton, *X-Ray Diffraction: A Practical Approach* (Springer US, 2013).

[48] Y. A. Burenkov, S. Y. Davydov, and S. P. Nikanorov, *Elastic properties of indium arsenide,* Fiz. tverd. tela **17**, 2183 (1975).

[49] D. N. Nichols, D. S. Rimai, and R. J. Sladek, *Elastic anharmonicity of InP: Its relationship to the high pressure transition,* Solid State Commun. **36**, 667 (1980).

[50] W. F. Boyle and R. J. Sladek, *Elastic constants and lattice anharmonicity of GaSb and GaP from ultrasonic-velocity measurements between 4.2 and 300 K,* Phys. Rev. B **11**, 2933 (1975).

[51] R. Khenata, A. Bouhemadou, M. Sahnoun, A. H. Reshak, H. Baltache, and M. Rabah, *Elastic, electronic and optical properties of ZnS, ZnSe and ZnTe under pressure,* Comput. Mater. Sci. **38**, 29 (2006).

[52] S. Palaz, H. Koc, H. Ozisik, E. Deligoz, A. Mamedov, and E. Ozbay, *Optical and magnetic properties of some XMnSb and Co$_2$YZ Compounds: ab initio calculations,* Phys. Status Solidi C **14**, 1600182 (2017).

[53] D. Kriegner, E. Wintersberger, and J. Stangl, *xrayutilities: a versatile tool for reciprocal space conversion of scattering data recorded with linear and area detectors,* J. Appl. Cryst. **46**, 1162 (2013).

[54] J. M. Hinckley and J. Singh, *Influence of substrate composition and crystallographic orientation on the band structure of pseudomorphic Si-Ge alloy films,* Phys. Rev. B **42**, 3546 (1990).

[55] R. L. Fagaly, *Superconducting quantum interference device instruments and applications,* Rev. Sci. Instrum. **77**, 101101 (2006).

[56] M. Buchner, K. Höfler, B. Henne, V. Ney, and A. Ney, *Tutorial: Basic principles, limits of detection, and pitfalls of highly sensitive SQUID magnetometry for nanomagnetism and spintronics,* J. Appl. Phys. **124**, 161101 (2018).

[57] K. Gas, J. Sadowski, and M. Sawicki, *Magnetic properties of wurtzite (Ga,Mn)As,* J. Magn. Magn. Mater. **533**, 168012 (2021).

[58] M. Sawicki, W. Stefanowicz, and A. Ney, *Sensitive SQUID magnetometry for studying nanomagnetism,* Semicond. Sci. Technol. **26**, 064006 (2011).

[59] K. Gas and M. Sawicki, *In situ compensation method for high-precision and high-sensitivity integral magnetometry,* Meas. Sci. Technol. **30**, 085003 (2019).

[60] M. Mayer, *SIMNRA User's Guide*, Max-Planck-Institut für Plasmaphysik, Max-Planck-Institut für Plasmaphysik, Garching, Germany (1997), report IPP 9/113.

[61] G. Götz and K. Gärtner, *High energy ion beam analysis of solids* (Akademie-Verlag Berlin, 1988).

[62] G. Van Rossum and F. L. Drake, *Python 3 Reference Manual* (CreateSpace, Scotts Valley, CA, 2009).

[63] C. R. Harris, K. J. Millman, S. J. van der Walt, R. Gommers, P. Virtanen, D. Cournapeau, E. Wieser, J. Taylor, S. Berg, N. J. Smith, R. Kern, M. Picus, S. Hoyer, M. H. van Kerkwijk, M. Brett, A. Haldane, J. F. del Río, M. Wiebe, P. Peterson, P. Gérard-Marchant, K. Sheppard, T. Reddy, W. Weckesser, H. Abbasi, C. Gohlke, and T. E. Oliphant, *Array programming with NumPy*, Nature **585**, 357 (2020).

[64] P. Virtanen, R. Gommers, T. E. Oliphant, M. Haberland, T. Reddy, D. Cournapeau, E. Burovski, P. Peterson, W. Weckesser, J. Bright, S. J. van der Walt, M. Brett, J. Wilson, K. J. Millman, N. Mayorov, A. R. J. Nelson, E. Jones, R. Kern, E. Larson, C. J. Carey, İ. Polat, Y. Feng, E. W. Moore, J. VanderPlas, D. Laxalde, J. Perktold, R. Cimrman, I. Henriksen, E. A. Quintero, C. R. Harris, A. M. Archibald, A. H. Ribeiro, F. Pedregosa, P. van Mulbregt, and SciPy 1.0 Contributors, *SciPy 1.0: Fundamental Algorithms for Scientific Computing in Python*, Nat. Methods **17**, 261 (2020).

[65] J. D. Hunter, *Matplotlib: A 2D graphics environment*, Comput. Sci. Eng. **9**, 90 (2007).

[66] Inkscape Project, *Inkscape*, (2020).

[67] S. van der Walt, J. L. Schönberger, J. Nunez-Iglesias, F. Boulogne, J. D. Warner, N. Yager, E. Gouillart, T. Yu, and the scikit-image contributors, *scikit-image: image processing in Python*, PeerJ **2**, e453 (2014).

[68] J. Werther, *Fabrication and characterization of lateral transport devices of epitaxial CuMnSb*, Master's thesis, Universität Würzburg (2020).

[69] H. Ye, L. Li, R. T. Hinkey, R. Q. Yang, T. D. Mishima, J. C. Keay, M. B. Santos, and M. B. Johnson, *MBE growth optimization of InAs (001) homoepitaxy*, J. Vac. Sci. Technol. **31**, 03C135 (2013).

[70] J. B. Philipp, D. Reisinger, M. Schonecke, M. Opel, A. Marx, A. Erb, L. Alff, and R. Gross, *Epitaxial growth and transport properties of Sr_2CrWO_6 thin films*, J. Appl. Phys. **93**, 6853 (2003).

[71] C. Kumpf, A. Stahl, I. Gierz, C. Schumacher, S. Mahapatra, F. Lochner, K. Brunner, G. Schmidt, L. W. Molenkamp, and E. Umbach, *Structure and relaxation effects in thin semiconducting films and quantum dots,* Phys. Status Solidi C **4**, 3150 (2007).

[72] P. Quarterman, C. Sun, J. Garcia-Barriocanal, M. DC, Y. Lv, S. Manipatruni, D. E. Nikonov, I. A. Young, P. M. Voyles, and J.-P. Wang, *Demonstration of Ru as the 4th ferromagnetic element at room temperature,* Nature Communications **9** (2018).

[73] J. W. Arblaster, *Crystallographic properties of ruthenium,* Platin. Met. Rev. **57**, 127 (2013).

[74] T. Berlijn, P. Snijders, O. Delaire, H.-D. Zhou, T. Maier, H.-B. Cao, S.-X. Chi, M. Matsuda, Y. Wang, M. Koehler, P. Kent, and H. Weitering, *Itinerant Antiferromagnetism in RuO$_2$,* Phys. Rev. Lett. **118**, 077201 (2017).

[75] B. Herd, M. Knapp, and H. Over, *Atomic Scale Insights into the Initial Oxidation of Ru(0001) Using Molecular Oxygen: A Scanning Tunneling Microscopy Study,* J. Phys. Chem. C **116**, 24649 (2012).

[76] P. Stein, *Investigation of CuMnSb/aluminum oxide tunnelling devices*, Master's thesis, Universität Würzburg (2020).

[77] L. Scheffler, K. Gas, S. Banik, M. Kamp, J. Knobel, H. Lin, C. Schumacher, C. Gould, M. Sawicki, J. Kleinlein, and L. W. Molenkamp, *Molecular beam epitaxy of the half-Heusler antiferromagnet CuMnSb,* Phys. Rev. Mater. **4**, 114402 (2020).

[78] C. Ciccarelli, L. Anderson, V. Tshitoyan, A. J. Ferguson, F. Gerhard, C. Gould, L. W. Molenkamp, J. Gayles, J. Železný, L. Šmejkal, Z. Yuan, J. Sinova, F. Freimuth, and T. Jungwirth, *Room-temperature spin−orbit torque in NiMnSb,* Nat. Phys. **12**, 855 (2016).

[79] E. J. Kirkland, *Advanced Computing in Electron Microscopy* (Springer US, 2010).

[80] N. Volkenshtein and V. Novoselov, *Anisotropy of the resistivity and hall coefficient of ru in the low-temperature range,* Phys. Met. Metallogr. **33**, 105 (1972).

[81] R. W. Powell, R. P. Tye, and M. J. Woodman, *The thermal conductivity and electrical resistivity of polycrystalline metals of the platinum group and of single crystals of ruthenium,* J. Less Common Metals **12**, 1 (1967).

[82] J. T. Schriempf and W. M. Macinnes, *Electrical and thermal resistivities of ruthenium from 2 to 20 K,* Phys. Lett. A **33**, 509 (1970).

[83] K. Fuchs, *The conductivity of thin metallic films according to the electron theory of metals,* Math. Proc. Cambridge Philos. Soc. **34**, 100 (1938).

[84] A. F. Mayadas and M. Shatzkes, *Electrical-resistivity model for polycrystalline films: the case of arbitrary reflection at external surfaces,* Phys. Rev. B **1**, 1382 (1970).

[85] S. Dutta, K. Sankaran, K. Moors, G. Pourtois, S. V. Elshocht, J. Bömmels, W. Vandervorst, Z. Tőkei, and C. Adelmann, *Thickness dependence of the resistivity of platinum-group metal thin films,* J. Appl. Phys. **122**, 025107 (2017).

[86] N. Mott, *Electrons in transition metals,* Adv. Phys. **13**, 325 (1964).

[87] A. Bauer, *Investigation ofitinerant antiferromagnetsand cubic chiral helimagnets,* Ph.D. thesis, Technische Universität München (2014).

[88] T. Jeong, R. Weht, and W. E. Pickett, *Semimetallic antiferromagnetism in the half-heusler compound CuMnSb,* Phys. Rev. B **71**, 184103 (2005).

[89] A. Regnat, *Low-temperature propertiesand magnetic structure of CrB_2, MnB_2, and CuMnSb,* Ph.D. thesis, Technische Universität München (2018).

[90] M. J. Otto, H. Feil, R. A. M. V. Woerden, J. Wijngaard, P. J. V. D. Valk, C. F. V. Bruggen, and C. Haas, *Electronic structure and magnetic, electrical and optical properties of ferromagnetic Heusler alloys,* J. Magn. Magn. Mater. **70**, 33 (1987).

[91] M. J. Otto, R. A. M. van Woerden, P. J. van der Valk, J. Wijngaard, C. F. van Bruggen, and C. Haas, *Half-metallic ferromagnets. II. Transport properties of NiMnSb and related inter-metallic compounds,* J. Phys.: Condens. Matter **1**, 2351 (1989).

[92] H. Lueken, *Magnetochemie* (Vieweg+Teubner Verlag, 2013).

[93] M. Doerr, J. Bœuf, C. Pfleiderer, M. Rotter, N. Kozlova, D. Eckert, P. Kerschl, K.-H. Müller, and M. Loewenhaupt, *Search for half-metallic antiferromagnetism using pulsed magnetic fields: experimental investigation of Mn_3Si, CuMnSb and PdMnTe,* Phys. B Condens. Matter **346-347**, 137 (2004).

[94] S. Hasegawa, *Reflection High-Energy Electron Diffraction,* in *Characterization of Materials* (John Wiley & Sons, Ltd, 2012) pp. 1–14.

[95] L. Scheffler, J. Werther, K. Gas, C. Schumacher, C. Gould, M. Sawicki, J. Klein-lein, and L. W. Molenkamp, *Bulk-like magnetic properties in MBE-grown unstrained, antiferromagnetic CuMnSb,* Appl. Phys. Lett. **121**, 012401 (2022).

[96] C. E. C. Wood, D. Desimone, K. Singer, and G. W. Wicks, *Magnesium- and calcium-doping behavior in molecular-beam epitaxial III-V compounds,* J. Appl. Phys. **53**, 4230 (1982).

[97] W. V. Roy, J. D. Boeck, B. Brijs, and G. Borghs, *Epitaxial NiMnSb films on GaAs(001),* Appl. Phys. Lett. **77**, 4190 (2000).

[98] F. Gerhard, C. Schumacher, C. Gould, and L. W. Molenkamp, *Control of the magnetic in-plane anisotropy in off-stoichiometric NiMnSb,* J. Appl. Phys. **115**, 094505 (2014).

[99] P. Dürrenfeld, F. Gerhard, J. Chico, R. K. Dumas, M. Ranjbar, A. Bergman, L. Bergqvist, A. Delin, C. Gould, L. W. Molenkamp, and J. Åkerman, *Tunable damping, saturation magnetization, and exchange stiffness of half-Heusler NiMnSb thin films,* Phys. Rev. B **92**, 214424 (2015).

[100] M. P. Raphael, B. Ravel, Q. Huang, M. A. Willard, S. F. Cheng, B. N. Das, R. M. Stroud, K. M. Bussmann, J. H. Claassen, and V. G. Harris, *Presence of antisite disorder and its characterization in the predicted half-metal Co_2MnSi,* Phys. Rev. B **66**, 104429 (2002).

[101] Z. Hou, W. Wang, G. Xu, X. Zhang, Z. Wei, S. Shen, E. Liu, Y. Yao, Y. Chai, Y. Sun, X. Xi, W. Wang, Z. Liu, G. Wu, and X. xiang Zhang, *High electron mobility and large magnetoresistance in the half-Heusler semimetal LuPtBi,* Phys. Rev. B **92**, 235134 (2015).

[102] I. Dzyaloshinsky, *A thermodynamic theory of "weak" ferromagnetism of anti-ferromagnetics,* J. Phys. Chem. Solids **4**, 241 (1958).

[103] T. Moriya, *Anisotropic Superexchange Interaction and Weak Ferromagnetism,* Phys. Rev. **120**, 91 (1960).

[104] H. T. Hirose, J. ichi Yamaura, and Z. Hiroi, *Robust ferromagnetism carried by antiferromagnetic domain walls,* Sci. Rep. **7** (2017).

[105] M. Jagodič, Z. Jagličić, A. Jelen, J. B. Lee, Y.-M. Kim, H. J. Kim, and J. Dolinšek, *Surface-spin magnetism of antiferromagnetic NiO in nanoparticle and bulk morphology,* J. Phys.: Condens. Matter **21**, 215302 (2009).

[106] Y. Z. Hu, M. Li, J. W. Andrews, K. A. Conrad, and E. A. Irene, *A Comparison of Argon and Hydrogen Ion Etching and Damage in the Si‑SiO$_2$ System*, J. Electrochem. Soc. **139**, 2022 (1992).

[107] R. Rodriguez, A. Fernandez, A. Isalgue, J. Rodriguez, A. Labrata, J. Tejada, and X. Obradors, *Spin glass behaviour in an antiferromagnetic non-frustrated lattice: Sr$_2$FeNbO$_6$ perovskite*, J. Phys. C: Solid State Phys. **18**, L401 (1985).

[108] J. Kroder, K. Manna, D. Kriegner, A. S. Sukhanov, E. Liu, H. Borrmann, A. Hoser, J. Gooth, W. Schnelle, D. S. Inosov, G. H. Fecher, and C. Felser, *Spin glass behavior in the disordered half-Heusler compound IrMnGa*, Phys. Rev. B. **99**, 174410 (2019).

[109] J. R. L. de Almeida and D. J. Thouless, *Stability of the Sherrington-Kirkpatrick solution of a spin glass model*, J. Phys. A: Math. Gen. **11**, 983 (1978).

[110] M. Ozima and M. Ozima, *Origin of thermoremanent magnetization*, J. Geophys. Res. **70**, 1363 (1965).

[111] H. Mamiya, S. Nimori, M. Ohnuma, I. Nakatani, M. Demura, and T. Furubayashi, *Comparison of field-cooled, zero-field-cooled, and thermoremanent magnetization in nanomagnet, random magnet, and bulk ferromagnet*, J. Magn. Magn. Mater. **316**, e535 (2007).

[112] J. Nogués and I. K. Schuller, *Exchange bias*, J. Magn. Magn. Mater. **192**, 203 (1999).

[113] A. L. Yaouanc, *Muon spin rotation, relaxation, and resonance applications to condensed matter* (Oxford University Press, 2010).

[114] T. Prokscha, E. Morenzoni, K. Deiters, F. Foroughi, D. George, R. Kobler, A. Suter, and V. Vrankovic, *The new beam at PSI: A hybrid-type large acceptance channel for the generation of a high intensity surface-muon beam*, Nucl. Instrum. Methods Phys. Res. A: Accel. Spectrom. Detect. Assoc. Equip. **595**, 317 (2008).

[115] A. Hirohata, H. Sukegawa, H. Yanagihara, I. Zutic, T. Seki, S. Mizukami, and R. Swaminathan, *Roadmap for Emerging Materials for Spintronic Device Applications*, IEEE Trans. Magn. **51**, 1 (2015).

[116] Feldman, *Fundamentals of Surface and Thin Film Analysis* (Appleton & Lange, 1992).

[117] K. Takanashi, M. Watanabe, H. Fujimori, and H. Yasuoka, *NMR investigation of the anomalous magnetization behavior in PtMnSb/CuMnSb multilayer films,* J. Magn. Magn. Mater. **104-107**, 1751 (1992).

[118] A. Koveshnikov, G. Woltersdorf, J. Q. Liu, B. Kardasz, O. Mosendz, B. Heinrich, K. L. Kavanagh, P. Bach, A. S. Bader, C. Schumacher, C. Rüster, C. Gould, G. Schmidt, L. W. Molenkamp, and C. Kumpf, *Structural and magnetic properties of NiMnSb/InGaAs/InP(001),* J. Appl. Phys. **97**, 073906 (2005).

[119] S. K. Ren, W. Q. Zou, J. Gao, X. L. Jiang, F. M. Zhang, and Y. W. Du, *Magnetic behavior of half-Heusler alloy $Cu_xNi_{1-x}MnSb$,* J. Magn. Magn. Mater. **288**, 276 (2005).